UNIVERSITÀ DEGLI STUDI DI PADOVA

Dipartimento di Fisica e Astronomia “Galileo Galilei”

Master Degree in Astrophysics and Cosmology

Final Dissertation

CHARACTERIZATION OF THE PHYSICAL AND DYNAMICAL PROPERTIES OF THE TOI-201 EXOPLANETARY SYSTEM

Thesis supervisor

Prof. Francesco Marzari

Thesis co-supervisors

Dr. Dino Mesa

Dr. Domenico Barbato

Candidate

Andrea Bernardi

Academic Year 2024/2025

To those who always supported me, and whom fate decided would no longer be here. You will not be forgotten.

Contents

Chapter 1

Introduction

The existence of other worlds is not a modern idea, but one that dates back thousands of years and was proposed by several philosophers. Among them, the Greek philosopher Epicurus, in his *Letter to Herodotus*, wrote: "[...] there are infinitely many worlds, both similar to this one and different from it. [...] there is nothing to prevent the infinity of worlds". More than two centuries after Epicurus, the Roman philosopher Lucretius, deeply influenced by Epicurean thought, wrote in his *De Rerum Natura*: "[...] if the number of atoms is so immense that the whole span of living time would not suffice to count them, and if the same power and nature persist that can combine atoms in the same way wherever they may be, then it must be admitted that there exist elsewhere in the void other earth-like worlds [...]".
Now, more than 2000 years later, thousands of planets have been discovered, exhibiting a diversity in their properties that would undoubtedly have pleased the ancient philosophers mentioned above. As of May 27, 2025, a total of 5 912 planets have been discovered, according to the NASA Exoplanet Archive[1]. Figure 1.1 illustrates the distribution of these planets, highlighting their mass and orbital period. The positions of the Solar System planets are also overlaid for comparison.

[1] https://exoplanetarchive.ipac.caltech.edu/index.html

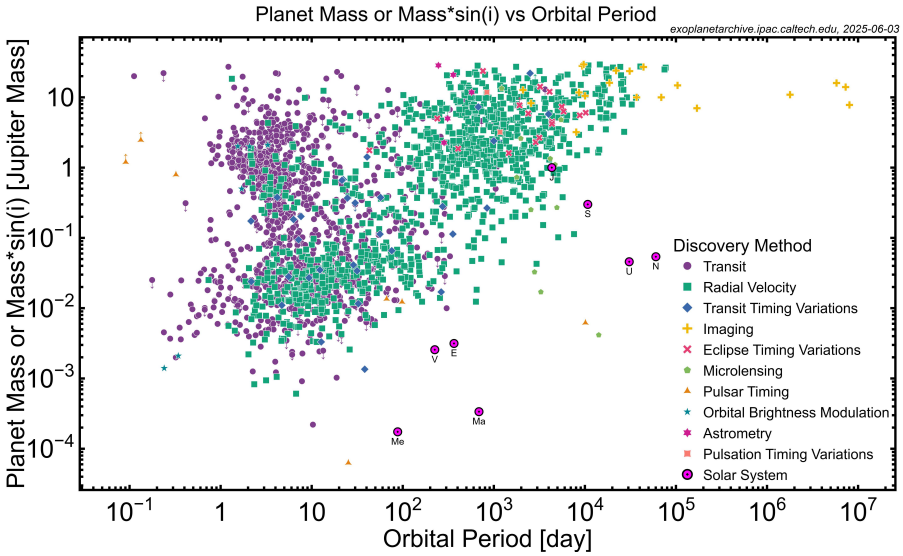

Figure 1.1: Distribution of the exoplanets discovered as of May 27, 2025, in the orbital period–mass plane. Detection methods are indicated by color and shape, and Solar System planets are included for comparison. Credits: NASA Exoplanet Archive.

This Master's thesis focuses on the characterization of the physical and dynamical properties of the exoplanetary system TOI-201. Astrometric measurements suggest the presence of an additional, yet undetected companion orbiting the host star. The goal of this work is to analyze the available observational data to constrain the properties of this companion and to assess the feasibility of its detection with current and future instrumentation. The dynamical stability of the system is also investigated through numerical simulations and the estimation of chaos indicators, and possible evolutionary scenarios leading to its present-day configuration are explored.

The work is organized as follows. Chapter 2 provides an overview of planet formation models, along with a description of the main classes of exoplanets and their properties. Chapter 3 discusses the principal detection techniques, including a historical perspective and the fundamental concepts behind each method. Chapter 4 is entirely dedicated to the main detection method used in this work: direct imaging. A comprehensive description of the so-called 'three pillars' of high-contrast imaging (adaptive optics, coronagraphy, and differential imaging) is provided, along with a general discussion of the principles behind direct imaging and an overview of some current and upcoming dedicated instruments. A more detailed description is given of SPHERE, the instrument from which the TOI-201 imaging data analyzed in this work were obtained. Chapter 5 is entirely dedicated to the analysis of observational data for TOI-201. Following a brief introduction to the target and a review of the relative

literature, the astrometric measurements are presented, highlighting their implications and the reasons why TOI-201 is a particularly interesting system to investigate. The subsequent section provides a detailed description of the data reduction and post-processing of high-contrast imaging data from SPHERE, outlining the various steps and methodologies involved. The final part of the chapter focuses on a multi-technique analysis combining astrometric and radial velocity data, which enables the determination of a set of orbital parameters for the companion, ultimately classifying it as a low-mass brown dwarf. Finally, Chapter 6 presents the stability and dynamical analysis of the TOI-201 system. A long-term numerical integration confirms that the system is indeed stable. This result is further supported by a stability analysis based on the MEGNO chaos indicator, which identifies regions of stability and instability and confirms the long-term stability of the system. The final section discusses possible evolutionary scenarios for TOI-201. Its peculiar configuration suggests that, shortly after disk dissipation, the system experienced a phase of dynamical instability involving planet–planet scattering, likely resulting in the ejection of one or more planets. An alternative explanation considers the role of secular perturbations, which could have driven the system toward its current configuration.

Chapter 2

Extrasolar planets and statistics

Innumerable suns exist; innumerable earths revolve around these suns in a manner similar to the way the seven planets revolve around our sun.
– G. Bruno

Thousands of exoplanets have been discovered, exhibiting a wide range of properties, including mass, orbital distance, composition, and more. This chapter provides a general overview of the principal planetary formation models, beginning with protoplanetary disks and outlining the main evolutionary stages, including a brief discussion of planetary migration. In the second part, several classification schemes for exoplanets are presented, along with details on the different categories and a concise review of theoretical models that aim to explain and reproduce the currently observed exoplanet population.

2.1 Planet formation model

Planetary systems are believed to form as common byproducts of star formation. Stars form in molecular clouds, structures with wide density and composition variations, mainly composed by molecular gas (dominated by H_2 and He with presence of compounds such as CO, CO_2 and CH_4) and dust grains (mainly olivine and pyroxene). While the formation mechanisms of stars with masses above 8 $M_\odot$ remain uncertain, stars with lower masses are generally thought to form through gravitational instabilities within molecular clouds, which trigger gravitational collapse and subsequently lead to the formation of a gas and dust-rich circumstellar disk. Brown dwarfs, objects within the mass range of 13-80 M_J, are formed as the low-mass tail of this process, although some may be formed as a high mass tail of planet formation.
As the star forms, the surrounding disk can provide the conditions necessary for the formation of planetary companions. According to the most recent stud-

ies, two main models have been proposed to explain planet formation: the core accretion model (Safronov [1972]) and the gravitational instability model (Boss [1997]). The former (which will be described in detail starting from Section 2.1.2) is a bottom-up process, in which bodies grow progressively through the accretion of smaller solids. It proceeds through a number of stages that, together, extend over more than 14 orders of magnitude in size, from sub-micron dust grains to the giant planets, and it is generally viewed as taking place in three distinct stages. In the first stage, within protoplanetary disks, dust grains of heavy elements that condensed from the cooling gas collide and stick by short-range van der Waals attraction, resulting in cm-sized or larger particles. In the second stage of growth, from cm to km-sized bodies, planetesimals form. However, accretional growth in this phase is particularly challenging in a turbulent disk, as turbulence can lead to the fragmentation of previously formed bodies, and the physical processes involved in this stage remain highly uncertain. In the third coagulation stage, dominated by gravity, planetesimals merge by physical and gravitational capture as they collide. Continued accretion yields protoplanets on time scales of 10^5 - 10^6 years, which continue to collide and merge into full-sized planets. The core-accretion model successfully explains the formation of both terrestrial and most of the giant planets through the gradual accumulation of solids followed by gas accretion in the case of massive cores.
The gravitational instability model (described in more detail in Section 2.1.6), which accounts for the formation of the most massive giant planets, follows a top-down approach. In this scenario, gas giant protoplanets form through the rapid collapse of regions within a gravitationally unstable protoplanetary disk. Compared to core accretion, this is a much faster process and strongly depends on the ability of the disk's self-gravity to overcome internal thermal pressure.
The primordial phase of disk evolution in which giant planet formation takes place typically ends in 1-6 Myr with the dissipation of the gas. Over the next few Myr, the remnant primordial circumstellar dust is either dispersed by stellar radiation, decelerated by Poynting-Robertson drag and accreted onto the star, or accreted onto growing planetesimals. Over the following $\sim$ 30 Myr, rocky terrestrial protoplanets continue to accrete planetesimals, while icy protoplanets grow by accreting icy planetesimals beyond the snow line. The snow line, characteristic for each chemical species, is defined as the radial distance from the host star where that compound transitions from gas to solid ice grains. By 100 Myr, current models portray planetary systems at a relatively mature stage, with little accretion growth occurring. Figure 2.1 schematizes the various processes involved in planetary formation, along with indicative timescales for each stage. Terrestrial planets and giant planets have different formation paths, but they both have origin from the same structure: a protoplanetary disk.

2.1.1 Protoplanetary disks

Star formation begins with the gravitational collapse of a molecular cloud, triggered by a highly supersonic turbulent flow. Local density enhancements due to the compression of finite volumes within the flow become gravitationally unsta-

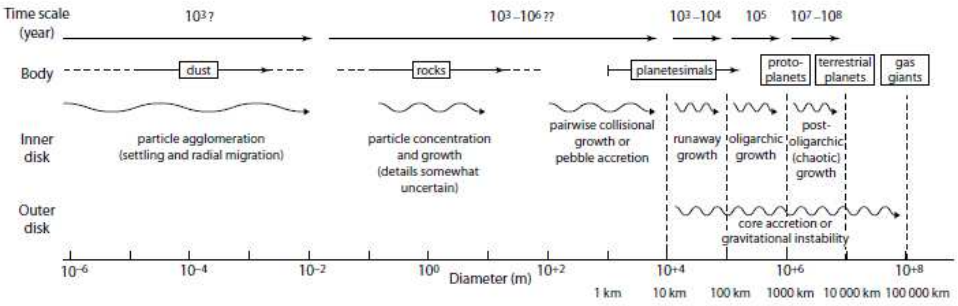

Figure 2.1: Schematic of the growth of planets, starting with sub-micron dust and extending up to the terrrestrial planets in the inner disk, and the gas giants in the outer disk. Some indicative time scales are given (Perryman [2018]).

ble if, according to the Jeans instability criterion, their size (hereafter denoted by λ) exceeds the critical Jeans length:

$$\lambda_J = \sqrt{\frac{\pi c_s^2}{G\rho}} \,, \tag{2.1.1}$$

where ρ is the local density, $c_s^2 = kT/\mu$ is the isothermal sound speed, μ is the mean molecular weight, T is the temperature and k the Boltzmann constant. If $\lambda > \lambda_J$ the thermal pressure cannot resist self-gravity and runaway collapse follows. The material within a gravitational unstable region of a molecular cloud carries some angular momentum, which prevents the collapsing material from falling directly onto the protostar. Instead it falls, by symmetry, onto a flat rotating disk in the plane passing through the center of mass and orthogonal to the total angular momentum of the cloud. The disk extends out to the centrifugal radius, which is expected to grow rapidly with time according to $R(t) \propto \Omega^2 t^3$, where Ω is the angular rotation rate of the core. Numerical models (Hueso and Guillot [2005]) show that disks form rapidly, within $\sim 10^4$ yr. Temperatures are very high in these early stages due to gravitational infall, and as the core material is used up or dispersed, the disk cools down and its mass decreases as it accretes onto the star. The fraction of the gas and dust falling onto the disk rather than onto the star depends on the angular momentum of the collapsing cloud, but may exceed 90 %. For high disk to protostar mass ratios the disk is gravitationally unstable, spiral waves develop, and rapid mass accretion onto the star continues until the mass ratio falls below the Toomre instability limit (Toomre [1964]), which states that a disk is gravitationally unstable if:

$$Q = \frac{c_s \Omega}{\pi G \Sigma} < 1 \,, \tag{2.1.2}$$

with $Q \approx 1$ implying marginal instability. Here, $c_s = (\gamma P/\rho)^{1/2}$ is the sound speed, $\Omega = (GM_\star/R^3)^{1/2}$ is the Keplerian angular frequency at radius R, and

Σ is the disk surface density.
Furthermore, if the disk is isothermal in the vertical direction z and in hydrostatic equilibrium, the vertical profile of the gas density is:

$$\rho_g(z) = \frac{\Sigma(R)}{\sqrt{2\pi}H_g}\, exp(-z^2/2H_g^2)\,, \tag{2.1.3}$$

where

$$H_g = \sqrt{\frac{kT}{\Omega^2 \mu m_H}}\,, \tag{2.1.4}$$

is called the gas scale height, with m_H the mass of the hydrogen atom. Protoplanetary disks are observed to dissipate, as mentioned before, in few Myr, with relatively high accretion rates onto the host star, of the order of $\sim 10^{-8}\ M_\odot/yr$. The initial mass of the disk is usually assumed to be a few percents of the stellar mass, and this coupled with the high accretion rates implies that most of the disk mass needs to be transported towards the star, and its angular momentum needs to be removed on the same timescale. The microscopic viscosity of the disk cannot account for this, so a turbulent viscosity $\nu = \alpha c_s H_g$ (Shakura and Sunyaev [1973]) is introduced, with α a dimensionless parameter called the Shakura-Sunyaev parameter and c_s the isothermal speed of sound. This shear-driven turbulence arises because gas closer to the center rotates more rapidly than in the outer regions; the shear then breaks down into a turbulent flow which produces the torque needed to transport angular momentum at larger radii. Over time, the disk is expected to grow in radius while decreasing in mass, resulting in a decreasing accretion rate.
The assumption of viscous shear transporting angular momentum and Keplerian orbital motion allows for deriving a single equation yielding the evolution of the gas surface density (Pringle [1981]):

$$\frac{d\Sigma}{dt} = \frac{3}{r}\frac{d}{dr}\left[\sqrt{r}\frac{d}{dr}\left(\sqrt{r}\nu\Sigma\right)\right]. \tag{2.1.5}$$

This differential equation, once solved, gives the evolution of the disk density radial distribution with time. Physical models of viscous accretion disks (e.g. Hartmann et al. [1998]) predict an exponential profile of the form:

$$\Sigma(R) = (2-\gamma)\frac{M_d}{2\pi R_c^2} exp\left[-\left(\frac{R}{R_c}\right)^{2-\gamma}\right]\,, \tag{2.1.6}$$

where M_d is the disk mass, R_c is a characteristic radius, and γ specifies the radial dependence of the disk viscosity, $\nu \propto R^\gamma$. This exponential form approximates a power law, $\Sigma \propto R^{-\gamma}$, for $R \ll R_c$. A typical reference disk is the so-called Minimum Mass Solar Nebula (MMSN, Hayashi [1981]), whose density profile is:

$$\Sigma(R) = 1700\left(\frac{R}{1\ AU}\right)^{-3/2} g/cm^2\,, \tag{2.1.7}$$

and whose temperature profile is:

$$T(R) = 280 \left(\frac{R}{1\ AU} \right)^{-1/2} K\ , \tag{2.1.8}$$

obtained by smearing the mass of the planets in a disk extending approximately for 40 AU and assuming a dust-to-gas ratio of 0.01. Recently, on the basis of the characteristics of extrasolar planetary systems, more massive disks are suggested (Minimum Mass Extrasolar Nebula, MMEN) with values of Σ_0 ranging from 5 to 20 times that of the MMSN. Figure 2.2 shows the evolution of various physical parameters of a protoplanetary disk in the α-viscosity regime.

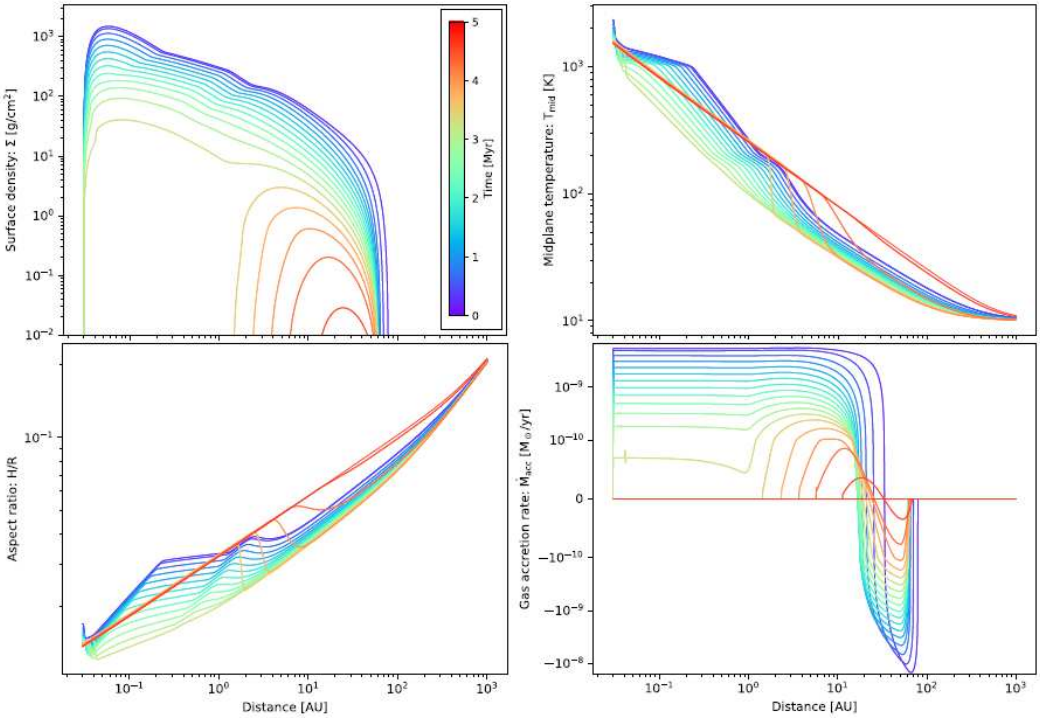

Figure 2.2: Evolution of a protoplanetary gas disk as a function of the distance from the star and time in the α-viscosity model. The panels show the gas surface density (*top left*), midplane temperature (*top right*), aspect ratio H/r (*bottom left*) and accretion rate (*bottom right*). From Mordasini and Burn [2024].

The evolution of the disk is primarily governed by processes such as viscosity, accretion onto the central star, grain coagulation, and photoevaporation, and can be broken down into several distinct phases, as described here. In the early stages of its evolution, the disk loses mass through accretion onto the star and FUV-driven photoevaporation of the outer disk. The FUV photoevaporation is

likely to truncate the outer edge of the disk, limiting its viscous expansion to a finite size of several hundreds of AU in diameter. At the same time, grains grow into larger bodies that settle onto the mid-plane of the disk where they can grow into rocks, planetesimals and beyond. Accordingly, the scale height of the disk decreases and the initially flared disk becomes flatter. As the disk mass and the accretion rate decrease, energetic photons from the stellar chromosphere are able to penetrate the inner disk and photoevaporation becomes important. When the accretion rate drops to the photoevaporation rate, the outer disk is no longer able to resupply the inner disk. At this point, the inner disk drains on a viscous timescale ($\lesssim 10^5$ yr) and an inner hole of a few AU in radius is formed in the disk. Once this inner hole has formed, the photoevaporation rate increases further, preventing any material from the outer disk from flowing into the inner hole. By the time this hole is formed, the mass of the outer disk is believed to be $\lesssim$ 1-2 M_J. Protoplanetary disks showing spectroscopic evidence for these inner holes are called transition disks.

Transition disks and, more in general, protoplanetary disks, have been detected with different methods, like for example direct imaging or with the infrared excess in the power spectrum of the star (e.g. Figure 2.3). In fact, if a protoplanetary disk is present around a star, its dust emits at a lower temperature with respect to the star and its blackbody radiation falls within the infrared spectrum range. As a consequence, the observed spectrum of the star is given by the combination of that of a blackbody with the superficial temperature of the star and that of a colder source (the disk), the infrared excess. From the morphology of the infrared excess is possible to deduce if the disk has gaps or holes. Transition disks are often associated with the presence of planetary or substellar companions, which are thought to be responsible for the observed gaps. Initially, they were considered as an intermediate phase in the evolution from optically thick disks extending to the stellar surface to systems where the disk has fully dissipated, potentially due to planet formation processes. One of the leading explanations for the spectral energy distribution (SED) of transition disks is that these systems are actively forming planets, as planet formation models predict the clearing of disk regions (see Espaillat et al. [2014] for a comprehensive review). A notable example is PDS 70 (Keppler et al. [2018]), a pre-main sequence star with an estimated age of 5.4 ± 1.0 Myr. Infrared excess in its SED provides evidence of a surrounding disk, and detailed modeling suggests that while the inner region is largely cleared of dust, a small optically thick inner disk still emits in the near-infrared. Observations with VLT/SPHERE, VLT/NaCo, and Gemini/NICI revealed the presence of a young protoplanet within the disk gap, marking the first direct imaging of a protoplanet. Subsequent studies (Haffert et al. [2019]) using H_α emission analysis identified a second protoplanet orbiting the star, further confirming that the system is undergoing active planet formation. Once the remaining gas photoevaporates, the dynamics of solid particles is dominated by radiation effects. The small grains ($r \lesssim 1\,\mu m$) are swept out by radiation pressure, and slightly larger ones spiral in due to Poynting-Robertson drag and sublimate when they reach the dust sublimation radius. What is left is a debris disk: a gas poor disk with large

grains, planetesimals and/or planets.

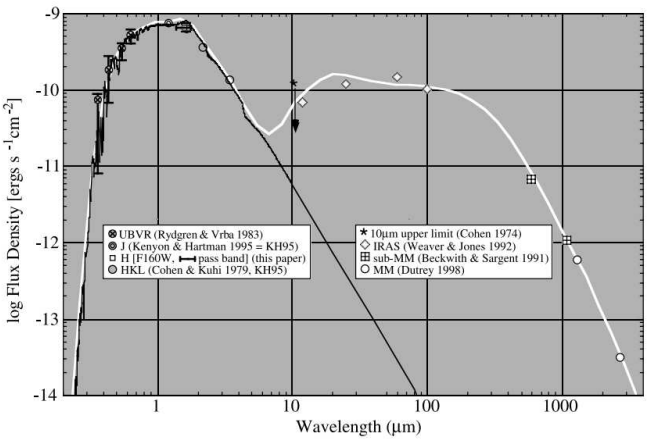

Figure 2.3: Spectral energy distribution of the star GM Aurigae. It shows a mid to far infrared excess, indicating the presence of a circumstellar disk (Schneider et al. [2003]).

2.1.2 From dust to pebbles and planetesimals

As particles start to aggregate and grow within the disk, inward drift occurs rapidly. Dust and particles in a protoplanetary disk are affected by aerodynamic drag due to their relative velocity with respect to the gas, whose rotation rate is sub-Keplerian because of the pressure gradient. Starting from the density and temperature profiles, the rotation frequency of the gas can be computed, leading to:

$$\omega_g^2 = \omega_K^2[1 - 2\eta(r)] \,, \tag{2.1.9}$$

with $\omega_K = (GM/r^3)^{1/2}$ the Keplerian rotation frequency and $\eta(r) = nc_m^2/v_K^2$, where c_m is the mean thermal speed of the gas, v_K the Keplerian velocity and n is a constant factor. Typical values of η range from 10^{-5} to 10^{-3}. This drag force can be expressed with two different formulations, depending on the ratio between the size s of the body and the mean free path λ of the gas molecules. If $s \ll \lambda$ the gas particles are treated as projectiles colliding with the dust grain. The drag force in this regime is called the Epstein drag and takes the form:

$$\mathbf{F}_D = -\frac{4}{3}\pi s^2 \rho_g v_{th} \mathbf{v} \,, \tag{2.1.10}$$

where $v_{th} = \sqrt{\frac{8kT}{\pi m}}$ is the thermal velocity, ρ_g the gas density and v the relative velocity of the dust particle with respect to the gas. This force, that acts in the direction opposite to the dust particle velocity, has two dynamical effects: it causes an inward drift of the dust and it also forces a sedimentation of the

dust towards the central plane of the disk. In particular, the time required by a dust particle of size s to settle towards the median plane of the disk is:

$$t_{settle} = \frac{v_{th}\rho_g}{\Omega_K^2 \rho_d s} \ , \tag{2.1.11}$$

with ρ_d the dust density, and it is of the order of 10^5 years for a typical disk at 1 AU from the star. The drag on the particles is both in the radial and azimuthal direction, described by:

$$v_r = -\frac{2\Delta v}{St + St^{-1}} \tag{2.1.12}$$

$$v_\phi = v_K - \frac{\Delta v}{1 + St^2} \ , \tag{2.1.13}$$

where Δv is the difference between the gas actual velocity with respect to the Keplerian velocity and $St = \Omega_K \tau_f$ is the dimensionless Stokes number, with τ_f the friction time.
If, instead, $s \gg \lambda$, the interaction between the gas and the body is described by the laws of fluid dynamics and the body is in the so-called Stokes regime. In this regime, the drag force is well described by:

$$\mathbf{F}_D = -\frac{C_D}{2}\pi s^2 \rho_g v \mathbf{v} \ , \tag{2.1.14}$$

where the aerodynamical coefficient C_D depends on the local value of the Reynolds number $Re = 2sv/\nu_m$, with ν_m the viscosity coefficient of the motion of the body within the fluid. If continuously replenished by growth, the maximum particle size reached before radial drift removes them is approximated by:

$$s_{drift} \sim \frac{2}{\pi}\frac{\Sigma_{dust}}{\rho_s}\frac{v_K^2}{c_s^2}\gamma^{-1} \ , \tag{2.1.15}$$

where Σ_{dust} is the dust surface density, ρ_s is the density of the dust aggregate and γ is the absolute value of the power law index of the gas pressure profile. Figure 2.4 illustrates the dust evolution in a standard protoplanetary disk, highlighting the different growth and drift regimes.
In a protoplanetary disk, the Stokes force is used to describe the perturbations by the gas on the planetesimals, and it is possible to calculate its effect on the orbital elements. The results show that the Stokes force yields a decay in semi-major axis, eccentricity and inclination. These last two effects are important in the early stages of planet formation because they enhance the collisional growth of planetesimals by keeping low their relative impact velocity, well described by:

$$v_{rel} \sim (\frac{5}{4}e^2 + i^2)^{1/2} v_K. \tag{2.1.16}$$

In addition to the hydrodynamical forces of pressure and gravity, a magnetized fluid is subject to Lorentz forces and, if the fluid is differentially rotating, this force can be highly disruptive, even if the magnetic field is weak. The

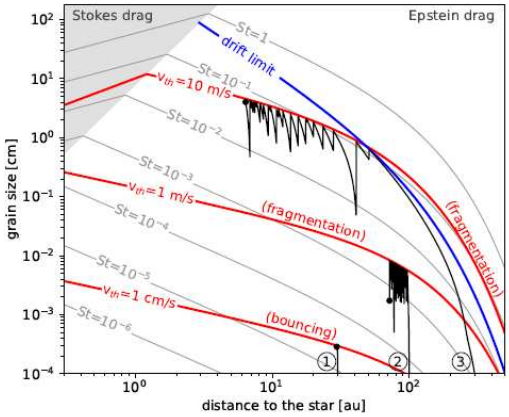

Figure 2.4: Dust evolution in a standard protoplanetary disk model. Grey lines indicate the size of dust aggregates with an internal density of 1 g/cm^3. The shaded area marks the Stokes drag regime, while the blue line represents the drift limit, beyond which the coagulation timescale exceeds the radial drift timescale. Black lines trace the evolutionary paths of three test particles, and red lines indicate the maximum grain size reached through dust coagulation for the adopted threshold velocity values (Drazkowska et al. [2023]).

resulting magnetorotational instability leads to self-sustaining turbulence, an outward transfer of angular momentum, an inward mass flow and to conditions favourable for particle accretion. In particular, simulations show that large-scale, long-lived pressure bumps form spontaneously in the turbulent flow, thus leading to concentrations of particles into radial bands and favouring the accretion of dust particles.

The solids available for planet formation are not uniform across a protoplanetary disk: at any given radius, only species with condensation or sublimation temperatures below the local temperature can exist as solids. As the disk cools over time, the locations of different snow lines move inwards. Iron and silicates are generally abundant in the inner regions of the disk, while the outer regions are rich in ice and other volatiles. If the presence of dust is allowed by the local temperature, dust grains are presumed to settle into a dense layer towards the disk mid-plane, where they begin to stick together through a combination of electrostatic forces and other factors like dipole charging, aerodynamical re-accretion, magnetic sticking and compositional features like porosity and ice fraction, growing as they collide. The smallest particles collide slowly due to Brownian motion, while larger aggregates achieve progressively higher collision speeds as they decouple from the gas flow. An equilibrium mid-plane layer is formed when the turbulent diffusion of the particles balances the rate of sedimentation, in a settling time scale of $\sim 10^5$-10^6 years.

The outcome of a collision between dust particles of different sizes can be con-

structive or erosive: direct collisional sticking happens when two dust aggregates collide slowly enough for contact forces to bind the aggregates together, while dust particles with intermediate sizes bounce and the presence of high collisional energy results in the break up of dust aggregates. Specifically, the formation of larger objects may be halted by a combination of fragmentation in disruptive collisions and mutual rebound. An important factor, determinant for the outcome of a collision, is the relative speed between the dust particles, given by the sum of the following contributions:

- Brownian velocity, which gives a contribution of the order of the thermal velocity:

$$v \sim v_{th} = \sqrt{\frac{8k_B T}{\pi \mu m_H}}\,, \tag{2.1.17}$$

  with T the local temperature of the disk and μ the mean molecular weight;

- differential vertical settling velocity:

$$v_{settle} = \frac{\rho_d}{\rho_g}\frac{s}{v_{th}}\Omega^2 z\,, \tag{2.1.18}$$

  due to the different settling velocities of dust grains of different sizes. Here, ρ_d and ρ_g are the dust and gas densities, respectively, s the radius of the grains and Ω the Keplerian frequency;

- differential radial drift velocity towards the star:

$$v_{radial} = -\eta\frac{\rho_d}{\rho_g}\frac{s}{v_{th}}\Omega^2 R\,, \tag{2.1.19}$$

  where η is the same coefficient appearing in (2.1.9) and R the radial distance from the star.

In addition to these three components, gas turbulence can also give a signficant contribution to the impact speed. If this speed is too high, the chemical sticking forces are not strong enough to assemble a bigger body and fragmentation and cratering with mass loss will dominate.
The further growth of mm- and cm-sized particles faces several obstacles, one of them being the so-called bouncing barrier. Bouncing events have been observed frequently in experiments and, since bouncing does not lead directly to further mass gain, the growth of dust aggregates is inhibited at the resulting bouncing barrier. For a MMSN model at 1 AU, the maximum dust aggregate size is in the range of mm to cm. Above this barrier, growth has been found to continue by mass transfer in high speed collisions. However, on its own, this mass transfer does not to appear to lead to widespread planetesimal formation, other than perhaps in the innermost part of the protoplanetary disk where dynamical timescales are short. Another obstacle is the meter-size barrier. When the growing bodies become roughly meter-sized, many problems arise, mainly:

- objects of this size drift extremely quickly towards the central star where they are destroyed by the high temperatures. The drift timescale at this size becomes in particular shorter than the timescale for further growth, so that growth effectively stops. The time until destruction for roughly meter-sized bodies starting at 1 AU is $\lesssim 100$ years (see Figure 2.5).
- Meter-sized bodies do not stick well together, but rather shatter at the typical collision speeds which arise from the turbulent motion of the disk gas, and differential radial drift motion.

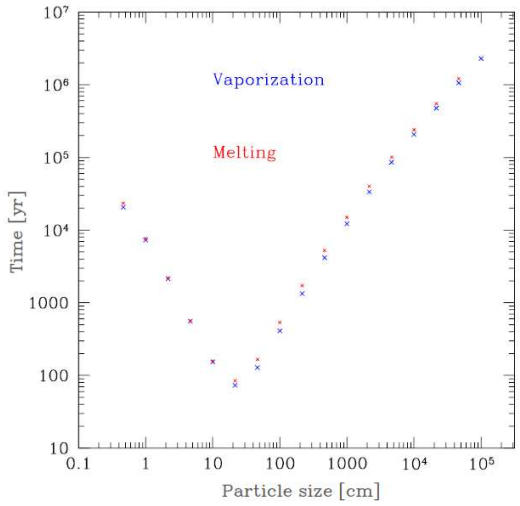

Figure 2.5: Time to destruction by inward spiraling into the host star for bodies of various initial sizes, assuming an initial orbital distance of 1 AU (Mordasini et al. [2010]).

As an alternative to the continuous growth of dust into planetesimals, gravitational instability has been proposed as a possible mechanism to convert directly dust into planetesimals. If self-gravity is strong enough, then planetesimals may form by gravitational collapse. In order for this to happen, the particles must be concentrated enough, so that the local density should be high enough to satisfy the following condition:

$$\rho_c > \frac{9\Omega_K^2}{4\pi G} , \tag{2.1.20}$$

where Ω_K is the Keplerian angular velocity at the location of the collapsing clump and ρ_c is the mean bulk density of the clump. This expression measures the interplay between stabilizing rotation, de-stabilizing self-gravity and stabilizing pressure of the clump. However, the onset of a Kelvin-Helmholtz instability due to the back-reaction of dust on the gas creates turbulence that diffuses the dust grains along the vertical direction, reducing the density. Drifting particles may also be captured at located higher pressure regions in the disk

called pressure bumps: particles drifting inwards are so slowed down, halted or even reversed depending on the steepness of the local pressure gradient. At these regions, the local density can increase by orders of magnitude with respect to the surrounding regions, allowing planetesimal formation by gravitational collapse.
Another mechanism involves the back-reaction friction force exerted by the particles on the sub-Keplerian gas, which results in its acceleration. If dust particles cluster sufficiently, their collective back-reaction becomes more prominent, reducing the speed at which the cluster drifts inwards. This allows other particles drifting from other regions of the disk to join the slowly drifting cluster, thus increasing the local density of solids and further reducing the cluster's drift rate. If the local dust to gas ratio exceeds a threshold for starting the collapse, the cluster shrinks sufficiently and the collapse may be successful in forming planetesimals in the range of sizes from ~ 1 to 1000 km. This mechanism is called streaming instability.
A quantitative approach to describe the size evolution of a number of merging bodies is based on the coagulation equation, which describes the evolution of the mass distribution of a collection of particles due to successive mergers. In discrete form, the bodies are represented as integer multiples of a small mass m_1, with n_k bodies of mass $m_K = km_1$ at time t. Neglecting fragmentation:

$$\frac{dn_k}{dt} = \frac{1}{2}\sum_{i+j=k} A_{ij} n_i n_j - n_k \sum_{i=1}^{\infty} A_{ki} n_i \ , \tag{2.1.21}$$

(Smoluchowski [1916]) where A_{ij} is the rate of mergers between bodies of mass m_i and m_j. The first term represents the increase in the number of bodies of mass m_k due to collisions of all pairs of bodies whose masses m_i, m_j sum to m_k, while the second describes the losses of masses m_k due to their incorporation into larger bodies. The outcomes depend very strongly on the assumed underlying physics of the internal structure, composition and fragmentation.
Over the next 10^4-10^5 years, further growth leads to the formation of planetesimals, objects of size ~ 1 km and above. This occurs through a continuation of the same type of collisional growth at smaller size scales, since gravitational interactions between individual bodies remain very weak until the minimum planetesimal mass is achieved. Once formed, planetesimals are decoupled from the gas: in this regime, if the random relative velocity between planetesimals (2.1.16) is lower than the escape speed from the largest of them, that body will grow accreting all other bodies that collide with it. Planetesimals must grow to run-away sizes despite bouncing or disruptive collisions and they must grow rapidly, constrained by radial drift time-scales that, for cm- to meter-sized particles, are as short as a few hundreds orbits. Newly-formed planetesimals move on elliptic orbits, and with gravitational interactions between them they increase their random motions, which can be damped by inelastic collisions. The dynamical friction also plays an important role during accretion. Because of angular momentum transfer, during closer encounters with smaller bodies, the largest planetesimals tend to have their orbital eccentricities and inclinations

damped. As result, their relative velocities decrease, favouring strong gravitational focusing. The protoplanet then grows at a rate given by (Pollack et al. [1996]):

$$\frac{dM_e}{dt} = \pi R_c \Sigma_p \Omega F_g \ , \tag{2.1.22}$$

where M_e is the embryo mass, R_c its capture radius, Σ_p the surface mass density of planetesimals, Ω the orbital frequency and F_g the gravitational focusing factor. The latter reflects the fact that due to gravity the effective collisional cross section of the body is larger than the geometrical one, as the trajectories get bended towards the body. For plausible models of disk mass of the order of $0.1\,M_\odot$ and a surface density varying as r^{-1}, total formation times estimated would be of order $4 \cdot 10^6$ yr for the Earth and $3 \cdot 10^{10}$ yr for Neptune. Thus local enhancements of the surface density, or a reduction in the relative planetesimal velocities are required to reduce the formation time scales.
Growth over the meter-size barrier remains particularly uncertain because of the various effects involved. Growth to 0.01 m may require $\sim 10^3$ yr, with growth from 0.01-10^4 m requiring a time in the range 10^3-10^6 yr. A mechanism that can help overcome the meter-size barrier is the so-called pebble accretion, based on the formation of cm-sized dust pebbles by coagulation. In later growth stages, it is much more favourable for an existing planetesimal to capture smaller pebbles within its Hill sphere, defined by the Hill radius:

$$R_H = a(1-e)\left(\frac{m}{3M_\star}\right)^{1/3} \ , \tag{2.1.23}$$

with m the mass of the protoplanet, $M_\star$ the mass of the star and a the semi-major axis of the protoplanet's orbit, than to interact with other protoplanets. Taking into account pebble accretion, numerical simulations showed that the core growth time is shortened by a factor 30-1000 at 50 AU. Two mechanisms halt pebble accretion: the fast dissipation of the disk that drags the pebbles towards a protoplanet and enhances the latter's impact cross-section; when the protoplanet reaches the so-called pebble isolation mass, it generates a pressure bump in the disk stopping the inward flux of pebbles. In this picture, cm-sized pebbles may be the primary building blocks of planetesimals, both inside the snow line and outside it. An estimate of the pebble isolation mass (here denoted as M_{PIM}) was provided by Ataiee et al. [2018], expressed as:

$$M_{PIM} \approx M_\star h^3 \sqrt{37.3\alpha + 0.01} \cdot \left[1 + 0.2\left(\frac{\sqrt{\alpha}}{h}\sqrt{\frac{1}{St^2} + 4}\right)^{0.7}\right] \ , \tag{2.1.24}$$

where $M_\star$ is the stellar mass, h is the aspect ratio of the disk, α is the α-turbulent viscosity parameter and St is the Stokes number. For typical values of α and h, such as $6 \cdot 10^{-3}$ and 0.05, respectively, the resulting pebble isolation mass is approximately $30\,M_\oplus$. Figure 2.6 shows the efficiency of pebble accretion, defined as the fraction of the total incoming pebble flux that is accreted by the protoplanet, across different regimes.

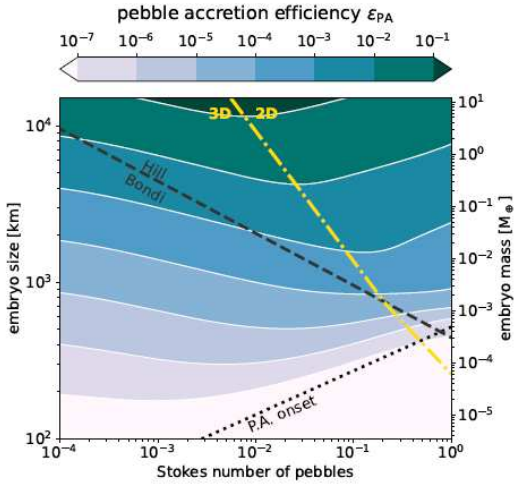

Figure 2.6: Efficiency of pebble accretion as a function of the planetary embryo size and the Stokes number (Drazkowska et al. [2023]).

2.1.3 From planetesimals to protoplanets: runaway growth (10 km to 100 km)

Mutual gravitational interactions between planetesimals become more important as their mass increase, since their effective cross section is much larger than their physical one. As a result, gravitational focusing starts to have a significant effect on collision probabilities. At the same time, dynamical friction transfers kinetic energy from larger to smaller planetesimals, keeping the relative velocity of the most massive bodies low and reducing the formation time scale. Assuming strong gravitational focusing, the planetary embryo's mass grows as (Rafikov [2003]):

$$\frac{1}{M_e}\frac{dM_e}{dt} \propto M_e^{1/3} \,, \tag{2.1.25}$$

indicating an acceleration in the embryo's growth as its mass increases. This corresponds to a phase of runaway growth, in which a few bodies grow rapidly at the expense of the others, leading to the formation of $\gtrsim 100$ km-sized bodies at 1 AU in some 10^4 yr. A complete model must consider whether collisions lead to accretion growth or to fragmentation, the overall outcome being determined by mass, impact velocity and parameters such as the intrinsic strength. If small fragments are produced as the outcome of collisions, they may have a second chance to be accreted by other planetesimals if the gaseous disk has not yet been dissipated, only if they do not drift inward too quickly to fall into the star. With the progressive formation of massive planets changing the velocity distribution through gravitational interactions, conditions are believed to develop from those more favourable to accretion into those more favourable for disruption. Recent

models (Lithwick and Wu [2014]) suggest that runaway growth ends with a trans-Hill stage, in which the larger bodies reach a Hill velocity matching the random speed of the small bodies they accrete. During this stage, the conglomeration can be categorised as collisionless (the smaller bodies rarely collide) or collisional (frequent collisions between the smaller bodies). The size spectrum for the size of the resulting bodies is of the form $dn/dR \propto R^{-4}$, strongly peaked for bodies having a smaller radius.

2.1.4 Oligarchic growth (100 km to 1000 km)

Oligarchic growth occurs when the runaway protoplanets become massive enough to affect the planetesimals random velocities by increasing their eccentricities and inclinations, with the transition happening typically when the mass of the protoplanets exceeds 100 times the average mass of planetesimals. The protoplanets can only perturb the orbits of planetesimals which are inside the growing planet's feeding zone, which size is set by the maximum distance over which its gravity is able to perturb other orbits sufficiently to allow collisions, scaling with the Hill radius. As the mass of the largest planetesimals grow, they perturb the velocities of smaller planetesimals in their vicinity, reducing the number of those which are available for accretion. This leads to a slowdown in the accretion rate once a certain isolation mass is reached, and runaway growth gives way to a phase of slower oligarchic growth: the largest objects still grow at the expenses of smaller bodies, but more slowly, and all roughly at the same rate. This slowdown occurs because, although the feeding zone expands as the planet mass grows, the number and mass of available planetesimals in the feeding zone rises more slowly. The isolation mass scales as:

$$M_{iso} \propto M_\star^{-1/2} \, \Sigma_p^{3/2} \, r^3 \, , \tag{2.1.26}$$

where Σ_p is the surface density of planetesimals at radial distance r. As an example, for $\Sigma_p = 100 \; kg/m^2$, conditions in the terrestrial planet region suggest an isolation mass of $\sim 0.07 \, M_\oplus$.
The oligarchic regime generates a bimodal population of planetary embryos and planetesimals: a small number of protoplanetary bodies and a larger number of small planetesimals. Planetary embryos are typically spaced from each other by 5-10 mutual Hill radii, where the mutual Hill radius of two bodies with masses m_i and m_j is defined as:

$$R_{H,i,j} = \frac{a_i + a_j}{2} \left(\frac{m_i + m_j}{3 M_\star} \right)^{1/3} \, . \tag{2.1.27}$$

If two embryos come closer than a few mutual Hill radii, they scatter each other and increase again their orbital separation. Typically, runaway growth may occur after $\sim 10^5$ yr when the relative velocities of the larger bodies fall into a low-velocity regime, and after $\sim 10^6$ yr this results in a number of relatively isolated protoplanets distributed throughout the disk. The resulting picture is of some hundreds of objects around 1000 km in size, with masses of 10^{22}-10^{23} kg, surrounded by billions of 1-10 km-sized planetesimals.

2.1.5 Giant impact phase (1000 km to 10000 km)

When the mass in relatively isolated protoplanets is comparable to the mass in planetesimals, and when there is insufficient damping of the protoplanets' eccentricities by dynamical friction, strong dynamical interactions lead to a more chaotic collision phase. Orbits of neighbouring embryos begin to cross, and their eccentricities and inclinations increase rapidly. Gravitational focusing weakens and the growth rate drops significantly. This stage, called post-oligarchic or chaotic, is characterized by giant impacts between planetary embryos, leading to the formation of several terrestrial planets, and defining the final architecture of the planetary system. Head-on collisions may lead to mergers with little mass loss, with large impacts causing extensive heating, the formation of magma oceans and possibly to connections between orbital properties (for example this happens for the eccentricities, mutual inclinations and orbit spacings of super-Earths).
The growing protoplanetary embryos, above $\sim$ 3000 km in size, are also characterized by their internal melting and differentiated interiors, with denser elements sinking in the core and the lighter floating above. Mergers proceed until orbit spacings become large enough to be quasi-stable, with the final assembly of terrestrial planets taking $\sim$ 10-100 Myr. The final size of terrestrial planets depends on numerous factors, amongst them the initial conditions, the viscosity of the protoplanetary disk, the surface density of protoplanets and the presence of giant planets. In the Solar System, for example, simulations show that the oligarchic and post-oligarchic stages are strongly influenced by the presence of Jupiter and Saturn. Numerical simulations also suggest that the Earth reached half of its current mass in 10-30 Myr, and its present mass in $\sim$ 100 Myr, with the growth rate declining exponentially with time. Numerical simulations of terrestrial planet formation (Hoffmann et al. [2017]) show that, as a result of the chaotic evolution of the embryos' trajectories, pratically identical initial conditions can result in a wide range of final planetary configurations, but some global properties can still emerge. Generally, systems with giant planets tend to form fewer, more massive, and more eccentric terrestrial planets at smaller semi-major axes than those without, while configurations with giant planets on eccentric orbits produce fewer and more massive terrestrial planets on tighter orbits than those with giants in circular orbits. The formation of terrestrial planets follows this bottom-up scenario, and Figure 2.7 shows the results of an N-body simulation exemplifying this process.

2.1.6 Giant planets formation

Giant planets, generally defined as those with masses $\geq 0.1\ M_J$, span a wide range of masses, orbits and compositions, encompassing both the gas and ice giants of the Solar System and the close-in hot Jupiters. Their typical gas envelopes provide a temporal constraint: they must form rapidly, within $\sim$ 5–10 Myr, before the protoplanetary disk dissipates. If the gas dispersal is faster than core formation, ice giants rather than gas-rich giants may form. Two formation

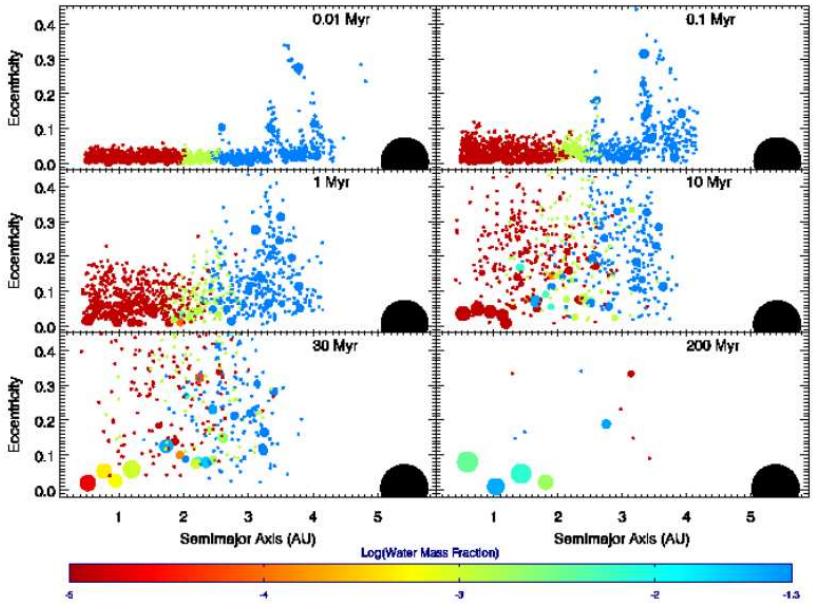

Figure 2.7: Snapshots in time for an N-body simulation of terrestrial planets formation. Jupiter is represented as a large black circle (Raymond et al. [2009]).

models for giant planets are currently explored: the core accretion model and the disk instability model. The former begins, as for terrestrial planets, with planetesimal coagulation forming a massive core of about 5-20 $M_\oplus$, followed by the accretion of a gaseous envelope. In the latter, gas giant are supposed to form as a result of gravitational fragmentation in the protoplanetary disk. However, core accretion and disk instability are not necessarily competing processes, as the latter is likely most common during the early phases of disk evolution (few 10^5 yr) while the former occurs at later stages (few Myr). Core accretion may be the dominant mechanism for ice giants and low-mass gas giants, while disk instability may be significant for the high end of the mass distribution.
The core accretion model (Figure 2.8), a bottom-up process, starts with the formation of a massive planet core, followed by the core's rapid accumulation of a massive gas envelope. This process is generally considered as taking place in four distinct phases, which may be modified by the effects of migration.

- Primary core accretion: this phase is the same of terrestrial planets formation, leading to the formation of a massive core in the mass range $\sim$ 5-20 $M_\oplus$, capable of retaining a gaseous atmosphere. The core accretes planetesimals until it reaches the isolation mass. The envelope mass also grows, but it remains a small fraction of the core mass. Generally, in the inner part of the disk there are insufficient solids to allow such massive cores to develop, but the situation is more favourable beyond the snow

line, where the temperature is low enough for the formation of ices. This, combined with the reduced gravitational dominance of the central star, allows massive solid cores to form more easily.

- Slow envelope accretion: characterized by a slowly increasing accretion of gas onto the core, which starts when the gravitational energy at the surface becomes larger in magnitude than the thermal energy of the nearby gas, along with the continued accretion of residual planetesimals. Over the period of a few Myr, the growing core eventually reaches a critical core mass, beyond which the gas accretion rate exceeds that of planetesimals.

- Rapid gas accretion: this is triggered if the envelope reaches a mass comparable to the core mass. It is characterized by runaway accretion of the surrounding gas, with relatively little accretion of solids. Once the envelope mass exceeds a few percent of $M_\oplus$, a combination of gas drag, evaporation and dynamical pressure makes difficult for the planetesimals to arrive intact to the core boundary, and a significant mass fraction dissolves in the gas envelope, enriching it in high-Z elements.

- Contraction and cooling: this is the end of gas accretion, either due to the opening of a disk gap or because the gas disk dissipates. The last stage of the evolution is characterized by a sequence of contractions and coolings at constant mass to its present state. The main energy source is slow contraction in hydrostatic equilibrium together with heating due to to planetesimals accretion, while an energy sink arises from cooling by radiation.

This scenario can explain a wide range of planetary architectures, including the Solar System giants, and many of the exoplanet giants orbiting within $a \lesssim$ 10-50 AU. Core accretion starts with an embryo of $\sim$ 0.01-0.1 $M_\oplus$ accreting planetesimals, and the accretion rate is approximated by the Safronov equation (Safronov [1972]):

$$\dot{M}_{core} = \pi R_{capt}^2 \sigma_s \Omega F_g \ , \tag{2.1.28}$$

where πR_{capt}^2 is the geometrical capture cross section, Ω is the orbital frequency, σ_s is the solid surface density of the disk and F_g is a gravitational enhancement factor, which in the two-body approximation can be written as:

$$F_g = 1 + \left(\frac{v_e}{v}\right)^2 \ , \tag{2.1.29}$$

where v_e is the escape velocity from the embryo and v the relative velocity between the embryo and the accreting planetesimal. If no gas is present, $R_{capt} = R_{core}$, while in the presence of an envelope $R_{capt} > R_{core}$. The gravitational influence of the embryo excites the velocities of the planetesimals, reducing F_g. In the absence of migration, the parameters most influencing formation are σ_s, $M_\star$ and a, which together determine the isolation mass (Pollack et al. [1996]):

$$M_{iso} = \frac{8}{\sqrt{3}} \sqrt{\frac{\pi^3 C^3}{M_\star}} \sigma_s^{3/2} a^3 \ , \tag{2.1.30}$$

which gives the maximum mass to which the embryo can grow, having accreted all the planetesimals in its feeding zone, with C being the number of Hill sphere radii on each side of the planet included in the feeding zone. M_{iso} must exceed $\sim 3M_{\oplus}$ for accretion to deliver a Jupiter-mass object during the disk lifetime. Gas from the protoplanetary disk can become bound to a planetary core of mass M_c if, in the frame of the core, its total energy becomes negative. Indicating with v_{rel} and v_{th} the relative (to the core) and thermal velocities of the gas, this condition requires that:

$$\frac{GM_c}{R} \geq \frac{v_{rel}^2 + v_{th}^2}{2} \ . \tag{2.1.31}$$

In this case, the gas which is below the radius R can become bound. The envelope accretion is also influenced by the Hill radius and the Bondi radius $R_B = GM_p/c_s^2$, with c_s the sound speed. For a forming planet in a protoplanetary disk, gas must fall into its Bondi sphere to accrete. Simulations of the gas flow around a planet embedded in a disk show that not all the gas flowing through the Hill radius is accreted by the planet (Lissauer et al. [2009]), and an effective outer radius can be defined as:

$$R_{eff} = GM_p \left(c_s^2 + \frac{GM_p}{0.25R_H} \right)^{-1} \ . \tag{2.1.32}$$

As gas accretes onto the core, and the envelope density and temperature increases, the resulting pressure gradient tends to oppose further accretion by inhibiting envelope contraction. Only by cooling the envelope can accrete further gas and grow, and in this stage the temporal evolution is controlled by the timescale of the Kelvin-Helmholtz cooling of the envelope. When the core mass reaches the critical core mass, the hydrostatic equilibrium is broken and both planetesimal and gas accretion increase exponentially. At this stage, the radiative losses from the envelope can no more be compensated by the accretion luminosity from the impacting planetesimals alone. Thus, the envelope has to contract, so that the new gas can stream in, which in turn increases the radiative losses. This runaway gas accretion builds up a Jupiter-like massive envelope in a timescale of the order of a few thousand years. The termination of rapid gas accretion may result from disk dissipation or from gap opening. For the former, the disk evolution involves a gradual reduction of disk mass and density over 2-4 Myr, after which a relatively rapid (few 10^5 yr) clearing phase occurs. For the latter, even after gap opening the gas can flow across it and accrete onto the planet, but at a decreased rate. Also planet-disk interactions can excite eccentricities and increase $\dot{M}_{env}$ even after the formation of a gap. The formation timescales predicted by the core accretion model were comparable to or exceeding the lifetime of protoplanetary disks, but they are significantly reduced including effects such as pebble accumulation, which can speed up the solid core accretion phase and core inward migration due to its interaction with the disk, which allows it to access new material in the growth phases. The estimated timescale for giant planets formation is thus $\sim 10^4$-10^6

yr. Following the end of accretion, the planet slowly contracts and cools at constant mass over many Gyr, together with a progressive decline in luminosity over time. For giant planets close to their host stars, additional energy sources lead to a larger radius than for an low-irradiation planet at any given time.

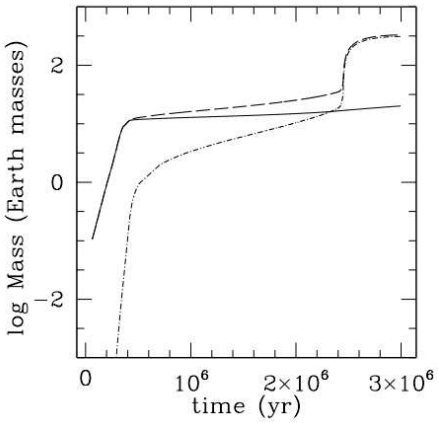

Figure 2.8: Growth of a protoplanet via core accretion. The solid line represents the core mass, the dash-dot line the envelope mass, and the dashed line the total mass. From Helled et al. [2013].

Gravitational disk instability

This top-down model supposes that giant planets can form, more directly, by contraction of gaseous condensations in a massive self-gravitating disk. This mechanism would avoid various problems in the progressive accumulation of solids, from sub-μm scales upwards. The process is based on a rapid, large single-step collapse in a massive, gravitationally unstable protoplanetary gas disk, which then leads to the formation of gas giant protoplanets. Thin accretion disks become gravitationally unstable at large radii, and the instability is determined by the value of the Toomre parameter Q (2.1.2), with $Q > 1$ indicating stability and $Q \sim 1$ indicating marginal instability (Figure 2.9). Marginal unstable disks will evolve through the formation of spiral density waves, which would transport angular momentum, thus enhancing stability, but also leading to dissipation and heating, thereby rising the sound speed and enhancing fragmentation. The evolution of gravitational instabilities in disks is controlled by gas cooling. If the local cooling timescale is larger than $2\pi/\Omega$, the internal energy produced by the instability and heat loss nearly balance each other out, and the instability may be sustained in a nearly steady-state. However, if the cooling timescale becomes $\lesssim 2\pi/\Omega$, the balance is broken and the disk can fragment into self-gravitating clumps. Detailed simulations (e.g. Riols and Latter [2016]) have confirmed that massive ($\geq 0.1\,M_\odot$) protoplanetary disks should cool rapidly enough to become gravitationally unstable, and to fragment beyond a few tens

of AU, while fragmentation appears less likely to produce giant planets around solar-type stars at $\lesssim$ 40 AU. In contrast to the core accretion model, giant planet formation is extremely fast in this model, as it occurs on a dynamical timescale.

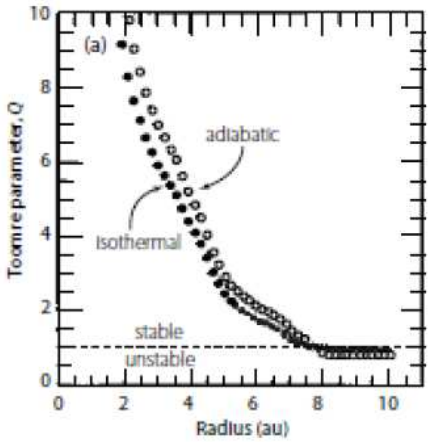

Figure 2.9: Toomre Q stability parameter as a function of the distance from the protostar for both locally isothermal and locally adiabatic models (Boss [1997]).

2.1.7 Planetary migration

The formation model described above presents some inconsistencies when applied to the currently known population of exoplanets. For example, it cannot explain the presence of giant planets orbiting close to their host stars, the so-called hot and warm Jupiters, since they are expected to form beyond the snow line, which, for Sun-like stars, typically lies beyond 3–4 AU. More generally, challenges arise from the large number of planets found at $a \lesssim 0.2$ AU, where high temperatures and the limited availability of protostellar material would preclude in situ accretion. Additionally, the model fails to account for the many planets with very high eccentricities, as formation within a protoplanetary disk is expected to produce nearly circular orbits, similar to those in the Solar System. Many of the observed deviations from the classical model can be at least partially explained by the effects of orbital migration. The main mechanisms responsible for this, gas disk migration and planet-planet scattering, will be discussed below. However, it is important to note that migration can also hinder planet formation: if it occurs on a timescale shorter than the core growth timescale, planetary embryos may fall into the star before they can significantly grow.

Gas disk migration

A planet moving through the gas disk excites spiral waves of density within it, and the torque exerted by the perturbed disk drives gap opening and orbital migration. Both the speed of migration, as well as its direction depend on the planet mass, and on the disk properties near the planet's orbital radius. In all cases, the migration must take place while the disk of gas and dust is still present, namely during the first 3-5 Myr of the host star's life. Excited density waves are particularly strong at the locations of the corotation and Lindblad resonances (Binney and Tremaine [2008]), and the planet experiences a torque exerted by each of them. For a planet on a circular orbit with angular frequency Ω_p, the corotation resonance exists at a radius in the disk where $\Omega = \Omega_p$, with Ω the angular frequency of the disk at that radius. Inner and outer Lindblad resonances happen for:

$$m(\Omega - \Omega_p) = \pm\kappa_0 \ , \tag{2.1.33}$$

where m is an integer and κ_0 is the epicyclic frequency (equal to Ω for a Keplerian disk). Several regimes of migration are distinguished, depending mainly on the planet to primary mass ratio, with type I migration applying to planets up to 10-20 $M_\oplus$, giant planets carve a deep gap around their orbit experiencing a type II migration and subgiant planets that open a partial gap may undergo type III migration in more massive disks (Figure 2.10). More in detail:

- type I migration is when, during the evolution of the planet's orbit, the gas surface density profile remains approximately unperturbed. The torque acting on type I migrating planets has two main components: the differential Lindblad torque and the corotation torque, and the combination of the two generates a wake (spiral density wave) in the disk. For typical density and temperature profiles, the Lindblad torque is negative: by itself, it would make the planet migrate inwards on a timescale much shorter than the life of the disk. The corotation torque (or horseshoe drag), accounting for the angular momentum exchanged between the planet and the disk within the co-orbital region, may lead to outwards migration and slows down the inward migration due to Lindblad resonances. It is also sensitive to the gradient in thermal properties over the region where gas particles describe an U-turn motion in proximity of the planet. For a 3D isothermal gas with surface profile $\Sigma(r) \propto r^{-\gamma}$, the migration time scale is given by:

  $$\tau_I = \frac{1}{2.1 + 1.1\gamma} \frac{M_\star^2}{M_p r_p^2 \Sigma(r_p) \Omega_p} \left(\frac{c_s}{r_p \Omega_p} \right)^2 , \tag{2.1.34}$$

  where $\Sigma(r_p)$, c_s and Ω_p are respectively the gas surface density, the sound speed and the angular velocity at the location of a planet orbiting at distance r_p (Tanaka et al. [2002]).

- More massive planets undergo type II migration and carve a larger gap in the disk. Type II migration provides a mechanism to transport gas giants that must form beyond the snow line inward to their host star, occurring

at the viscous speed of the disk and increasing the material that can be captured in a giant planet's envelope. Two conditions are required for gap formation: that the radius of the planet's Hill sphere is larger than the thickness of the gas disk and that the tidal torques must remove gas from the gap faster than viscosity will allow it to be replenished. These two conditions imply $M_p \gtrsim$ 20-40 $M_\oplus$, depending on the disk structure and on the distance from the host star. Once the gap is opened, orbital evolution occurs on the same timescale as the viscous timescale of the disk, giving a type II migration time scale of:

$$\tau_{II} = \frac{1}{3\alpha\Omega_p}\left(\frac{r_p}{h}\right)^2 , \tag{2.1.35}$$

(Papaloizou and Terquem [2005]) where α is the Shakura–Sunyaev viscosity parameter, yielding a time scale on the order of 10^5–10^6 yr.

- For a smooth initial density profile in the disk and a small density gradient at the corotation radius, the corotation torques are less pronounced than those coming from the Lindblad resonances. If the planet is massive enough to carve a small gap in the disk, a migration rate-dependent torque exists, depending on two quantities: the coorbital mass deficit δM, the mass that would need to be added to the corotation region so that the surface density there is equal to the average one of the gas flow, and the sum of the planet mass and the mass of the disk, M_{tot}. When $\delta M > M_{tot}$, type III migration, or runaway migration, occurs (Nelson [2018]).

The disk torques can also alter the orbital eccentricity and inclination of the migrating planet. Whether eccentricities undergo growth or decay depends on the relative strengths of Lindblad resonances (which increase the eccentricity) and corotation resonances (which damp the eccentricity). In conclusion, migration by interaction with the disk may explain the existence of the numerous exoplanets orbiting on short periods.

Figure 2.10: The three types of gas disk migration.

Planet-planet scattering

Gravitational interactions between planets in the same system can lead to planet–planet scattering, both during and, more significantly, after the dissipation of the protoplanetary disk (Weidenschilling and Marzari [1996]). The onset

of instability can occur on short timescales (a few 10^3 years) or over several billions of years, depending on the initial orbital radii, separations, planetary masses, and eccentricities. Additional mechanisms that may trigger dynamical instability include convergent migration, disk dispersal and the associated loss of its damping effect on planetary orbits, as well as perturbations from close stellar encounters within a cluster.
When instability onsets, the eccentricities grow and the planets are driven into crossing orbits, leading to close encounters. This period of chaotic evolution ends when one or more planets are ejected out of the system on hyperbolic orbits and the remaining planets are on eccentric but stable orbits (Figure 2.11). This process explains the presence of exoplanets with a high eccentric orbits, but it also produces rogue planets and leads to a modest semi-major axis inward migration (as a consequence of the conservation of energy).

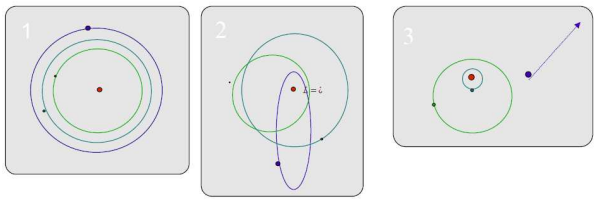

Figure 2.11: Planet–planet scattering dynamics in a three-planet system. (1) The system approaches instability; (2) chaotic evolution with orbit crossing; (3) end of the chaotic phase marked by the ejection of one planet on a hyperbolic trajectory (Marzari [2023]).

2.2 Exoplanet Zoo

The observed exoplanet population exhibits a wide variety of properties, including orbital parameters and compositions. Many exoplanets have highly elliptical orbits, with $e \gtrsim 0.3$. Among those with estimated masses, a significant fraction orbits their host star at close distances ($a \lesssim 0.2$ AU), including many hot giants. Others, instead, are found at distances exceeding 100 AU. While no single, universally accepted classification system for exoplanets exists, various classification schemes have been proposed based on different planetary properties. One of those classification is based on the planets' radius (Borucki et al. [2011]), a key parameter for the transit method:

- Earth-size, or terrestrial planets: $R < 1.25\,R_\oplus$,
- super-Earth-size: $1.25 - 2\,R_\oplus$,
- Neptune-size: $2 - 6\,R_\oplus$,
- Jupiter-size: $6 - 15\,R_\oplus$.

Other methods, such as radial velocity and microlensing, rely on the (projected) planetary mass as the key observable. A classification based on mass has been proposed by Plávalová and Rosaev [2024]:

- Mercury class planets: $M < 0.22\,M_\oplus$,
- Earth class planets: $0.22 - 2.2\,M_\oplus$,
- Super-Earth or Sub-Neptune class planets: $2.2 - 22\,M_\oplus$,
- Neptune class planets: $22\,M_\oplus - 0.4\,M_J$,
- Jupiter class planets: $0.4 - 14\,M_J$,
- Brown dwarfs: $M > 14\,M_J$.

Figure 2.12 shows the mass–radius and eccentricity–period distributions of confirmed exoplanets, highlighting the wide diversity of properties that characterize the exoplanet population.

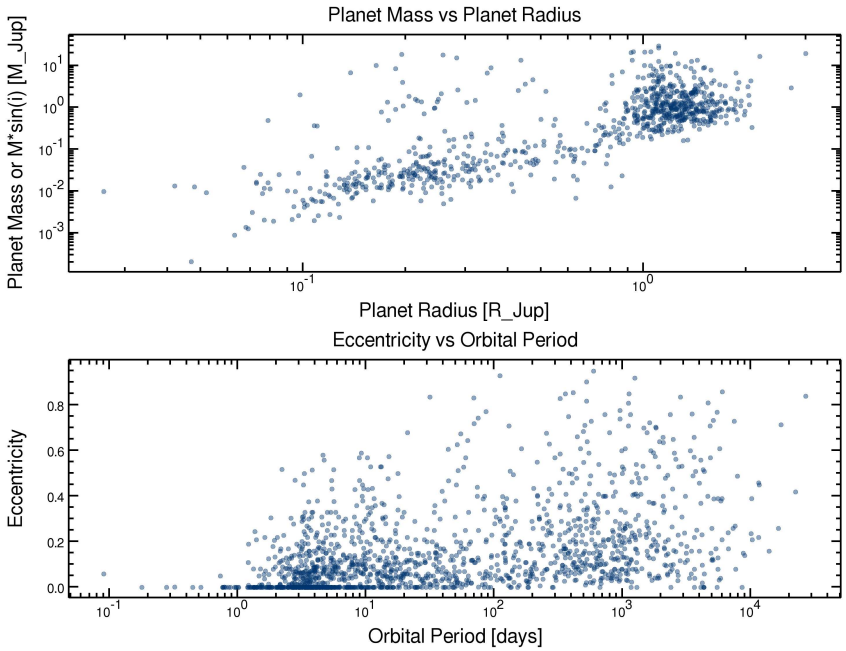

Figure 2.12: *Upper panel*: mass-radius distribution of confirmed exoplanets. *Bottom panel*: eccentricity-period distribution of confirmed exoplanets. Source: NASA Exoplanet Archive.

To compare statistically the predictions of planet formation models with the observed exoplanet distributions, population synthesis models have been developed. The aim of these models is to simulate with a numerical code the history

of planet formation from the protoplanetary disk to the final systems, for a given set of initial parameters (Figure 2.13). The outcomes of a large number of simulations are then statistically compared with the observed population, in order to better understand the processes involved in planet formation and to interpret the characteristics in the orbital and mass distributions of known exoplanets.

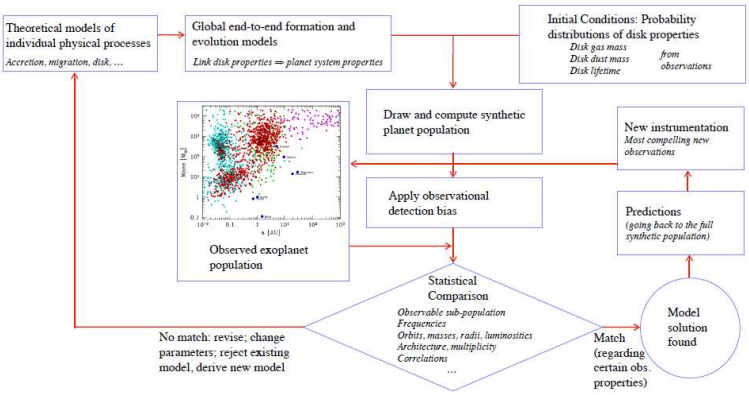

Figure 2.13: Elements and work flow of a planetary population synthesis model (Burn and Mordasini [2024]).

An example of a population synthesis model is the Generation III Bern model (Emsenhuber et al. [2021]), able to obtain precise results that accurately describe the observed population of exoplanets. Based on the core accretion paradigm, the Bern model, a global model of planet formation and evolution, studies the growth of several lunar-mass protoplanetary embryos embedded in protoplanetary disks around a solar-type star. The disk model is based on viscous angular momentum transport and the turbulence is characterized by the Shakura-Sunyaev approach. The initial mass of the disk depends on the star metallicity and also on the condensation state of the molecules in the disk. In this case the formation stage timescale, which includes N-body interactions, is fixed to 100 Myr. As a simplification, the model starts with all the solids in the form of planetesimals, and so does not account for the presence of dust. The resulting planets can be distinguished between five compositions: Jovian (H/He dominated in mass), Neptunian (volatile ice-rich with H/He), water worlds (volatile-rich without H/He), hyterran (silicate-iron core with H/He envelope) and terrestrial (silicate-iron without H/He or ices). Inspecting, instead, the final planetary systems, the emerging architectures can be divided into four main classes (Emsenhuber et al. [2023]). These are, ordered in increasing typical mass of formed planets: ordered Earths and ice worlds systems, migrated sub-Neptune systems, mixed systems with low-mass and giant planets (like the Solar System), and dynamical active giants. Analyzing the frequency of the different classes, it is found that most systems contain only low-mass planets (the first two classes), while only $\sim 20\,\%$ of the systems are in classes

that contain giant planets (the last two). However, these numbers are sensitive to the choice of initial conditions, which are subject to uncertainties. Although this model accurately reproduces several aspects of the observed exoplanet population, it also presents various limitations and inconsistencies. For example, it fails to form accurately the Solar System, mainly because in this model gas accretion is assumed to remain unaffected by gap formation, and this leads to the formation of systems more massive than the Solar System. Furthermore, a comparison between the planet population generated by the Bern model and a sample of planets taken from the Kepler mission (Chen et al. [2024]) shows that the synthetic results for sub-Neptunes and super-Earths are higher than the observational results, which imply that the planet population generated by the Bern model contains larger fractions of water-rich planets comparing to the Kepler sample.
While the Bern model is a theoretical population synthesis model based on numerical simulations, another approach (Mishra et al. [2023]) is a classification method focused on observed systems. It requires the introduction of two parameters: the coefficient of similarity (C_S) and the coefficient of variation (C_V). The first measures how a planetary quantity (such as mass, size and eccentricity) changes from one planet to another, inside-out. Denoting by q the specific quantity (and q_i its value for the i^{th} planet in a system), the coefficient of similarity for a system of n planets is defined as:

$$C_S(q) = \frac{1}{n-1} \sum_{i=1}^{n-1} log \frac{q_{i+1}}{q_i} \ . \tag{2.2.1}$$

It measures the average order of magnitude variation in the quantity q from one planet to another. If $C_S(q)$ is positive, then planets within a systems are ordered in q. Instead, if $C_S(q)$ is negative, the planets are anti-ordered. The coefficient of variation is used to measure the magnitude of variation in a set of planetary parameters, and it is defined as:

$$C_V(q) = \frac{\sigma(q)}{\bar{q}} \ , \tag{2.2.2}$$

the ratio between the standard deviation and the mean of the quantity q. It is positive defined and planetary systems consisting of planets that have a small (large) variability in their q_i values will have a small (large) value of C_V.
The different architectures can be categorized with respect to their values of C_S and C_V for the planetary masses, in the following way:

- Anti-ordered ($C_S(M) < -0.2$): planetary systems where the planetary mass shows an overall decrease with distance have an anti-ordered architecture. Many currently known single hot/warm Jupiter systems may host additional small, distant and yet undetected planets, revealing an anti-ordered architecture. In the Bern model, the radius distribution of this class peaks for rocky and super-Earth planets mainly outside 10 AU, making their detection very challenging.

- Ordered ($C_S(M) > 0.2$): planetary systems where the planetary masses show an overall increase with distance have an ordered architecture, and the increasing mass can be monotonic (e.g. TOI-561; Lacedelli et al. [2021]) or non-monotonic (e.g. the Solar System). The observations are generally biased against discovering small and less massive planets which orbit far away from their host star, making this architecture class very common between the observed systems.

- Similar ($|C_S(M)| \leq 0.2$ and $C_V(M) \leq \frac{\sqrt{n-1}}{2}$): planetary systems have a similar architecture when all planets in the system have masses that are approximately similar to each other. This architecture is also the most common outcome of planetary formation. The radius distribution of similar systems implies that they are mainly composed of rocky planets, super-Earths and sub-Neptunes. An example of a planetary system having a similar architecture is Trappist-1 (Gillon et al. [2016]).

- Mixed ($|C_S(M)| \leq 0.2$ and $C_V(M) > \frac{\sqrt{n-1}}{2}$): planetary systems where the planetary masses, inside-out, show broad increasing and decreasing variations have mixed architecture. The Bern model's synthetic mixed architecture systems tend to have numerous Earth-mass planets outside 10 AU, thus inaccessible to most exoplanet detection techniques. However, these systems are also composed of super-Earths, sub-Neptunes, Neptunes and Jovian planets. An example of a planetary system having a mixed architecture is Kepler-89 (Weiss et al. [2013]).

2.2.1 Earths and Super-Earths

Terrestrial planets and, in particular, super-Earths, are the most abundant class of planets known to date. Results from radial velocity and transit surveys show indeed that roughly half of all Sun-like stars observed appear to possess one or more planets with $R = 1\text{-}4\,R_\oplus$ and $P \lesssim 100$ d. Limiting to planets with $P \lesssim 50$ d and $M = 3\text{-}30\,M_\oplus$, two independent Doppler surveys found the occurrence rate to be $15 \pm 5\,\%$ (Howard et al. [2010]) and $27 \pm 5\,\%$ (Mayor et al. [2011]). For the same period range and planets with $R = 2\text{-}4\,R_\oplus$, Kepler data gave an occurrence rate of $13.0 \pm 0.8\,\%$ (Howard et al. [2012]). The surveys also agree that, within this range of periods and planet sizes, the occurrence rate is higher for smaller planets, roughly according to power laws of the form:

$$\frac{dn}{d\log m} \propto m^{-0.5}\,, \quad \frac{dn}{d\log R} \propto R^{-2}\,. \tag{2.2.3}$$

A key objective of exoplanetary science is to determine the occurrence rate of Earth-like planets orbiting Sun-like stars at distances that allow for the presence of liquid water on their surfaces, a quantity denoted as eta-Earth ($\eta_\oplus$). However, estimates of this value vary significantly across different studies. An important early estimate was provided by Petigura et al. [2013] (Figure 2.14), who analyzed a sample of bright Sun-like stars from the Kepler catalogue (defined as having

Kepler magnitude between 10 and 15, T_{eff} between 4100 and 6100 K, and surface gravity $\log g$ between 4.0 and 4.9). The search focused on Earth-like transiting planets, defined as those with radii between 1 and 2 $R_\oplus$ and incident fluxes between 0.25 and 4 $F_\odot$. Their study yielded an estimated occurrence rate of potentially habitable Earths of $\eta_\oplus = 22 \pm 8\,\%$.

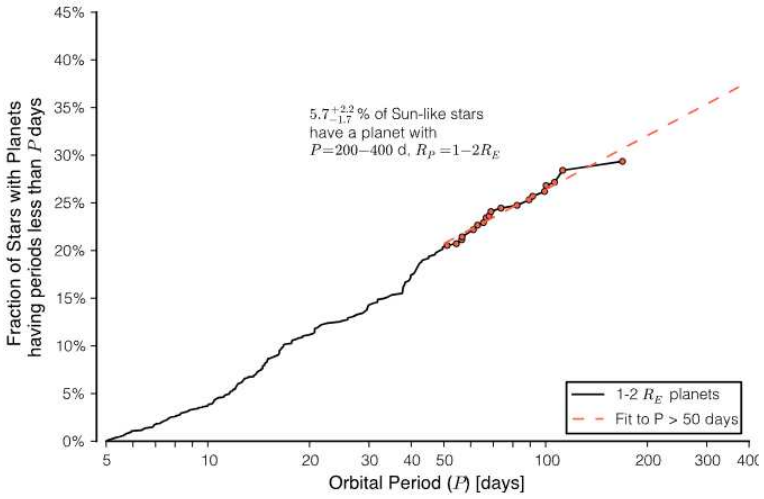

Figure 2.14: The fraction of stars having nearly Earth-size planets ($R \approx$ 1-2 $R_\oplus$) with any orbital period up to a maximum period P (Petigura et al. [2013]).

More refined estimates have been provided by later studies, such as Barbato et al. [2018a] and Zink and Hansen [2019]. The first study, based on a sample obtained by cross-matching Gaia DR2 and Kepler, defines Earth-like planets as those with R_p = 1-1.75 $R_\oplus$ and F = 0.2-2 $F_\odot$. It reports an occurrence rate of $\eta_\oplus = 20.88^{+25.74}_{-8.22}$ % when considering only confirmed Earth-like planets, and $\eta_\oplus = 35.01^{+25.00}_{-15.66}$ % when including candidate planets. The second study, using a stellar sample from Kepler DR25 with corrections from Gaia DR2, includes stars with T_{eff} between 4200 and 6100 K, $\log g \geq 4$, and $R_\star \leq 2\,R_\odot$. Defining potentially habitable planets as those with masses between approximately 0.3 and 4 $M_\oplus$, radii between 0.72 and 1.7 $R_\oplus$, and orbital distances between 0.95 and 1.68 AU, the estimated occurrence rate is $\eta_\oplus = 34 \pm 2\,\%$. This study also suggests that $6.4 \pm 0.5\,\%$ of Sun-like stars could host more than one habitable planet, while $0.036 \pm 0.009\,\%$ might contain as many as five habitable planets. More recent results, based on data collected from Kepler (Bergsten et al. [2022]), estimate the occurrence of Earth-sized planets in the habitable zone of FGK stars as $15^{+6}_{-4}\,\%$, with the Kepler's poor sampling of small planets at long orbital periods being the primary source of uncertainty. Contrary to giant planets, Earth-sized planets are common around M dwarfs. An analysis conducted by Gaidos et al. [2016], based on Kepler data, shows that, on average, each M dwarf from their sample hosts 2.3 ± 0.3 planets with radii of 1-4 $R_\oplus$

and $P < 180$ d. The same study also reveals that M dwarfs often host compact systems of multiple planets. Although, as stated before, super-Earths represent the most abundant class of known planet, they are absent in the Solar System. Many hypotheses have been proposed to explain this absence, among them one states that this may be related to the blocking of the inward migration of more distant embryos by Jupiter, or this could be due to the initial distribution of embryos.

Super-Earths are often found in multi-planet systems. These multiple-planet systems are usually tightly packed (called STIPS, Systems of Tightly-packed Inner PlanetS), with spacing ranging from 10 to 30 Hill radii. Although some of these multiple-planet systems occupy mean motion resonances, most of them have period ratios unassociated with any resonance. This could be explained taking into account the disk turbulence, which prevents resonance capture, or the large eccentricities of the migrating planets. In this second possibility, planets are captured into resonances but they escape on timescales shorter than the migration timescale. Several models have been developed to explain the origin of super-Earths, of which two remain viable: the migration and drift models (Izidoro and Raymond [2018]). In situ growth has been discarded: if it was the case, then they must grow extremely quickly because of the very dense disks required to have many Earth masses of solids so close-in. Yet if planets form that quickly in massive gas disks, they must migrate: the disks are so dense that aerodynamic drag acts on full-grown planets on a timescale shorter than the disk dissipation timescale. Thus, in situ growth implies that the planets must migrate.

Also population synthesis models have been used to find correlations between the architecture of a planetary system and the presence of an Earth-like planet. Key quantities related to the presence of an Earth-like planet are the architecture and properties of the innermost detectable planet (IDP). Around G-type stars, low-mass systems (in which the most massive planet has $M \leq 20\,M_\oplus$) with $R_{IDP} > 2.5\,R_\oplus$ or systems with a single known planet ($n = 1$ planets) of $M < 100\,M_\oplus$, $R > 8\,R_\oplus$ or $P > 30$ d are the systems that show the higher probability to host a Earth-like planet. In contrast, anti-ordered, ordered, mixed, and $n = 1$ systems with an IDP too massive or too large are the systems that show the least probability. For early-M stars the results are the same as for G stars, while for late-M if a system falls into the low-mass or $n = 1$ category, it is highly likely to host an Earth-like planet.

By combining radial velocity and transit data, density measurements and thus insights on the compositions of Earth-like planets and super-Earths is possible, even with high uncertainty. Focusing on planets with $R < 4\,R_\oplus$, results show remarkably diverse bulk densities, implying that these planets must have a wide range of compositions even if they have similar masses, differently from the Solar System, where planets of comparable mass share similar bulk density and composition. Terrestrial planets are considered to have secondary atmospheres, generated through outgassing or comet impacts, in contrast to the giant planets, whose atmospheres are primary, captured directly from the original solar nebula.

2.2.2 Neptunes and Sub-Neptunes

The distinction between super-Earths and sub-Neptunes is not sharp and depends on several physical properties. Low-mass planets with sizes between 1-4 $R_\oplus$ are classified as super-Earths (predominantly rocky) or sub-Neptunes (with a significant mass fraction in volatile ices and a H_2/He envelope) depending on their compositions, which is in turn based on their densities. In addition to radius and composition, mass plays an important role in distinguishing sub-Neptunes, which typically range from a few to around 20 $M_\oplus$. Several studies predicted the presence of water worlds, with substantial mass fractions of H_2O and potentially habitable, with atmospheres dominated by N_2, H_2O and CO_2: on example of such a planet is K2-18b, a temperate sub-Neptune which could allow for liquid water underneath its H_2/He atmosphere (Piette and Madhusudhan [2020]).
For planets with $P < 100$ d, the occurrence rate density $dn/d\log R$ shows a dip centered on $\sim 1.7\,R_\oplus$ (Figure 2.15; Fulton et al. [2017]), which location is often used as the dividing line between super-Earths and sub-Neptunes. This is conventionally interpreted as the result of the loss of the primordial H/He envelopes atop rocky cores, due to the high irradiation from the close host star. However, another possible explanation is that the sub-Neptunes are water-rich. Such large water contents are a prediction of planet formation models, leading to migration of ice-rich planets from outside the water condensation line towards the star. In the case of water-dominated outer layers of the planet, the phase of water determines the precise radius. For close-in planets, water forms a hot (to a large degree supercritical) vaporized hydrosphere, which increases the radius compared to condensed, solid, high-pressure ice. A combined formation and evolution model considering the different water phases between super-Earths and sub-Neptunes demonstrated the emergence of the radius valley as a separator between dry and wet planets formed, respectively, within or beyond the ice line. The main driver of this dichotomy is varying pebble accretion efficiency based on pebble composition, which produces smaller rocky and larger icy cores. In this model, the radius valley is a hybrid consequence of both formation (migration leading to the sub-Neptune peak) and evolution (evaporation leading to the super-Earth peak) (Burn et al. [2024]).
There is also a connection between the composition of such planets and the formation place: at larger distance from the star more solids are available for accretion, leading to growth up to several $M_\oplus$, where migration is more efficient. Thus, planets migrate in the inner region, where they collide with smaller rocky planets. Collisions with other bodies, or the radiation flux of the host star, can lead to the expansion and Roche lobe overflow of the gaseous envelope, and thus remove the H/He content, but it is not the case for water. These process therefore can give rise to a population of planets with pure water envelopes. More massive planets or those located at larger distances share a similar formation history but they are not stripped completely of H/He. During the evolution stage, planets cool and are subject to photoevaporation, which reduces their size. The most frequent evolutionary pathway is the loss of a H/He atmosphere

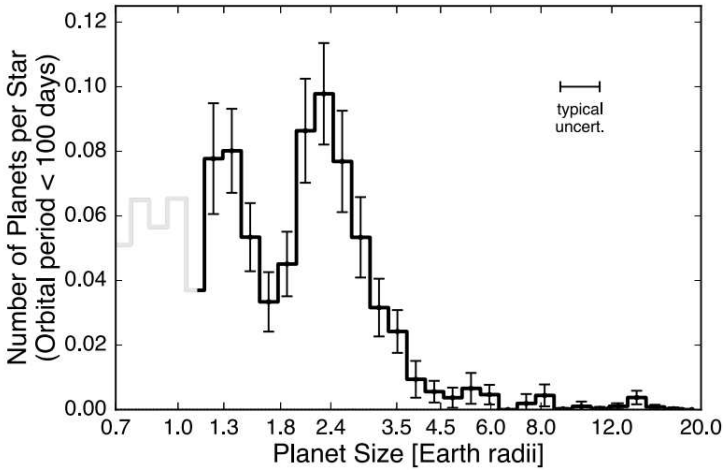

Figure 2.15: Occurrence rate density of planets with orbital periods shorter than 100 days and radii $R \leq 20\ R_\oplus$. The dip around 1.7 $R_\oplus$ appears to separate super-Earths from sub-Neptunes (Fulton et al. [2017]).

from a rocky core. A mixed or water-dominated envelope can also be lost completely, resulting in a bare, rocky core.

Both Doppler and transit surveys found a very low occurrence rate for planets with periods shorter than a few days and with radii between 2-6 $R_\oplus$ or masses between 10-100 $M_\oplus$ (Mazeh et al. [2016]), a region known as the Neptunian desert. Several hypotheses have been proposed to explain this distribution. Among them, the most widely supported involves photoevaporation driven by stellar irradiation. In this scenario, these planets (hereafter referred to as hot Neptunes) are subject to intense radiation from their host star, which strips away their gaseous envelopes. Thus, they lose a substantial fraction of their mass and can no longer be considered giant planets. This may also explain why the terrestrial planet population does not exhibit a similar depletion. A study from Dong et al. [2018], based on Kepler data, tries to better define and characterize those planets. They found that hot Neptunes, like hot Jupiters, are preferentially hosted by metal-rich stars, and the frequency is correlated with the [Fe/H] value of the host star, strongly increasing for $[Fe/H] \geq 0.1$. Furthermore, hot Neptunes tend to preferentially exist in Kepler's single transiting planetary systems, more in detail the $73 \pm 9\,\%$ of all those observed. Last, the planet-radius distribution from Kepler observations show a deficit of planets with size similar to that of Saturn ($\sim$ 6-10 $R_\oplus$) that divides hot Neptunes from hot Jupiters, the so-called hot Saturn valley (Figure 2.16). This radius range roughly corresponds to the mass domain (between $\sim$ 10-30 and $\sim$ 100-200 $M_\oplus$) of the planet desert expected from core accretion of planet formation. However, these predictions apply to a = 0.2-0.3 AU while hot planets have $a < 0.1$ AU, so also migration mechanisms need to be taken into account. The similarities in

host metallicity, intrinsic frequency and preference for single transiting planetary systems suggest a close link between hot Jupiters and hot Neptunes in their migration and formation processes, suggesting that hot Neptunes may originate from photoevaporation of hot Jupiters.

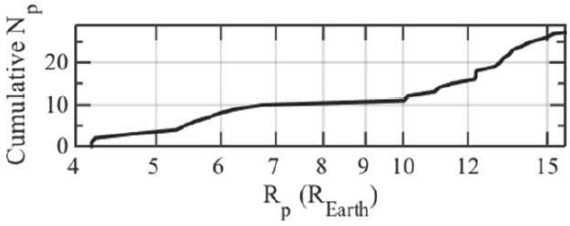

Figure 2.16: Cumulative distributions of planets with $R \geq 4\ R_{\oplus}$ from the Dong et al. [2018] sample, highlighting the presence of the hot Saturn valley.

2.2.3 Giant planets

Giant planets can be categorized into two different populations depending on their orbital separation from the host star:

- planets orbiting very close to the star, with $a \lesssim 0.1$ AU, or P = 3-9 d, are called hot Jupiters because of their high superficial temperatures due to their proximity to the star. Very hot Jupiters have been defined as gas giants with $P \leq 3$ d, or $a \leq 0.025$ AU. Last, ultra-short-period hot Jupiters are giants with $P < 1$ d, which occur only around stars of $M_{\star} \leq 1.25\, M_{\odot}$. A famous hot Jupiter is 51 Peg b (Mayor and Queloz [1995]).
- The second group is located at much larger separation, starting from ~ 0.4 AU up to several AU. This population is composed by temperate to cold giants, and includes planets like Jupiter.

Between these two clusters resides a region of transition where relatively few giant planets have been detected, known as the period valley (Figure 2.17 and Figure 1.1 for a more updated version). This valley in the period distribution of giant planets is a strong indicator that temperate/cold giants and hot Jupiters have different formations and migration mechanisms. In this valley are included also the so-called warm Jupiters, planets orbiting their host star at $a \sim 0.1$-1 AU with periods between 10 and 200 days.
It is generally held that in situ formation of hot Jupiters is unlikely: both the core accretion model and the disk instability model suggest that the region of formation of hot Jupiters is beyond the snow line of their protoplanetary disks ($a \gtrsim 3$ AU), where solid material is abundant because of the condensation of ices. Assuming formation at much larger distances from the host star, two main hypotheses have been proposed to explain how they reached their current

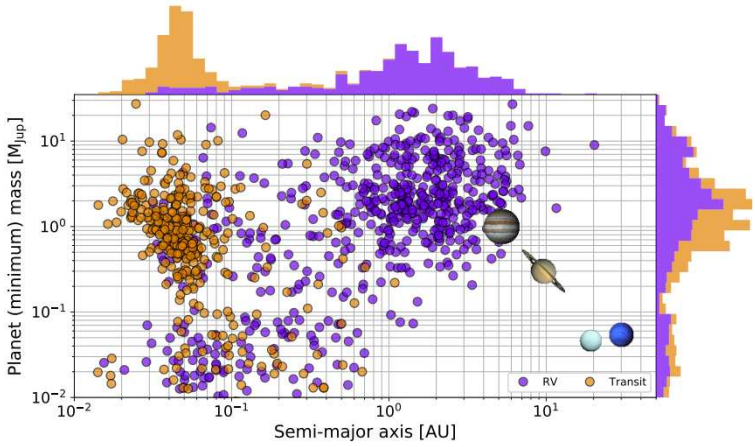

Figure 2.17: Exoplanets discovered as of May 2018 via the transit and radial velocity methods. Planetary mass is plotted as a function of semi-major axis, with histograms showing the distributions in semi-major axis (*top*) and minimum mass (*right*). The figure provides visual evidence of the so-called 'period valley' (Santerne [2018]).

location: inward, disk-driven migration, or placement on a highly eccentric orbit with a small pericenter, followed by tidal circularization. Spectroscopic surveys of hot Jupiters reveal that about half of them have long-period (several AU) massive companions, within the planetary or stellar regime (e.g. Neveu-VanMalle et al. [2016]). This supports the idea that hot Jupiters could have migrated through interaction with the disk or by planet-planet interaction. On the other hand, some temperate/cold giants and giants in the period valley have inner, low-mass planetary companions. This is evidence that these planets had a smooth disk migration that preserved the inner planets and, in some circumstances, the presence of the inner companion could even be the reason for these giant planets to stay cool and prevent them from migrating inwards and becoming hot Jupiters.
Data collected from the Kepler transit survey and two independent Doppler surveys (Cumming et al. [2008] referring to planets with $M > 0.3\,M_J$, Mayor et al. [2011] for planets with $M > 0.16\,M_J$) are well described by a distribution uniform in log-period from 2-300 days, followed by a sharp increase by a factor of 4-5 for longer periods. This behaviour might be related to the location of the snow line in protoplanetary disks: beyond this line there is enough material for giant planets to form, and thus to be more frequent. The occurrence rate of hot Jupiters in the solar neighbourhood has been estimated mainly by two radial velocity surveys: the Californian Planet Search (CPS) and the Geneva-lead survey. The CPS survey (Wright et al. [2012]) mostly used the Keck and Lick telescopes. They defined hot Jupiters as giant planets with $P < 10$ d and $M > 0.1\,M_J$, and they estimated an occurrence rate in their sample (836

stars observed at least for five epochs) of $1.2 \pm 0.38\,\%$. They also explored the period valley to search for temperate and cold giant populations and they found six planets with $M > 30\,M_\oplus$ and $P < 50$ d in a sample of 122 FGK dwarfs, leading to an occurrence rate of $4.9 \pm 2.0\,\%$ (Howard et al. [2010]). The Geneva survey (Mayor et al. [2011]) used both the CORALIE and HARPS spectrographs, with a sample composed by 822 southern stars up to 50 pc focusing on low-activity FGK dwarfs. They considered giant planets the ones with $M > 50\,M_\oplus$, and their found occurrence rate for giant planets with $P <$ 10 years is $13.9 \pm 1.7\,\%$. Selecting only hot Jupiters, period-valley giants and temperate giants ($P < 400$ d), it gives occurrence rates of $0.83 \pm 0.34\,\%$, $1.64 \pm 0.55\,\%$ and $2.90 \pm 0.72\,\%$, respectively (Santerne et al. [2016]). A survey based on the CoRoT space mission derived an occurrence of hot Jupiters of $0.95 \pm 0.26\,\%$ and $1.12 \pm 0.31\,\%$ (Deleuil et al. [2018]) for pointings toward the galactic center and anti-center, respectively. This values are in agreement with the value observed in the solar neighbourhood. In the Kepler field the occurrence rate of hot Jupiters, period-valley and temperate giant populations, cleaned from false positives, are $0.47 \pm 0.08\,\%$, $0.90 \pm 0.24\,\%$ and $3.19 \pm 0.73\,\%$, respectively (Fressin et al. [2013]). Notably, the hot Jupiter frequency is about half the one reported in the solar neighbourhood., as shown in Figure 2.18. This difference in the rates is unlikely explained by the difference of metallicity of the stellar field, since the Kepler field and the solar neighbourhood are comparable in metallicity. Several other explanations for this discrepancy are proposed, such as different stellar multiplicity rate or some bias in the stellar population observed by Kepler, but it remains unclear today.

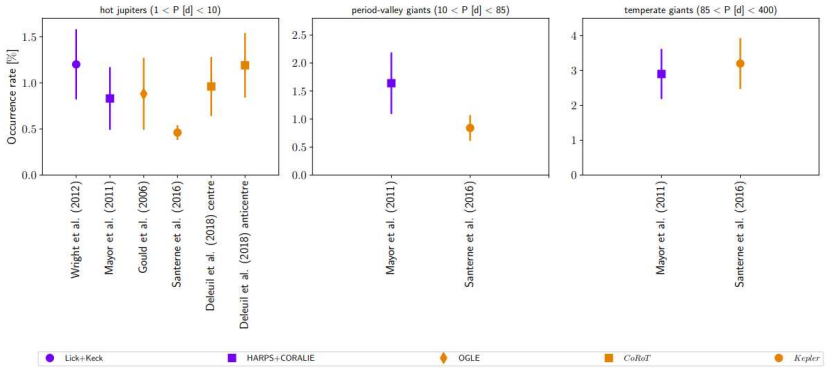

Figure 2.18: Occurrence rate of the different populations of extrasolar giant planets by different surveys. Adapted from Santerne et al. [2016].

A strong correlation between the stellar metallicity and the presence of giant planets is identified, with giant planets found to orbit preferentially metal-rich stars. Although this may seem to be an observational evidence for the core-accretion mechanism as the primary formation scenario for giant planets, the latest models of the disk instability mechanism (e.g. Nayakshin [2016]) are able

to reproduce this correlation. The correlation with metallicity can be modeled as a power law of the form:

$$\mathcal{P} = \alpha[Fe/H]^{\beta} \,, \tag{2.2.4}$$

with $\alpha = 0.03$ and $\beta = 2.0$, where $\mathcal{P}$ is the probability to find a giant planet orbiting a particular star (Fischer and Valenti [2005]). Detailed Bayesian analysis have been performed in order to constrain the form of the correlation in the low-metallicity regime (Mortier et al. [2013]), but an unique formulation is stil missing, and several hypotheses are studied. The metallicity of the host star does not only impact the presence of planets, it also shapes their period distribution. In fact, giant planets in metal poor systems are found at much larger separations than those in the metal-rich counterpart. In Figure 2.19 is indeed shown that giant planets orbiting stars with $[Fe/H] < 0.1$ *dex* have much longer orbital periods than those orbiting star more rich in metals. This is explained by the fact that giant planets still form around metal-poor stars. but slower than in metal-rich systems. As a consequence, their migration is also less efficient and they are observed close to their formation place. A discussion on the frequency of giant planets around metal-poor stars is presented in Barbato et al. [2019]. From a sample of 42 metal-poor stars (-1.0 *dex* $\leq [Fe/H] \leq -0.5$ *dex*) observed with HARPS-N, combined with a 88-star sample observed with HARPS in previous studies (e.g. Santos et al. [2011]), to form a unified sample of 130 metal-poor stars in both the northern and southern hemispheres, they obtained a total of five detected giant planets and one candidate. The obtained frequency is thus $f_p = 3.84^{+2.45}_{-1.06}$ % considering only the five detected planets, and $f_p = 4.61^{+2.58}_{-1.21}$ % including also the candidate. The detected planets all lie at the metal-rich end of the joint sample, ranging from [Fe/H] approximately -0.7 to -0.4 dex, confirming previous results that suggested that the frequency of giant planets continues to be a rising function of stellar metallicity even for metal-poor stars.

The mass of the central star impacts the formation of giant planets: the mass of the protoplanetary disk scales indeed with the mass of the star. Hence, more massive disks have the potential to form more efficiently massive planets, compared to low-mass disks. In fact, extremely few giant planets have been found so far to orbit low-mass M dwarfs (among the few cases, Kepler-42 b; Muirhead et al. [2012]). Therefore, protoplanetary disks surrounding M dwarfs are not massive enough to form efficiently giant planets. On the other end, massive stars form with massive disks and should form efficiently giant planets. It is also expected that a cut-off high mass exists, around which giant planets do not form. A possible explanation is because, at these high masses, the star evolves too fast off of the main sequence, or because of intense stellar winds.

2.2.4 Between planets and stars: Brown Dwarfs

Brown dwarfs are substellar objects with relatively low temperatures and luminosities compared to stars. Their masses are insufficient to sustain stable

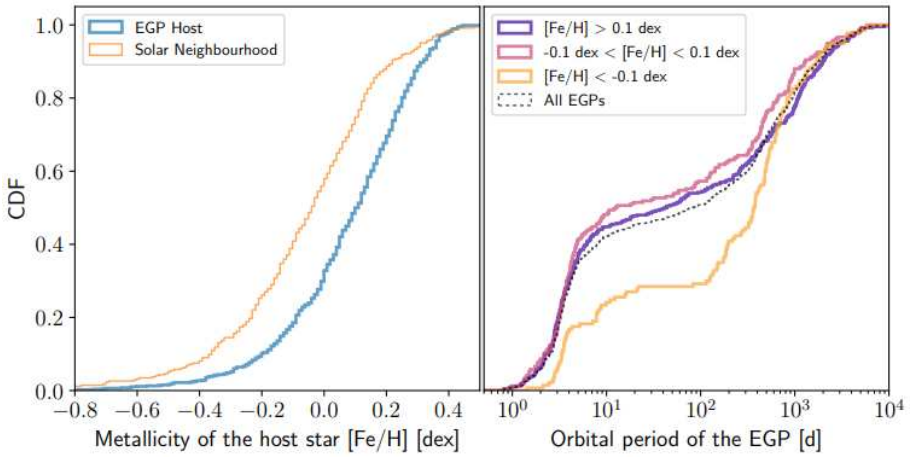

Figure 2.19: *Left*: cumulative distribution function (CDF) of the metallicity of extrasolar giant planets (EGP) host stars and of the solar neighborhood. *Right*: CDF of the orbital period of EGPs for three populations of host stars (Santerne [2018]).

hydrogen fusion, but they can still undergo lower-threshold nuclear reactions, such as deuterium burning. Spanning the mass range $\sim$ 13-80 M_J, their properties overlap with lower-mass stars and higher-mass planets in many aspects: their atmospheric properties and associated models, as an example, overlap with those of the highly irradiated hot Jupiters. At solar metallicity, objects above $\sim$ 78 M_J reach the core temperatures necessary to initiate H fusion, and become stars, while below $\sim$ 74 M_J this is not the case and these objects are called brown dwarfs. Transition objects in the range $\sim$ 74-78 M_J sustain core fusion for the first $\sim$ 10^9-10^{10} yr of their lifetime before falling temperatures transforms them in brown dwarfs. Decreasing metallicity leads to an increase in the mass of the stellar/substellar boundary: at zero metallicity, for example, this boundary is at $M \sim 0.09\ M_\odot = 96\ M_J$. Below the H burning limit, lower threshold nuclear reactions may still occur: for solar metallicity, Li fusion above 63-65 M_J and deuterium fusion above $\sim 13\,M_J$. Below the deuterium burning limit, which is sensitive to chemical composition, objects can not sustain any species of nuclear burning in their interiors. The typical deuterium fusion threshold of $\sim$ 13 M_J thus usually sets a lower mass limit for objects classified as brown dwarfs. Below that mass, there are planets.
Brown dwarfs are classified spectroscopically as L, T and Y. Atmospheric temperatures range from 2000-3000 K down to 500-600 K, so that their thermal emission lies primarily beyond 1 μm. The low temperature conditions accelerate condensation out of the gas state and into the formation of grains, such that the effects of condensates, clouds, molecular abundances and atomic opacities are important in interpreting spectral properties. Below 2000-2100 K, L dwarfs

are characterized by strong metal hybrid bands (FeH, CrH,...) and strong near-infrared absorption of H_2O and CO. Below 1200-1300 K, T dwarfs are characterised by prominent CH_4 absorption. Atmospheres are sufficiently cool for H_2O and CH_4 to form in abundance, resulting in planet-like spectra. Below 500-600 K, in Y dwarfs, NH_4 absorption makes a significant contribution to the near- and mid-infrared spectrum, along with scattering from water ice clouds. Several optical spectra of L and T-type brown dwarfs are shown in Figure 2.20.

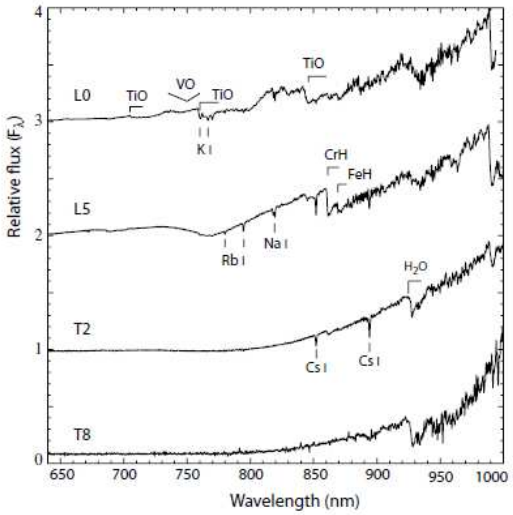

Figure 2.20: Optical spectra of L and T-type brown dwarfs, with T_{eff} ranging from $\sim$ 2100 K at L0 to $\sim$ 900 K at T8 (Reid and Metchev [2008]).

Several independent surveys have shown that the occurrence rate of brown dwarfs is low, especially in close orbits, giving origin to the term "brown dwarf desert" to indicate a range of orbits (up to 5 AU around solar-type stars) within which brown dwarfs are unlikely to be found orbiting a star. A survey exploring the brown dwarf desert (Unger et al. [2023]), combining radial velocity measurements collected from CORALIE with Gaia DR3 data obtained an occurrence rate for brown dwarf companions (13-80 M_J) on close orbits ($<$ 10 AU) of $0.8^{+0.3}_{-0.2}$ %.

The majority of brown dwarfs likely have protoplanetary disks, which can result in the formation of Earth-sized or smaller planets. The possibility to have habitable planets around brown dwarfs is determined by the properties of the brown dwarf: the inner and outer limits of the habitable zone, the prospects for photosynthesis on brown dwarfs and, last, the origin of life needs sufficient fluxes of UV-C radiation. A recent study (Lingam et al. [2020]) demonstrated that, if the habitable zone is assumed to lie in the temperature range 175-270

K, a planet can remain within it for a time:

$$t_{HZ} \approx 3 \cdot 10^{-7} \left(\frac{M_{BD}}{M_J} \right)^{2.037} \left(\frac{a}{1AU} \right)^{-1.543} Gyr \ . \tag{2.2.5}$$

The maximum lifetime occurs when the planet is situated close to its Roche limit and, for $t_{HZ} > 10$ Gyr to be valid at the Roche limit, it would require $M_{BD} \gtrsim 100\, M_J$, higher than the conventional upper bound for brown dwarfs. By setting $t_{HZ} \sim 1$ Gyr, the results shows that it is possible for $M_{BD} \gtrsim 20\, M_J$: hence, it is unlikely that brown dwarfs below this value can host planets that remain habitable over geologically significant timescales. Considering photosynthesis, in the same study is shown that, it is found that brown dwarfs with $M_{BD} < 30\, M_J$ are not able to emit enough photosynthetically active radiation over timescales of $\sim Gyr$, so planets around these brown dwarfs are not able to sustain photosynthetic biospheres over these timescales. Last, analyzing the emitted flux, the authors found that it is relatively unlikely for planets around brown dwarfs with masses $< 40\, M_J$ to support UV-mediated prebiotic reactions over a timespan $\gtrsim 100$ Myr. Even when these mass limits are exceeded, the prospects for long-term habitability are determined by the planet's orbital radius: planets that are too far out ($\gtrsim 0.1$ AU) do not receive sufficient fluxes of electromagnetic radiation in the appropriate range, while overly close-in planets ($\lesssim 10^{-3}$ AU) are susceptible to tidal heating and disruption. Another crucial point is that brown dwarfs have temporally limited habitable zones with respect to M-dwarfs, therefore it is not expected that brown dwarfs host habitable planets when their age exceeds ~ 10 Gyr. Recent statistical studies suggest that the number of brown dwarfs with $M_{BD} > 30\, M_J$ is potentially as high as $\sim 10^{11}$, but it is not possible to estimate the number of Earth-sized planets in the habitable zones of brown dwarfs due to the paucity of available statistics.

Chapter 3

Exoplanets detection techniques

Somewhere, something incredible is waiting to be known.
– Carl Sagan

The first exoplanet discovery around a main sequence star dates back to 1995, with the detection of a planet orbiting the Sun-like star 51 Pegasi (Mayor and Queloz [1995]). Since then, an increasing number of exoplanets around various types of stars have been detected, thanks to the continuous improvement of different detection techniques. These techniques are often complementary, as they are suited to identifying objects at different distances from their host star and across a range of masses. To achieve a more complete characterization of exoplanets, they are frequently combined in a multi-technique approach. This chapter describes the main planet detection methods, except for direct imaging, which will be discussed in greater detail in Chapter 4.

3.1 Radial velocities

The motion of a planet in orbit around a star causes the star to undergo a motion around the star-planet barycenter, with each body moving in a closed elliptical orbit. The mass of the star is much larger than the mass of the planet, so that the center of mass will almost coincide with the center of the star. However, this little displacement is sufficient to produce periodic variations in the radial velocity of the star, detectable from a small but systematic Doppler shift of the many absorption lines that make up the stellar spectrum. If, in the observer's reference frame, the source is receding with velocity v at an angle θ relative to the observer-source direction, the change in wavelength is related to the velocity by:

$$\lambda_{obs} = \lambda_{em} \frac{1 + \beta \cos\theta}{\sqrt{1 - \beta^2}} \ , \tag{3.1.1}$$

where λ_{obs}, λ_{em} are the observed and emitted wavelengths and $\beta = v/c$. For $v \ll c$ and $\theta \ll \pi/2$ this expression reduces to the classical form:

$$v_r = v\cos\theta \approx \left(\frac{\Delta\lambda}{\lambda_{em}}\right) c\,, \tag{3.1.2}$$

where $\Delta\lambda = \lambda_{obs} - \lambda_{em}$ and, conventionally, positive values indicate recession. From the radial velocity measurements of a star, it is possible to derive some physical parameters of the orbiting planets, such as their mass and orbital period. Consider a planet with mass M_p around a star of mass $M_\star$ describing an elliptical orbit of semi-major axis a and eccentricity e with a period P. The orbital radius varies between the pericenter distance $a(1-e)$ and the apocenter distance $a(1+e)$. Different angles, or anomalies, can be defined to describe this elliptical orbit. The true anomaly $f(t)$ is the angle between the direction of pericenter and the current position of the body measured from the barycentric focus of the ellipse. The eccentric anomaly $E(t)$ is an angle referred to the auxiliary circle of the ellipse, and it is related to the true anomaly by:

$$\tan\frac{f(t)}{2} = \sqrt{\frac{1+e}{1-e}}\,\tan\frac{E(t)}{2}\,. \tag{3.1.3}$$

The mean anomaly $M(t)$ is related to a fictitious mean motion around the orbit, and the mean anomaly at time $t - t_p$ after the pericenter passage is defined as:

$$M(t) = \frac{2\pi}{P}(t - t_p)\,. \tag{3.1.4}$$

The eccentric anomaly and the mean anomaly are related by the Kepler's equation:

$$M(t) = E(t) - e\sin E(t)\,. \tag{3.1.5}$$

The position of an object along its orbit at any time can then be obtained by calculating the mean anomaly at that time from equation (3.1.4), numerically solving equation (3.1.5) for E and last using the equation (3.1.3) to obtain f. Radial velocity measurements describe the projected motion, along the line of sight, of the star as it orbits the system barycenter. The radial velocity of the star can be expressed as:

$$v_r = K\left[\cos(\omega + f) + e\cos\omega\right]\,, \tag{3.1.6}$$

where ω specifies the argument of pericenter, the angular coordinate of the object's pericenter relative to its ascending node, measured in the orbital plane and in the direction of motion. K is the radial velocity semi-amplitude, given by:

$$K = \left(\frac{2\pi G}{P}\right)^{1/3} \frac{M_p\sin i}{(M_\star + M_p)^{2/3}} \frac{1}{\sqrt{1-e^2}} \tag{3.1.7}$$

where i specifies the orbit inclination with respect to the reference plane, with $i = 0°$ indicating a face-on orbit.

If $M_\star$ can be estimated independently, then $M_p \sin i$ can be determined. Without additional information on the inclination, the planetary mass cannot be obtained, and small values of K, for example, could indicate either a low-mass planet viewed with high inclination or an object of significantly higher mass with small orbital inclination. $M \sin i$ is usually called the minimum mass of the planet. To give an idea of the magnitude of radial velocity variations due to the presence of planets, consider the Solar System. For Jupiter $K_J \approx 12.5\ m/s$, while for Earth $K_\oplus \approx 0.09\ m/s$. Figure 3.1 shows the radial velocity curve of the star 51 Peg, which led to the discovery of 51 Peg b in 1995.

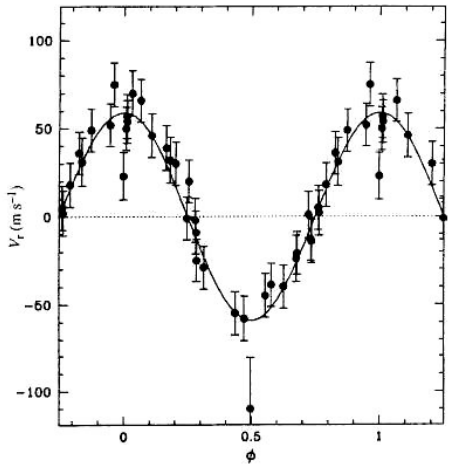

Figure 3.1: Radial velocity curve of the star 51 Peg, phased to a period of 4.23 days, obtained with the ELODIE spectrograph (Mayor and Queloz [1995]).

Massive planets orbiting closer to their host star are optimal targets for radial velocity measurements, since the semi-amplitude of their signal, which is an observable that can be measured, is larger. Highly eccentric orbits are harder to detect at short periods, where poor sampling can result in poor phase coverage during rapid pericenter passages. Moreover, the shape of the radial velocity curve is strongly dependent on the orbital eccentricity, increasingly departing from a sinusoid with increasing eccentricity. For example, Figure 3.2 shows the radial velocity curve for the star HD 66428, hosting a planet with $M \sin i = 2.96\ M_J$ and on an eccentric orbit, with $e = 0.5$.
The detection of planets has demanded long-term radial velocity accuracies of the order of m/s, corresponding to an accuracy of a few parts in 10^8 in wavelength, maintained over months or years. To collect high-accuracy radial velocities, échelle spectrographs with high spectral resolving power are typically used. High instrumental stability and accurate wavelength calibration is demanded to improve the precision, and large telescopes and long integration times are necessary to achieve an elevate signal-to-noise ratio. For any absolute determination of radial velocities at the m/s level, many effects have to be considered, in-

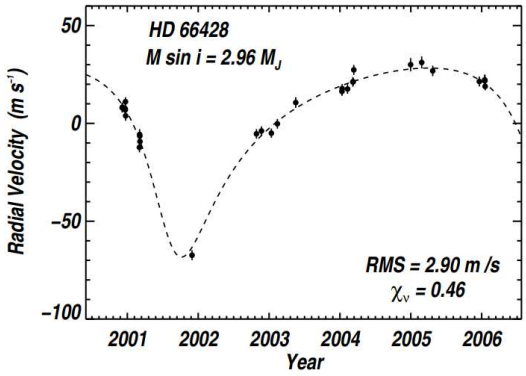

Figure 3.2: Radial velocity curve of the star HD 66428, unveiling the presence of a planet with $M \sin i = 2.96\ M_J$ and $e = 0.5$ (R. P. Butler and others [2006]).

cluding: barycentric correction, Earth rotation, stellar rotation, stellar activity and many more. Various effects, other than an orbiting exoplanet, can produce periodic variations in stellar radial velocity. The amplitude of these variations provides an estimate of the mass of the perturbing object. If the variations are on the order of km/s, the perturber is likely of stellar nature. Additionally, intrinsic stellar phenomena, such as activity and oscillations, can induce periodic radial velocity variations even in the absence of a planet. To determine whether the observed variations are caused by an orbiting companion, an effective approach is to analyze the shape of spectral lines, particularly the line bisector. True Doppler shifts, caused by orbital motion, preserve the shape of spectral lines. In contrast, correlations between measured radial velocity variations and changes in line width indicate that the signal may originate from stellar activity rather than the presence of a companion. The preferred targets of radial velocity surveys are bright stars, because a large number of photons is needed to make a precise Doppler measurement. The targeted stars should have narrow lines, and hot, rapidly rotating stars are also unsuitable. For these motivations, radial velocity surveys usually target stars of spectral type later than F6.
The first exoplanet discovered using the radial velocity technique, and the first exoplanet ever detected around a solar-type star, was 51 Peg b (Mayor and Queloz [1995]), a giant planet orbiting its host star in approximately 4.2 days, and its discovery challenged the prevailing planet formation models of the time. However, the theoretical concept of detecting planets via radial velocity had been proposed decades earlier. An early example is Struve [1952], where the author explores the radial velocity amplitudes induced by different types of planets on their host stars and discusses the feasibility of detecting them with the instruments available at the time. This method is one of the most successful in detecting exoplanets with masses down to that of Earth. However, most of the discovered planets are located close to their host stars, as larger orbital sepa-

rations require longer observation times. Additionally, the method struggles to detect smaller planets, since Mercury-like bodies induce radial velocity variations that are too small to be measured with current instruments. In conclusion, radial velocities measurements allow us to characterize part of the inner region of exoplanetary systems, but fail to detect farther planets.

3.2 Transits

Given a suitable alignment geometry, the light from the host star is attenuated by the transit of a planet across its disk, with the effect repeating at each orbital period. The probability of observing a transit for any given star, seen from a random direction and at a random time, is extremely small: in fact, transits only occur if $i \approx 90°$. More in detail, the minimum inclination where transits can occur is given by $\cos i_{min} = R_\star/a$. The light curve of a star with a transiting planet presents a decrease of the observed flux during the transit. After the transit, the brighter day side of the planet progressively comes into view, and the total flux rises, to drop again during the secondary eclipse as the planet passes behind the star. The schematic of a transit is shown in Figure 3.3.

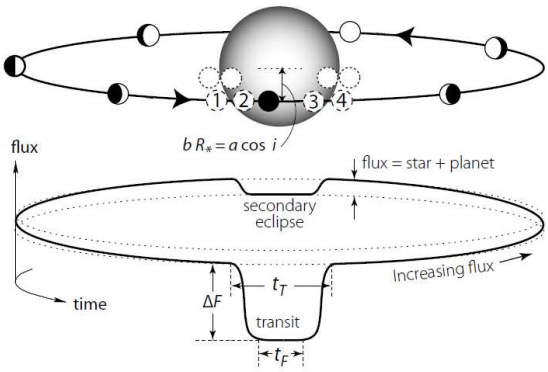

Figure 3.3: Photometric transit geometry (Winn [2010]).

The amplitude of the transit signal and the transit probability are independent on the star distance, but the corresponding photometric accuracy decreases. If a planet of radius R_p transits in front of a star with radius $R_\star$, the transit depth is then:

$$\Delta F = \left(\frac{R_p}{R_\star}\right)^2 \tag{3.2.1}$$

and the effect is generally very small. For example, a planet with $R \sim R_J$ transiting a Sun-like star results in $\Delta F/F \approx 1.1 \cdot 10^{-2}$, while for an Earth-like planet we get $\Delta F/F \approx 8.4 \cdot 10^{-5}$. If $R_\star$ can be estimated independently, the planetary radius R_p can be estimated from equation (3.2.1).

The probability to observe a transit, for the general case of an eccentric orbit, can be expressed as:

$$p = \frac{(R_\star \pm R_p)(1 + e\sin\omega)}{a(1-e^2)} \,, \tag{3.2.2}$$

where the term $\pm R_p$ accounts for the inclusion or exclusion of grazing transits (when the figures of the planet and the star do not overlap completely). In the simple case of a circular orbit and assuming $R_p \ll R_\star$ this reduces to:

$$p \approx \frac{R_\star}{a} \approx 0.005 \frac{R_\star}{R_\odot} \frac{1AU}{a} \tag{3.2.3}$$

(Borucki and Summers [1984]) and this shows that planets on eccentric orbits are more likely to transit than those on circular orbits with the same semi-major axis, by a factor $(1-e^2)^{-1}$. From equation (3.2.2), we notice that planets orbiting close to a host star with large radii are more probable to be observed transiting. The probability to observe a planet transiting at 1 AU from its host star is $\sim 0.5\%$, but grows up to $\sim 10\%$ at 0.05 AU: hot planets are thus more likely to be detected.

From the analysis of a transit light-curve, many physical parameters like the stellar density, the planet surface gravity and the orbital inclination can be derived. If, for a given planet, both radial velocity and transit observations are available, its density can be derived from the mass and radius estimations, giving a first insight on its composition. The photometric precision of ground-based observations is limited by atmospheric fluctuations, currently able to discover exoplanet transits with depths up to $\sim 1\%$, thus limited to giant planets. In order to detect terrestrial planets observations from space are necessary: many space-based surveys like Kepler (Borucki et al. [1997]) and TESS (Transiting Exoplanet Survey Satellite; Ricker et al. [2015]) discovered thousands of planets, and future missions like PLATO (PLAnetary Transits and Oscillations of stars; Rauer et al. [2025]) are specifically designed to search for Earth-like planets. A real light-curve, from JWST (James Webb Space Telescope; Gardner et al. [2006]), is shown in Figure 3.4.

Another source of error is that due to photon statistics on the mid-transit time, given by:

$$\frac{\sigma_{t_c}}{t_T} \sim (St_T)^{-1/2} \frac{R_p}{R_\star} \,, \tag{3.2.4}$$

(Holman and Murray [2005]), where t_T is the transit duration and S the stellar photon count rate. The resulting accuracies on the ephemeris periods can be as high as 0.01 s or better, and ephemerides errors have an impact on the efficiency of follow-up observations. It is thus fundamental to achieve a very high precision in the mid-transit time estimation.

A transit-type signature in a star light-curve is not always caused by a transiting planet, since multiple phenomena can mimic this effect, like for example a grazing eclipse by a main sequence star or an eclipsing binary in the background. For these reasons follow-up observations, like spectroscopic measurements, are required to remove false positives and confirm the planetary nature of a list of

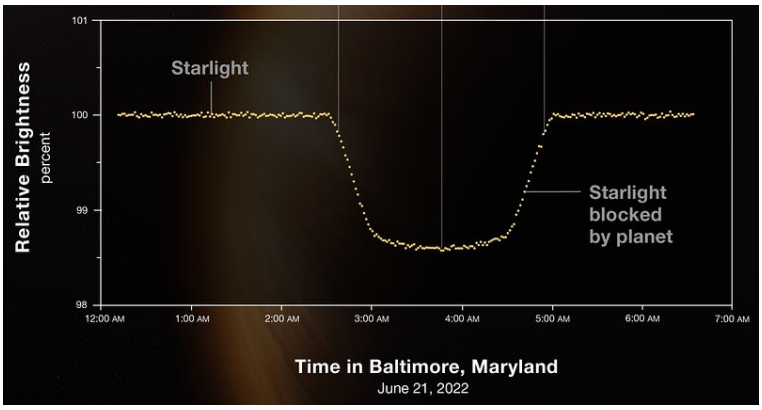

Figure 3.4: Light-curve from JWST's NIRISS (Near InfraRed Imager and Slitless Spectrograph) showing the change in brightness of light from the star WASP-96 over time as a planet transits the star. Credits: NASA (https://webbtelescope.org/contents/media/images/2022/032/01G72W1XZK6A79RJK2Z93D58CD).

candidates provided by a transit survey. The first exoplanet observed transiting its host star was HD 209458 b (Charbonneau et al. [2000]), a giant planet orbiting its host star in approximately 3.5 days. Since then, this technique has led to the detection of a vast number of exoplanets, establishing itself as one of the most successful methods to date. Transits are particularly useful in searching objects close to their host star, helping to characterize the inner part of exoplanetary systems.

3.2.1 Transit Timing Variations

Transits of a single planet on a Keplerian orbit occur at regular times given by the orbital period. With a further body in the system, the orbit is no longer Keplerian and the transits are no longer strictly periodic, because of the gravitational perturbation of the additional body on the transiting one. Transit timing variations (TTVs) describe the deviations from the linear ephemeris of a strictly Keplerian orbit, and the amplitude of this effect is dependent on the mass of the perturber, being strongly enhanced if it is locked in a low-order orbital resonance with the transiting planet. For example, a Jupiter-mass planet in a $2:1$ resonance would cause a variation of many minutes, which is in principle easy to detect. In case of a Keplerian motion, the timing of the transit can be calculated as:

$$C = T_0 + P \cdot E \,, \tag{3.2.5}$$

where E is the epoch (an integer transit number), T_0 is the time of the transit at $E = 0$, P is the orbital period and C stands for "calculated" based on a constant-period model. Meanwhile, the observed transit times are denoted

O. TTVs are typically represented using the O–C diagram (observed minus calculated), where deviations from a linear ephemeris are plotted to highlight timing variations. The O - C diagram for WASP-47 is shown in Figure 3.5.

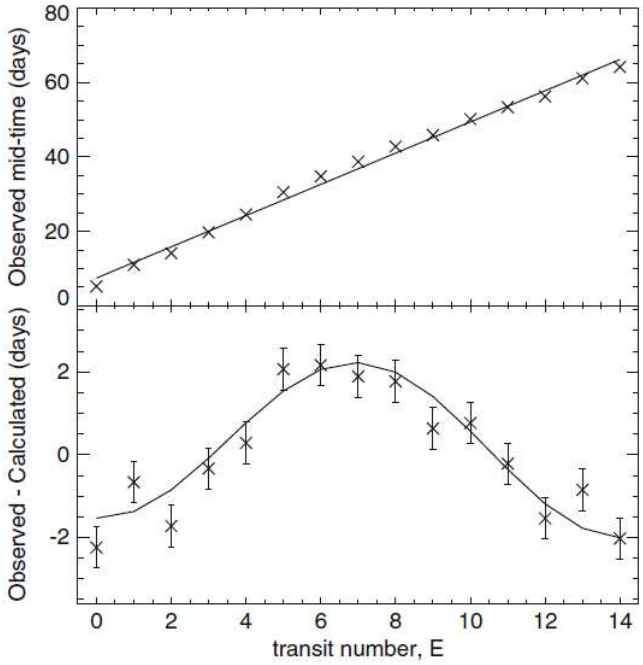

Figure 3.5: O-C diagram for WASP-47. *Top panel*: measured transit midtimes, the line is a fit by least squares. *Bottom panel*: residuals of the fit, observed minus calculated, the line represents the theoretical model (Agol and Fabrycky [2017]).

The task of inverting a set of transit times to recover the masses and the orbits of the constituent planets is difficult, in part due to its computational expense, but also because different perturber mass-orbit configurations can lead to degenerate solutions. This degeneracy can be partially broken with a numerical N-body integration or, if the measurements of the transit times have high precision, an analytical model based on perturbation theory can be used. Transits may also change in duration over time. Such transit duration variations (TDVs) can be caused by changes in a, e or ω. The most prominent effect is due to orbital plane reorientation: changes in the inclination will change the length of the transit chord, which in turn changes the duration of the transit. The TDV amplitude is proportional to the perturber mass, does not require orbital resonances and can reach some tens of seconds for Earth-sized perturbers.
The theoretical concept of detecting planets through TTVs was first proposed by Agol et al. [2005], where TTVs were analytically computed for a range of

theoretical scenarios and known multiplanet systems. The study also explored the feasibility of detecting planets via TTVs using the available instrumentation at the time. The first confirmed detection of planets using this method was reported in Steffen et al. [2013], which identified 27 planets in 13 planetary systems initially discovered by Kepler. The confirmation was based on the presence of anticorrelated transit timing variations, demonstrating that the candidates belong to the same system, and on long-term dynamical stability analyses, which constrained their masses, confirming their planetary nature. Since then, numerous planets have been discovered using TTVs, both from ground-based and space-based observations. Notably, the Kepler mission has provided the first exomoon candidates (see Kipping [2020] for a more detailed analysis). While no exomoon has been conclusively identified to date, TTVs and TDVs remain among the most promising techniques for their potential detection.

3.3 Astrometry

Astrometry consists in measuring the positions and the motions of the astronomical objects on the sky. Two different measurement approaches can be applied. The first involves making differential measurements by tracking an object's position relative to other objects (relative astrometry). A key example is the motion of a planet around its host star, which can be observed and measured using direct imaging techniques. The second approach involves observing from two widely separated viewing directions (absolute astrometry). By scanning the entire celestial sphere, this method allows the creation of an all-sky catalog of stellar positions, proper motions, and parallaxes.

As with the radial velocity technique, the astrometry method also exploits the fact that when one or more planets orbit a star, the star itself moves around the system's center of mass. This motion is a linear combination of the reflex motions induced by each planetary orbit, with an amplitude proportional to the planetary masses. Because planets are typically too faint to be observed directly, monitoring the motion of the host star allows for the indirect detection of orbiting planets and the determination of their characteristics. The motion of a star projected onto the plane of sky is the combination of three types of apparent motion: parallax, the proper motion and the reflex motion due to the presence of planets (Figure 3.6). A precise orbit determination can therefore show the presence of planets only if the effect of parallax and proper motion can be subtracted.

Astrometric measurements of the motion of a star of mass $M_\star$ located at a distance d due to the presence of a planet yield the period P and the planetary mass M_p, but also the six parameters of the orbit a, e, T_0, i, ω and Ω. For multiple planet systems astrometry can also, in principle, determine the relative inclination between pairs of orbits. The contribution of a planet to the reflex motion of its host star is given by the following formula of the apparent semi-

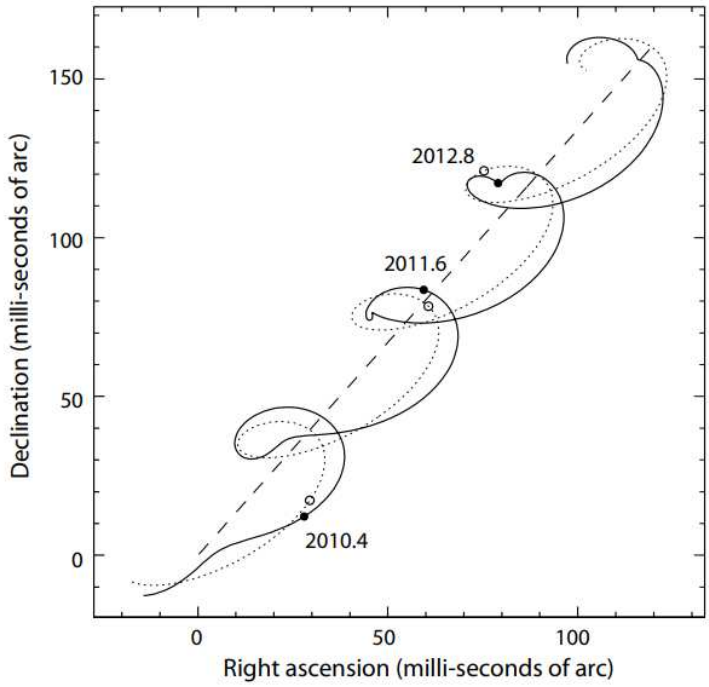

Figure 3.6: This figure shows how the angular position of a star on the celestial sphere is perceived to change with time. A typical star moves through space at a velocity $\sim 10 - 30\ km/s$, tracing out a linear path across the sky (dashed line). Superimposed on this, the star's position appears to oscillate due to the Earth's motion around the Sun, allowing to measure the star's distance through the parallax effect (dotted line). A planet orbiting the star describes a more complex motion around the center of mass of the system (solid line) (Perryman [2012]).

major axis of the stellar orbit (Malbet and Sozzetti [2018]):

$$\Delta\alpha = 0.33\ \frac{a}{1\ AU}\ \frac{M_p}{M_\oplus}\ \frac{M_\odot}{M_\star}\ \frac{10\ pc}{d}\ \mu as\ . \tag{3.3.1}$$

It follows that astrometry is particularly effective for detecting nearby systems and is most sensitive to massive planets with large semi-major axes. The effect is very small, and typically the accuracy required to detect planets is sub-mas. More in detail, a Jupiter in a solar-like planetary system located at 10 pc gives a signal of the order of 500 μas, and an Earth-like planet in its habitable zone only of 0.3 μas. At this precision level, several secondary effects must be taken into account: refraction of the light in Earth atmosphere, gravitational light deflection by massive objects in the line of sight and many others. Expected

astrometric signals for different types of planetary systems are presented in Table 3.1.

	Classical Jupiter	Young Jupiter	Hot Jupiter	Hot super-Earth	Earth in HZ	Earth in HZ
Stellar spectral type	G2	G2	G2	M	G2	M
M_P ($M_\oplus$)	300	300	300	5	1	1
a_P (AU)	5	5	0.1	0.1	1	0.28
P (yr)	11	11	0.03	0.05	1	0.2
$M_\star$ ($M_\odot$)	1	1	1	0.45	1	0.45
d (pc)	10	150	10	2.5	10	10
Astrometric signal (μas)	**495**	**33**	**10**	**1**	**0.3**	**0.2**

Table 3.1: Astrometric signals for different types of planets (HZ: habitable zone).

Astrometric surveys can be conducted both from the ground and from space. However, achieving the precision required for effective planet detection generally requires space-based observations. Ground-based observations are mostly used to perform follow-ups on objects that have already been detected with other techniques. The space mission Gaia (Gaia Collaboration et al. [2016]) has an accuracy in the astrometric measurements that can reach $\sim 10\ \mu as$ between $V \sim 7-12$, degrading according to photon statistics, and the number of astrometric exoplanet discoveries with Gaia is expected to be of order of several thousands, monitoring stars distant up to $\sim 200\ pc$. The details related to new discoveries will be more clear in the next years, with the release of Gaia astrometry data. The latest release, Gaia Data Release 3 (Gaia Collaboration et al. [2023]), dates back to June 2023. An important parameter, related to Gaia observations, is the renormalized unit weight error (RUWE; Lindegren et al. [2021]), defined as:

$$RUWE = \frac{\sqrt{\chi^2/(N-5)}}{u_0(G,C)}\ , \tag{3.3.2}$$

where χ^2 is the astrometric chi-squared following a chi-square distribution with $\nu = N - 5$ degrees of freedom, with N the number of observations (excluding the outliers). Last, u_0 is a normalizing reference function, which depends on the magnitude G and on the color index C. This parameter, typically used as a statistical quality flag for Gaia data, also serves as a useful diagnostic for the presence of close companions. A high RUWE value is often indicative of a nearby massive object, whose gravitational influence perturbs the motion of the target star, increasing the uncertainty in its astrometric solution and thus inflating the RUWE. A commonly adopted threshold is 1.4, above which the astrometric solution may be unreliable. Figure 3.7 shows the estimated astrometric signature for the known exoplanets up to February 2018

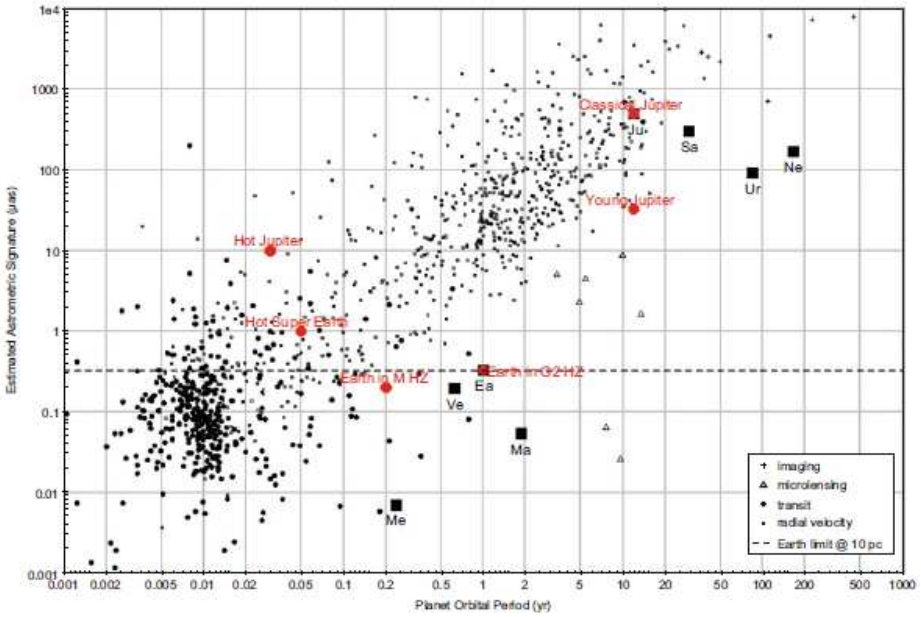

Figure 3.7: Estimated astrometric signatures for all 1160 confirmed exoplanets as known in February 15, 2018 in function of their orbital period. The signals generated by the planets of a Solar System located at 10 pc are also shown (Malbet and Sozzetti [2018]).

Thanks to the precise proper motion measurements of hundreds of thousands of stars provided by instruments such as Hipparcos (Perryman et al. [1997]) and, more recently, Gaia, the detection of an increasing number of companions from their influence on the proper motion (PM) has become possible. In fact, for an isolated single star with no intrinsic morphological change, the motion of its photocenter is linear and uniform, and the PM vector is therefore constant in direction and norm. In presence of a secondary mass, the barycenter will be shifted away from the primary star and, due to the photometric contribution of the secondary, the photocenter of the system will also be displaced. Therefore, the PM vector of the photocenter of a binary system will vary with time. A proper motion anomaly (PMa) measurement is based on the comparison of proper motion values reported in different catalogs at different epochs, in order to compute the deviation of a star's motion from a purely linear trajectory. First, the long-term proper motion vector is estimated from the proper motions measured at two different epochs. The PMa at each epoch is then defined as the difference between the long-term proper motion and the catalog-specific proper motion measured at that epoch. As an example, the method employed by Kervella et al. [2019], which was later updated in a second version (Kervella et al. [2022]), is described here. This work computed the PMa for more than

10^5 stars by comparing the proper motions listed in the Hipparcos and Gaia EDR3 catalogs. The PMa vector $\Delta\boldsymbol{\mu}_{H/G3}$ can be here defined as the result of the subtraction of the long-term PM vector $\boldsymbol{\mu}_{HG}$ from the PM vectors of the two catalogs (Hipparcos and Gaia EDR3):

$$\Delta\boldsymbol{\mu}_{H/G3} = \boldsymbol{\mu}_{H/G3} - \boldsymbol{\mu}_{HG} \ , \tag{3.3.3}$$

with $\boldsymbol{\mu}_{H/G3}$ the PM vectors from the Hipparcos or GDR3 catalogs and $\boldsymbol{\mu}_{HG}$ the mean PM vector determined from the difference in astrometric position (α, δ, π) between the two catalogs, expressed at the corresponding comparison epoch.

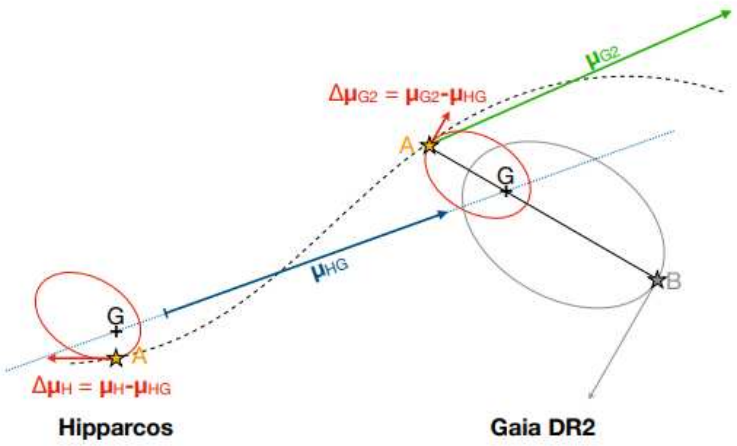

Figure 3.8: Principle of the proper motion anomaly determination (Kervella et al. [2019]).

The PM vectors contain the sum of the barycenter velocity and the "virtual orbital" velocity of the photocenter, the differential PMa vector $\Delta\boldsymbol{\mu}$ thus corresponds to the projected velocity vector of the photocenter around the barycenter at the Hipparcos or GDR3 epochs. The mass of the companion of a primary star exhibiting a PMa can be constrained using the measured tangential velocity anomaly. It is, however, degenerate with its orbital radius r following the relation:

$$\frac{m_2}{\sqrt{r}} = \sqrt{\frac{m_1}{G}} v_1 = 4740.470 \cdot \frac{\Delta\mu}{\pi} \sqrt{\frac{m_1}{G}}, \tag{3.3.4}$$

where m_1 is the mass of the primary star, m_2 the mass of the companion, $\Delta\mu$ the PMa, v_1 the tangential orbital velocity of the primary star, π the parallax and the multiplicative term transforms the ratio between $\Delta\mu$ and π in m/s. In this expression, it is assumed that $m_2 \ll m_1$ and that the orbital plane is perpendicular to the line of sight. The sensitivity of the PMa technique therefore decreases linearly with the distance of the target, and it is also limited by the time window smearing of the short-term PM measurements as well as the limited

time baseline between the Hipparcos and Gaia epochs for the estimation of the long-term PM vector. Further corrections, accounting for the effects of orbital inclination and for the excess noise, among others, are apported to increase the accuracy of the results. A PMa detection for a star is conventionally considered significant, and thus indicative of the presence of a companion, when the Signal-to-Noise ratio of the measurement exceeds 3.
Historically, this principle was first employed by Bessel [1844] to discover the invisible companion of Sirius, the white dwarf Sirius B, and it was also applied to various types of stars, for instance by Wielen et al. [1999] and Makarov et al. [2008].

3.4 Microlensing

In general relativity, the presence of matter distorts spacetime, and the path of electromagnetic radiation is deflected as a result. Under certain conditions, light rays from a distant background object (the source) are bent by the gravitational potential of a foreground object (the lens) to create images of the source which are distorted and which may be significantly amplified. The occurrence of this event depends upon the fortuitous alignment of the background source, the lens and the observer. This effect is called gravitational lensing. In the microlensing regime, both source and lens are objects in the stellar regime (or below) and the angular distances between the images generated by the lensing effect are of order 1 mas, meaning no current telescope can resolve the images.

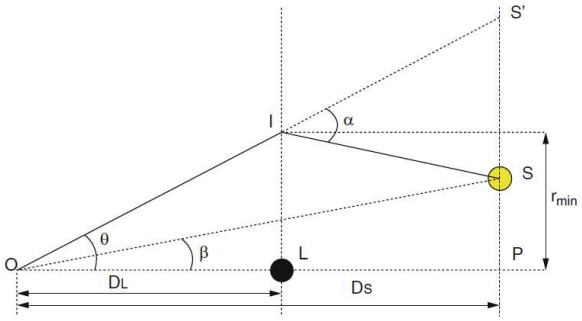

Figure 3.9: Deviation of a light ray from a source S due to the gravitational field of a lens L (Batista [2018]).

Consider a light ray coming from the source S being deflected by a point mass L, called lens (Figure 3.9). The light is deviated by an angle α, creating the illusion for the observer that the source is at the position S'. Under the assumption of small angles, the three angles α, β and θ are related by:

$$\alpha(D_S - D_L) = D_S(\theta - \beta) \ , \tag{3.4.1}$$

where $\alpha = 4GM/(D_L\theta c^2)$, with M the lens mass, D_S is the distance between the observer and the source and D_L the distance between the observer and the lens. The deviation of light affects an ensemble of rays coming from the source, so when the lens and the source are perfectly aligned on the observer's line of sight ($\beta = 0$) the source image in the lens plan appears like a ring, called the Einstein ring, whose angular size is expressed as:

$$\theta_E = \sqrt{\frac{4GM}{c^2}\frac{D_S - D_L}{D_S D_L}} \, . \tag{3.4.2}$$

For a source at the distance of the Galactic center ($\sim$ 8 kpc) and a lens with solar mass half way, typical images separations are of order $\theta_E \sim 1$ mas, well below the angular resolution of most ground-based instruments. For the vast majority of events, the source and the lens are never perfectly aligned, and a complete Einstein ring never forms.

A microlensing effect is visible on the light curve of the source star as a magnification of its light, up to tens or hundreds of times of its luminosity. The magnification of the source by the lens is estimated as the area ratio of the images (the major and minor images, outside and inside of the Einstein ring, respectively) over the source. The lensing effects caused by exoplanets are short-lived, because of the very low mass ratio of the planet to its host star, and the presence of an exoplanet manifests in the form of an anomaly, like a single additional bump, on a typical single-lens microlensing light curve caused by its host star. The first planet detected through gravitational microlensing was OGLE-2003-BLG-235, reported in Bond et al. [2004]. This event, observed in both the MOA (Microlensing Observations in Astrophysics; Bond et al. [2001]) and OGLE (Optical Gravitational Lensing Experiment; Udalski et al. [2015]) survey observations, was originated by a planet of about 1.5 M_J with an orbital radius of $\sim$ 3 AU, assuming that the host star is a main sequence star. Figure 3.10 shows the light-curve of the microlensing event OGLE-11-0265, as an example of planetary microlensing. Modeling the light curves of planetary microlensing usually provides two well-determined parameters: the mass ratio q between the star and the planet and the projected separation of components in the sky in the units of the Einstein ring. By taking into account and modeling the effects related to the finite size of the source, θ_E can be derived and, measuring also the lens-source parallax, the lens mass can be directly determined. Also free-floating planets can be detected with microlensing if they give rise to isolated, short term events.

Because of the peculiar geometrical configuration needed to detect a microlensing signal, millions of stars need to be monitored in order to observe a handful of magnified ones: up to October 2024 317 planets have been discovered using the microlensing technique. A wide range of masses (down to $M_\oplus$ and even smaller) can be detected, opening a domain of exploration down to very faint, even invisible objects, since there is no need to measure the light of the lens system itself. This method is usually applied on very distant systems (near to the Galactic center): the primary usefulness of gravitational microlensing is thus statistical, as it can reveal whether a star hosts exoplanets and determine

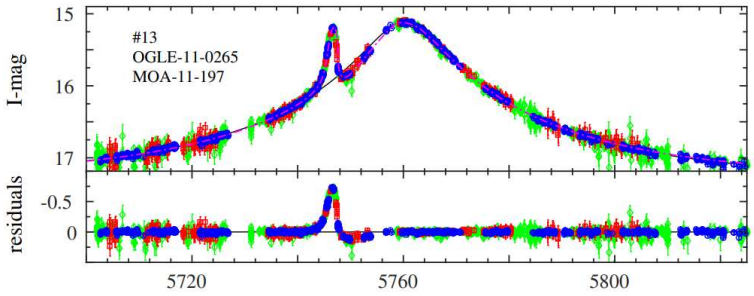

Figure 3.10: Light curve of a microlensing event with a planetary deviation found by the second generation OGLE-MOA-Wise collaboration. The deviation corresponds to a planet of mass $0.6 \pm 0.2\ M_J$. Data by OGLE, MOA and Wise are shown in blue, green and red, respectively. Time is given in $HJD - 2450000$, where HJD stands for Heliocentric Julian Date (Shvartzvald et al. [2016]).

their separation from the star. However, it provides limited characterization, lacking details such as the planetary radius or atmospheric properties.

3.5 Timing

An orbiting planet is accompanied by the periodic oscillation of the position of the host star about the system barycenter, and if the star possesses some periodic time signature, this can provide an alternative route for the detection of orbiting planets through the change in measured period due to light travel time. Three classes of objects have this peculiar behaviour: radio pulsars, pulsating star and eclipsing binaries. Radio pulsars are the preferred targets for timing measurements: they provide short-period and extremely stable timing signals, and the precision that can be achieved when measuring the orbits of pulsars is so high that even small asteroids can, in principle, be discovered. If the pulsar has one or more companions, they can be detected in a variation of the pulses arrival times due to the reflex motion of the pulsar.
The amplitude of time of arrival variations can be expressed as:

$$\Delta t = \frac{M_p a \sin i}{M_\star} \ , \tag{3.5.1}$$

which, for a circular edge-on orbit of period P, and assuming a canonical pulsar mass of 1.35 $M_\odot$, can be written as:

$$\Delta t \approx 1.2 \ \frac{M_p}{M_\oplus} \ \left(\frac{P}{1\ yr} \right)^{2/3} \ ms \ . \tag{3.5.2}$$

A timing precision of about 100 ns is not uncommon anymore, so path-length differences of only 30 m can be detected, translating into a sensitivity to small-mass orbiting bodies, down to asteroid-like objects. The task is to study the

timing results of pulsars to find indications of a planetary companion and to determine, or at least constrain, the orbital period P, the projected semi-major axis of the orbit $a \sin i$ (i is usually unknown), the orbital eccentricity e, the argument of pericenter ω and the time of pericenter passage T_0.

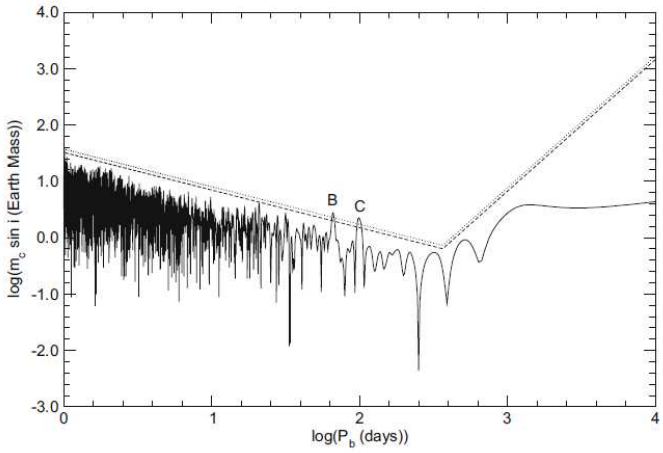

Figure 3.11: Results of a spectral analysis of timing residuals obtained for the pulsar PSR B1257+12. This plot reveals the presence of two significant periods exceeding the 95% and 99% threshold lines, related to planets B and C with orbital periods of 66 and 98 days (Kramer [2018]).

In 1992, the first evidence of an exoplanet was discovered around the millisecond pulsar PSR 1257+12, as reported in Wolszczan and Frail [1992]. In that study, the authors used precise timing measurements from the Arecibo radio telescope to demonstrate that the pulsar is orbited by two planets with minimum masses of $2.8\,M_\oplus$ and $3.4\,M_\oplus$ and orbital periods of 98.2 and 66.6 days, respectively (Figure 3.11). The existence of these planets was later confirmed in Wolszczan [1994], which also revealed the presence of a third, lower-mass planet with a mass of approximately $0.02\,M_\oplus$, still among the least massive exoplanets known to this day.
Being this technique able, at least in principle, to detect even asteroid-like objects, thousands of planets would be expected to be discovered, but only 229 have been confirmed, up to November 2024. To resolve this apparent paradox, it is necessary to consider the formation scenarios that could account for the presence of planets orbiting pulsars. There are three possible scenarios: the planetary disk forming the planet is the result of material from the supernova that created the pulsar; the supernova destroys the binary companion and the neutron star takes material from this companion; the system is the result of a merger and tidal disruption of a C/O white dwarf by the neutron star. Understanding which is valid is still a matter of debate, and the correct one must explain this scarcity of planets.

Chapter 4

High-Contrast Imaging

The real voyage of discovery consists not in seeking new landscapes, but in having new eyes.
– M. Proust

One of the most ambitious goals in exoplanetary science is the direct detection of light originating from an exoplanet, either as starlight reflected off its atmosphere or as thermal emission from the planet itself. This task is extremely challenging due to several factors, including the typically small angular separation between the planet and its host star, on the order of a few tenths of an arcsecond for stars located within 100 pc of the Sun, and the extreme difference in brightness between the two (approximately 10^{-6} for young, Jupiter-like planets). In this context, the term high-contrast imaging (HCI) refers to the combination of instrumental hardware, image processing techniques, and observing strategies specifically designed to detect very faint sources such as planets and circumstellar disks located in close proximity to bright stars. An example of a HCI observation performed on the Gliese 229 system is shown in Figure 4.1. The radiation emitted by a planet consists of two distinct components: a reflected component, dominant in the optical range, and an intrinsic thermal component, which prevails in the infrared. The first depends on the brightness of the host star, the planet-star separation, and the planet's albedo $A(\lambda, t)$, which in turn varies with wavelength and time. For a planet with radius R_p orbiting its host star at an orbital distance a, the reflected flux can be expressed as:

$$F_{p,\,reflected} = A(\lambda, t)\phi(t)\frac{R_p^2}{4a^2}B(\lambda, T_{eff})R_\star^2\,, \tag{4.0.1}$$

where $B(\lambda, T_{eff})$ is the brightness of the host star and $R_\star$ is the stellar radius. $\phi(t)$ is the phase angle, which is defined as the angle between the observer-planet direction and the planet-star direction, and varies from 0 to π radians. The fraction of the planetary surface illuminated by the star is given by a phase law $f(\phi)$ which, for a Lambertian sphere, valid for high albedo atmospheres,

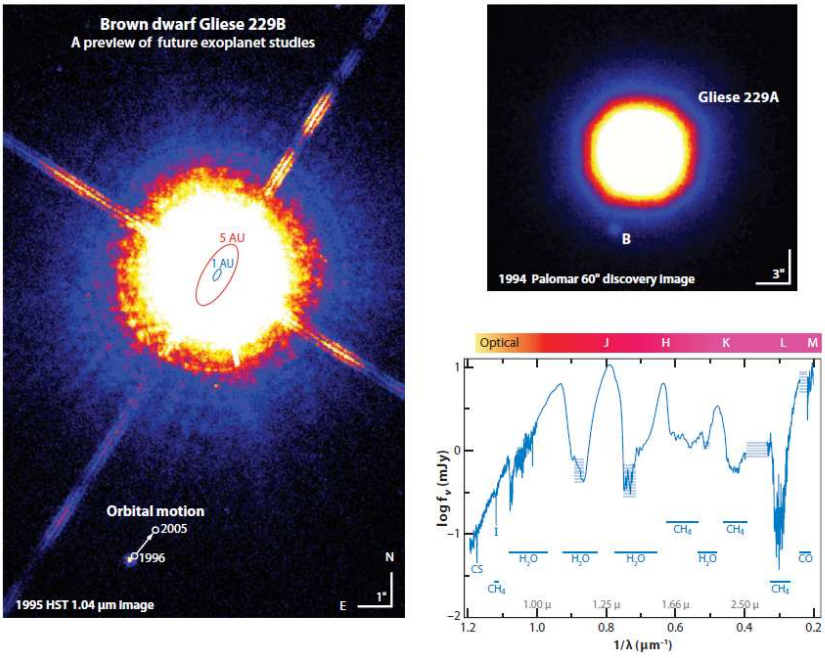

Figure 4.1: Hubble Space Telescope and Palomar observations of the Gliese 229 system, an M-dwarf, T-dwarf pair discovered with coronagraphy. *Left*: the Gliese 229 system observed with Hubble. *Upper right*: the Gliese 229 system observed with Palomar. *Bottom right*: the Gliese 229 B spectrum. Image taken from Oppenheimer and Hinkley [2009].

takes the following expression (Traub and Oppenheimer [2010]):

$$f(\phi) = [\sin\phi + (\pi - \phi)\cos\phi]/\pi \ . \tag{4.0.2}$$

The albedo represents the fraction of the stellar light reflected by the planet, and both geometrical (A_g) and Bond albedo (A_B) are considered to describe the reflective properties of a planet. The geometrical albedo is the ratio between the planet brightness at zero phase angle and the brightness of a perfectly diffusing disk with the same position and apparent size of the planet. The Bond albedo is instead the ratio between the power reflected and the power incident on the planet integrated on the whole solid angle and wavelengths. The two are related by the phase integral q, according to $A_B = qA_g$. The component of the flux emitted by a planet can be estimated as that of a black body at the same temperature T_p of the planet, according to:

$$F_{p,\,emitted} = \epsilon_{IR} B(\lambda, T_p) R_p^2 \ , \tag{4.0.3}$$

where ϵ_{IR} is the emission coefficient of the planet, depending on the wavelength and on the chemistry of the planet surface and atmosphere. The planet's tem-

perature results from the combination of the absorbed stellar radiation and the planet's internal heat. When the contribution of internal heat is negligible, the temperature is referred to as the equilibrium temperature (T_{eq}). Conversely, if internal heat plays a significant role, the more appropriate term is the effective temperature (T_{eff}). These two temperature differ from each other only if internal heat is present. Assuming that the incident flux is equal to the radiated flux, the equilibrium temperature can be expressed as:

$$T_{eq} = \left(\frac{1 - A_B}{4f}\right)^{1/4} \left(\frac{R_p}{a}\right)^{1/2} T_\star \ , \tag{4.0.4}$$

where f is the heat redistribution factor. It is equal to 1 when the thermal emission originates from the entire planetary surface, a scenario typical of rapidly rotating planets where heat is efficiently redistributed. Conversely, it assumes a value of 0.5 when the emission comes only from the dayside hemisphere, as is the case for tidally-locked planets, which rotate synchronously with their host star. The ratio between the planetary flux (both emitted and reflected) and the stellar flux is defined as contrast, which is a function of the wavelength, properties of the planet such its age, and the apparent geometry of the planet-star system. It can be written as:

$$C = \frac{F_{p,\,reflected} + F_{p,\,emitted}}{F_\star} \ . \tag{4.0.5}$$

The age of a planet plays a crucial role in determining the achievable contrast, since young planets possess a higher intrinsic luminosity and can be several orders of magnitude brighter than older planets. In the near-infrared range (1–3 μm), giant planets aged a few to a few tens of Myr typically exhibit contrasts in the range of $\sim 10^{-5}$ to 10^{-6}. At longer wavelengths (3–5 μm), the same planets can reach contrasts of $\sim 10^{-3}$ to 10^{-4}: this is because, at temperatures of approximately 500–1500 K, the thermal emission of young giant planets peaks in this wavelength range, making it, on this point of view, the most favourable spectral window for detecting such objects via direct imaging. However, most high-contrast imagers operate in the near infrared, as this wavelength range allows for higher spatial resolution, enabling the detection of companions at smaller angular separations compared to the mid-infrared. In the optical region, as stated before, planets are seen in reflected light. As an example, at 4.5 Gyr, Jupiter and Earth have contrasts of $\sim 10^{-9}$ and 10^{-10}, respectively, at 0.5 μm. Figure 4.2 shows how the contrast vary for various types of exoplanets orbiting a G2V star. In the near IR young super-Jupiter planets are approximately 10^{-3} to 10^{-5} fainter than a Sun-like star, while in the mid-IR predicted contrasts for these planets are 10 times smaller. A Jupiter analog emits negligible thermal emission in the band $\lambda \sim 4 - 5\,\mu m$.

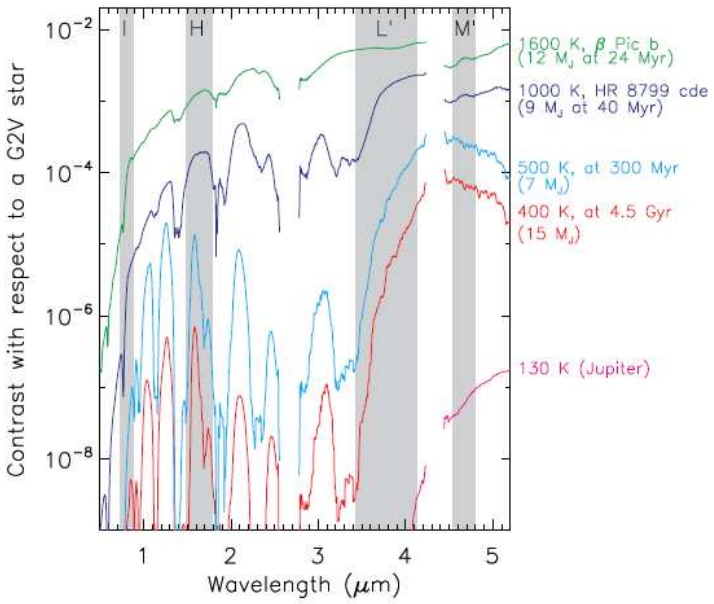

Figure 4.2: Contrast ratio in optical, near IR and mid-IR for models for known directly imaged planets (β Pic b and HR 8799 cde), models for older cooler exoplanets and Jupiter, assuming a G2V host star. Image taken from Currie et al. [2023].

Detecting a planet through direct imaging enables the measurement of its position via relative astrometry with respect to the host star, and its brightness through photometric observations. When combined with evolutionary models, photometric data can be used to infer the planet's mass, provided that the distance and age of the system are well constrained. Moreover, by comparing the detection limits of imaging surveys with evolutionary models, it is possible to place statistical constraints on the occurrence rate of exoplanets across different mass and orbital separation ranges, those to which direct imaging is most sensitive. In addition, spectroscopy of directly imaged companions allows for a direct atmosphere characterization. Low-resolution spectra can reveal information about the atmospheric composition, and when combined with atmospheric models, can be used to infer the temperature–pressure profile and estimate key parameters such as the carbon-to-oxygen (C/O) ratio.
High-contrast imaging is a technique particularly well suited for detecting planets on wide orbits, as illustrated in Figure 1.1. Indeed, companions located farther from their host star have larger angular separations, making them more accessible to current imaging capabilities. In this sense, direct imaging is complementary to other detection methods, as it enables the identification of distant companions, exploring the outer part of exoplanetary systems, within a reasonable amount of telescope time, without requiring the extended observational

baselines that techniques like radial velocity would demand for similar detections.

Young planetary systems are also prime targets for direct imaging, as they can be intrinsically brighter than their older counterparts by several orders of magnitude, resulting in higher contrast relative to their host stars and thus enhancing detectability. Under the simplifying assumptions of a polytropic equation of state and a degenerate electron gas, it is possible to derive an analytical relation linking the bolometric luminosity of brown dwarfs and giant planets to their age and mass, taking the form (Stevenson [1991]; Burrows and Liebert [1993]):

$$L_{bol} \propto t^{-5/4} M^{5/2} \,, \tag{4.0.6}$$

where L_{bol} is the bolometric luminosity, t the object's age and M is its mass. In conclusion, young stars are attractive targets for direct imaging since planets are most bright at early ages. Figure 4.3 shows the luminosity evolution of different objects with different masses versus age, according to the theoretical model by Burrows et al. [2001].

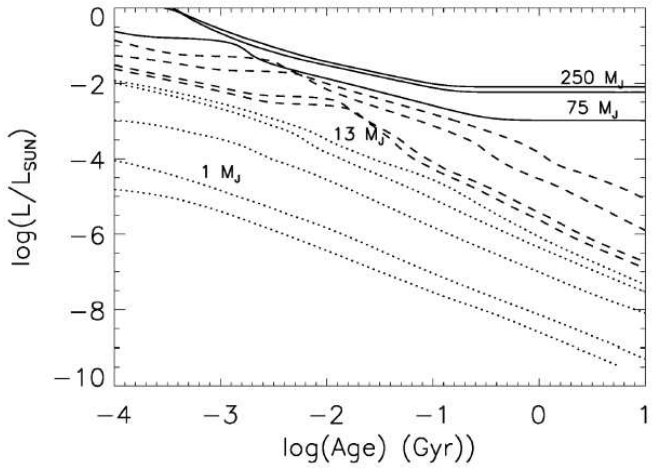

Figure 4.3: Theoretical models for the luminosity evolution of different objects with different masses versus age. Stars are shown in continuous line, sub-stellar structures with $M < 13\,M_J$ in dashed line, and giant planet in dotted line. Young planets are brighter by several orders of magnitude with respect to old planets. Plot taken from Claudi and Mesa [2025].

Before delving into the main processes, instruments, and algorithms employed in high-contrast imaging, it is essential to first describe how images form on the focal plane of a telescope, highlighting the fundamental limitations that this technique must overcome. The light coming from a far away star, focalized on the focal plane of the telescope, can be considered as a plane wavefront. For example, for a star located 10 pc away, the deviation from a plane wavefront is less than one part on 10^{17} for a 4-m telescope. Once that the light has entered

through the telescope aperture, according to Huygens' principle, each point of the aperture becomes an emission center of spherical waves that are focalized onto the focal plane of the telescope. In this case, in which the light source can be considered at the infinite, Fraunhofer diffraction can be employed to give exact results. Considering a circular aperture of diameter D, and an incoming wavefront with amplitude $A(x) = 1$, with x a position on the aperture, the amplitude on the focal plane of the telescope can be expressed as:

$$A_2(\theta) = \sqrt{I_0}\frac{2J_1(\pi D\theta/\lambda)}{\pi D\theta/\lambda} , \tag{4.0.7}$$

and the corresponding intensity is $I_2 = |A_2|^2$, obtaining:

$$I_2(\theta) = I_0\left[\frac{2J_1(\pi D\theta/\lambda)}{\pi D\theta/\lambda}\right]^2 , \tag{4.0.8}$$

with $J_1(x)$ the Bessel function of first order and θ the angle between the optical axis and the point of observation. The first zero-intensity angle is $\theta = 1.22\lambda/D$, often referred to as the Airy disk radius (e.g. for a 8-m telescope at a $\lambda = 1\ \mu m$, this is of the order of ~ 30 mas). The intensity is most concentrated in the first peak, then has secondary rings separated by the minima of the function, with decreasing energy: in particular, in a perfect diffraction-limited system, the central Airy disk contains $\sim 84\%$ of the total light in the point spread function. In the case of a telescope with a circular aperture and a central obscuration, like a telescope secondary mirror, the Airy pattern has a functional form of:

$$I(u) = \frac{1}{(1-\epsilon^2)^2}\left[\frac{2J_1(u)}{u} - \epsilon^2\frac{2J_1(\epsilon u)}{\epsilon u}\right]^2 , \tag{4.0.9}$$

where $u = \pi D\theta/\lambda$ and ϵ is a measure of the amount of central obscuration expressed as a fraction of the total aperture. For $\epsilon = 0$ it correctly reduces to equation 4.0.8. The full width at half maximum (FWHM) of the intensity pattern is $\theta = 1.03\lambda/D \approx \lambda/D$, and is typically used to define the diameter of the diffraction-limited image of a point source collected by a telescope with diameter D.

For ground-based telescopes, the light from a star passes through the Earth atmosphere, which has a thickness of about 20 km, and the resolution is lowered to λ/r_0, where r_0 is the Fried parameter (view Section 4.1 for more details), the indicative size of the seeing cell. The Fried parameter is strongly dependent on the wavelength, scaling as $r_0 \propto \lambda^{6/5}$, and it is about 10 cm in the visible. Within a single turbulent cell in the atmosphere, the refractive index of the air can be considered constant, but it differs from that of adjacent cells. As a result, the incoming wavefront becomes distorted, leading to a degradation of the image quality, an effect commonly referred to as atmospheric seeing. Table 4.1 gives a comparison between the diffraction-limited resolution of an 8-m telescope and the seeing-limited resolution at 0.55 μm (V band), 1.6 μm (H band) and 3.5 μm (L band) under good weather conditions ($0.25''$ seeing at V band).

Distance (pc)	Resolution (AU)		
Seeing-limited observations			
	$0.55\,\mu m$	$1.65\,\mu m$	$3.5\,\mu m$
50	12.5	46.5	115
150	37.5	140	345
Diffraction-limited observations			
50	0.9	2.6	5.5
150	2.6	7.8	16.5

Table 4.1: Seeing (r_0) and diffraction (θ) limited resolutions at three common HCI wavelengths for an 8-m telescope with a 0.25″ seeing at V band (Follette [2023]).

One way to overcome this limitation is to employ space-based telescopes, which operate outside the Earth's atmosphere and are thus immune to seeing effects. For ground-based observations, however, adaptive optics systems, designed to correct in real time for the distortions introduced by the atmosphere, are essential. An image acquired without any wavefront correction typically appears as a speckle pattern, which is an ensemble of interference structures arising from coherent patches of the wavefront, each of characteristic size r_0, distributed across the telescope aperture. Figure 4.4 shows an image where the speckle pattern is clearly visible.

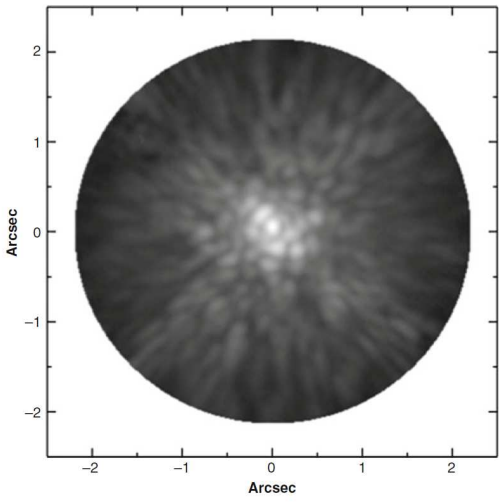

Figure 4.4: Image taken with a coronagraph showing the presence of speckles (Oppenheimer and Hinkley [2009]).

Each of these patches acts like an individual aperture, producing a point spread function (PSF) with a full width at half maximum (FWHM) of approximately λ/r_0. Furthermore, any two patches separated by a distance D (the diameter of the telescope) effectively form an interferometer, creating an interference pattern on the focal plane with a fringe spacing of order λ/D. These fringes are oriented orthogonally to the line connecting the two patches. Each couple of cells represents an interference pattern which, if the interference is constructive, produces a bright speckle. The random phase variation of the incoming wavefront makes the intensity of the speckles to vary in a random way, while the positions of the speckles are a function of the wavefront perturbations and the wavelength of the observed light. Speckles can originate both from the atmospheric turbulence, resulting in short-lived phenomena, and from imperfections in the optics of the telescope, which give rise to long-lived, quasi-static speckles. The latter are mostly permanent during the exposure, with typical lifetimes of minutes. In both cases the resulting image is composed by a weakened image of the star surrounded by an highly-variable background. In this context, the atmospheric coherence time (τ_0) can be introduced, defined as the characteristic timescale over which the incoming wavefront maintains a near-constant phase structure, both temporally and spatially. More specifically, it represents the timescale over which optical paths deviate by less than 1 rad of root mean square (RMS) phase aberration from each other, and is proportional to r_0/v_{wind}, where v_{wind} denotes the average wind speed. The coherence time varies from site to site, depending on the atmospheric conditions, typically ranging from a few to 15-20 milliseconds. A ground-based image of a star is therefore composed of approximately $(D/r_0)^2$ speckles, which evolve on a τ_0 timescale and distributed over an angular diameter on the sky of about λ/r_0, independently on the telescope diameter. Generally, speckles do not follow Poisson statistics and exhibit correlated noise properties. As a result, they cannot be averaged out by simply increasing the integration time or by using broadband observations across wide wavelength ranges. The speckles are brighter going closer to the star, and this is a limitation for direct imaging.

Overall, the direct imaging of faint companions presents several challenges, which can be addressed through the use of dedicated instrumentation and observing techniques. Achieving high angular resolution, essential to resolve objects located close to their host stars, requires large-aperture telescopes. To correct for atmospheric turbulence, these telescopes must be equipped with adaptive optics systems. The stellar light must also be attenuated or removed, which is accomplished using coronagraphic devices. Finally, to reach the contrast levels required for the detection of faint companions, speckle noise must be mitigated or ideally suppressed. Several advanced techniques have been developed and optimized to achieve this goal.

4.1 Adaptive Optics

As previously discussed, the atmospheric turbulence distorts the wavefront of the incoming light, causing deviations from an ideal, planar shape and thereby reducing the resolution. Without correction, the resulting atmospheric seeing would significantly limit the achievable contrast, precluding the direct detection of exoplanets. In order to correct for these effects and ideally achieve diffraction-limited images, modern telescopes are equipped with adaptive optics (AO) systems. The first astronomical AO instrument, COME-ON, was tested at the 1.52-m telescope of the Observatoire de Haute-Provence (Merkle et al. [1989]; Rousset et al. [1990]) and later installed at ESO's 3.6-m telescope at La Silla Observatory. Figure 4.5 shows two images of γ_2 And taken with COME-ON, highlighting the difference between an uncorrected image and one corrected with AO.
The performance of an AO system is commonly quantified by the Strehl ratio (SR), defined as the ratio between the peak of the PSF measured in the detector and the theoretical diffraction-limited PSF collected with the same instrument. This ratio, which depends on the wavelength at which the instrument is operating, is typically expressed as a percentage. In the case of a perfect instrumentation, this ratio is equal to 100%, while most AO systems operate at a SR of around $20 - 60\%$. The larger the wavefront error, the lower the SR: for this reason the Strehl ratio is higher at longer wavelengths. If the RMS of the wavefront error in radians, denoted σ_W, is much smaller than 1, the Strehl ratio can be approximated as $SR \sim \exp(-2\pi\sigma_W^2)$ (Ross [2009]).

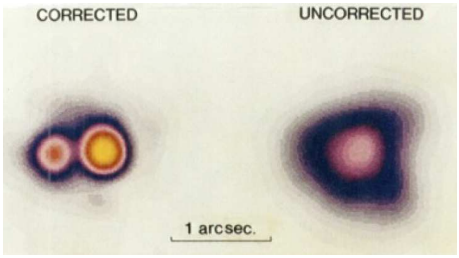

Figure 4.5: Images of γ_2 And collected with the COME-ON AO prototype system at K band. *Left*: image corrected with AO. *Right*: uncorrected image (Rousset et al. [1990]).

The turbulent structure of the atmosphere can be modeled as an ensemble of small cells within which the refractive index is approximately constant, with their characteristic size defined by the Fried parameter. This parameter represents the spatial scale over which the wavefront statistically varies by less than 1 radian of RMS phase aberration, and is defined as (Beckers [1993]):

$$r_0 \propto \lambda^{6/5} \left[\int_0^\infty C_n^2(h) dh \right]^{-3/5} , \tag{4.1.1}$$

where $C_n^2(h)$ is a function of the altitude h and of the refractive index n, characterizing the turbulent structure of the atmosphere. Another important quantity is the isoplanatic angle $\theta_0 \propto (cos\gamma)r_0/h$, with γ the elevation angle and h the characteristic height of the turbulence, which describes the angle out to which optical path variations deviate by less than 1 rad of RMS phase aberration from each other.

In a first-order approximation, the effect of the Earth's atmosphere on incoming starlight can be modeled as a plane-parallel wavefront propagating through a turbulent atmospheric layer, structured as an ensemble of cells of size r_0. Within each cell, the wavefront phase is aberrated, perturbing the incoming PSF and blurring the diffraction image. When restricting the analysis to the lowest order aberrations, the so-called tip and tilt modes, the intrinsic shape of the PSF remains unchanged, although the propagation direction of the wavefront is altered with respect to the original path. As a result, a wavefront exiting an atmospheric layer is no longer plane-parallel, but it is corrugated, with the angle of arrival varying across the telescope aperture. The main duty of an adaptive optics system is then the reconstruction of the original, unperturbed wavefront, with the timescale for these corrections determined by the atmospheric coherence time τ_0, resulting in correction frequencies typically ranging from approximately 0.2 to 1 kHz.

The first step in AO is achieved with a tip and tilt system, or fine-guidance tracker. This system corrects for large movements (up to a few arcseconds) of the stellar PSF due either to atmospheric variations, wind or vibration in the telescope. Once the image of the star has been stabilized by the fine-guidance tracker, the remaining correction of the wavefront is performed with a deformable mirror (DM). The restoration of the plane structure of the wavefront is achieved by measuring its deviations with a wavefront sensor (WFS), calculating a proper correction, and applying it to the DM. This correction loop is performed hundreds of times per second, according to the timescale of the atmospheric changes set by the coherence time τ_0.

A deformable mirror is a device designed to correct for the optical path differences introduced by atmospheric turbulence. It typically consists of an array of actuators connected to a thin optical surface, which deforms under the expansion of the actuators. The number of actuators is a key parameter in adaptive optics systems, as a higher number of actuators enables finer deformations and thus more accurate wavefront corrections. In fact, AO systems cannot correct atmospheric effects on spatial scales smaller than the actuator spacing. Ideally, the size of the actuators should approximately match the Fried parameter r_0. The number of actuators also plays a role in defining the angular distance up to which AO systems remain effective. In fact, adaptive optics can correct wavefront errors up to a separation known as the outer working angle (OWA). This angle corresponds to spatial frequencies above $N_{act}\lambda/(2D)$, where N_{act} is the number of actuators along one linear dimension of the deformable mirror, and D is the telescope aperture. A wavefront sensor is a real-time device that measures the incoming wavefront, providing a signal from which its shape can be estimated with sufficient accuracy. A typical WFS setup includes a phase-sensitive opti-

cal device (or sensing scheme) and a low-noise, high-quantum-efficiency photon detector. The main sources of uncertainty in a wavefront sensor are photon noise, chromaticity, aliasing, time delay, scintillation, and non-common path errors. When AO systems operate in closed-loop mode, with corrections being applied in real time, if the sensed wavefront deformations require corrections whose amplitudes exceed the control range of the DM, the loop will open to protect the mirror. This is called a breaking of the AO control loop. In this context, an important parameter for the WFS is the control gain, which acts as a multiplicative factor applied to the sensed wavefront, ensuring that the entire measured aberration is not corrected at once, but only a fraction of it. This approach helps to avoid overcorrection and allows unsensed or incorrectly sensed aberrations to pass without breaking the loop. The control gain can be adjusted in real time during observations, and it is one of the key parameters determining the ability of the AO loop to remain closed throughout an observation. A schematic representation of how an AO system works is shown in Figure 4.6.

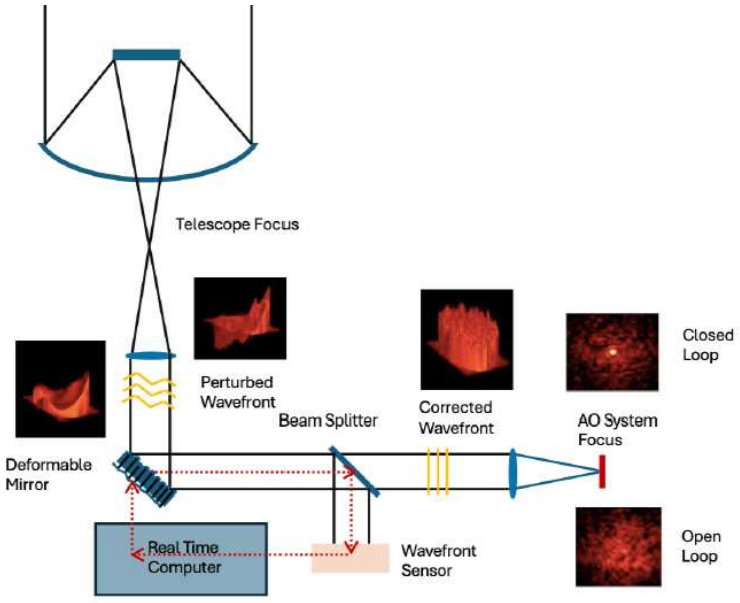

Figure 4.6: The principle of an adaptive optics system. Image taken from Claudi and Mesa [2025].

This setup uses WFS observations of a single guide star to correct the wavefront in its direction and is referred to as single-conjugate adaptive optics (SCAO). This technique suffers from image degradation over the field of view, set by the isoplanatic angle θ_0. To accurately analyze the wavefront, AO systems require sufficiently bright guide stars (typically $V \sim 15$ mag) located within θ_0 of the target. Since this condition cannot always be met with natural stars, it can be

overcome using laser guide stars (LGSs), a concept that was first suggested in astronomy by Foy and Labeyrie [1985]. LGSs rely on two physical mechanisms: Rayleigh scattering in the denser atmospheric layers up to altitudes of about 30 km, and resonance fluorescence from sodium atoms concentrated in a layer around 90 km altitude. The principle is to use a laser beam projected from the ground and reflected by the upper layers of the atmosphere, creating a bright artificial source of light that experiences the same wavefront distortions as a real star. This technique also has some limitations. For example, due to the finite distance between the telescope and the laser star, the backscattered beam does not fully sample the telescope aperture at the altitude of the turbulent atmospheric layers. To overcome this effect, measurements from several LGSs can be combined to reconstruct the complete turbulence profile in the direction of the target. There are also several types of AO systems designed to probe different turbulent layers by using various combinations of natural and laser guide stars. The scheme of a typical LGS system is shown in Figure 4.7.

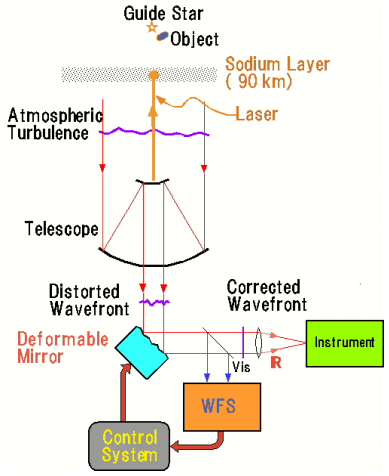

Figure 4.7: Scheme of a LGS system. Credits: National Astronomical Observatory of Japan (https://subarutelescope.org/old/Pressrelease/2005/07/06/index.html)

In the last decade, most of the new-generation high-contrast imagers have been equipped with extreme AO (ExAO) systems, designed to fully correct for both atmospheric and instrumental perturbations. While conceptually similar to SCAO, their implementation is technically challenging. The main goal is to achieve high performance on bright stars ($V < 10$ mag), aiming for a Strehl ratio greater than 90% in the H band, ultimately enabling a contrast improvement by a factor of 10–100 at sub-arcsecond separations. ExAO systems have been built upon hardware advancements in three key areas: detectors, deformable mirrors, and computing hardware. Fast, low-noise detectors such as Electron-Multiplying Charge-Coupled Devices (EMCCDs) are used to capture stellar

photons for wavefront sensing, minimizing measurement errors. Deformable mirrors with over 10^3 actuators, along with wavefront sensors capable of operating at frequencies $\gtrsim 1$ kHz, are employed to enable fast and precise corrections of the incoming wavefront.

4.2 Coronagraphy

The correction performed by adaptive optics, although necessary, is not sufficient to enable high-contrast observations. AO systems, through wavefront correction, ideally produce diffraction-limited images characterized by an Airy pattern. However, this pattern remains several orders of magnitude brighter than an exoplanet or any faint companion. To make their detection possible, the stellar diffraction peak must be suppressed, which is achieved with a coronagraph. A coronagraph is an instrument specifically designed to attenuate the stellar light, thereby allowing the detection of faint objects close to the star, originally invented by Lyot (Lyot [1939]) to observe the Sun. In order to highlight this necessity, consider a telescope of diameter D equipped with a detector observing a point-like star with flux F_s at a wavelength λ. The intensity of the star's PSF at a separation $\mathbf{x}$ from the star center is denoted as $PSF(\mathbf{x})$. Now, consider an exoplanet with a flux F_p (where typically F_p/F_s ranges from 10^{-4} to 10^{-10}), whose image appears as a PSF centered at position $\mathbf{x}$. Assuming a perfect telescope and a noiseless detector, the signal-to-noise ratio (SNR) for the detection of the exoplanet, calculated on a single pixel, can be expressed as:

$$SNR_{P,S}(t_{exp}) = \frac{F_p t_{exp} PSF(0)}{\sqrt{F_p t_{exp} PSF(0) + F_s t_{exp} PSF(\mathbf{x})}} , \tag{4.2.1}$$

that is the ratio between the exoplanet signal and the photon noise originated from the star and exoplanet light, with t_{exp} the exposure time. In the absence of the star, $SNR_P(t_{exp}) = \sqrt{F_p t_{exp} PSF(0)}$. In order to link the SNR in presence and absence of the star, Equation 4.2.1 can be written as:

$$SNR_{P,S}(t_{exp}) = SNR_P(t_{exp}) \left(1 + \frac{F_s}{F_P} \frac{PSF(\mathbf{x})}{PSF(0)}\right)^{-1/2} . \tag{4.2.2}$$

Considering, as an example, the presence of a Jupiter-like planet orbiting a Sun-like star ($F_p/F_s \sim 10^{-9}$) at a projected distance of $|\mathbf{x}| = 5\lambda/D$, $SNR_{P,S}(t_{exp}) \approx 10^{-3} SNR_P(t_{exp})$. The presence of the star reduces the expected SNR by a factor of 10^3, meaning that, to achieve the same SNR, the integration time would need to be 10^6 times longer compared to the case without the star. Therefore, in order to detect exoplanets and faint companions within a reasonable amount of time, the stellar light at the position of the exoplanet (represented by $PSF(\mathbf{x})/PSF(0)$) must be minimized.
An optical system can be modeled as a succession of conjugate planes. Using the Fraunhofer approximation, the electric field in a plane is given by the Fourier transform of the electric field in the preceding plane. At each stage,

the field amplitude can be modified by masks, stops, polarization changes, and phase shifts; all of these effects contribute to the net transmitted amplitude before applying the Fourier transform and moving to the next plane. The final observed amplitude is thus the result of all these transformations. For a given spectral filter centered at λ with a bandwidth $\Delta\lambda$, the recorded intensity $I_{D,\Delta\lambda}$, where D denotes the imaging plane, is the integration of the monochromatic intensity over the filter bandwidth. Furthermore, if two orthogonal polarization states p are considered, the total intensity is obtained by summing the intensities corresponding to each polarization state, as:

$$I_{D,\Delta\lambda} \propto \sum_{p} \int_{\lambda-\Delta\lambda/2}^{\lambda+\Delta\lambda/2} I_D(\boldsymbol{x}, \lambda, p) d\lambda \,, \tag{4.2.3}$$

with I_D the intensity for a monochromatic source at wavelength λ, and $\boldsymbol{x}$ the position in the imaging plane.

There are many different types of coronagraphs, which can be broadly divided into two main categories: coronagraphs with occulting masks and phase-mask coronagraphs. The first class uses an opaque mask that attenuates the central peak of the Airy disk, while the second class induces a phase shift in part of the starlight in the focal plane, creating destructive interference for the on-axis starlight within the telescope pupil, thus blocking the stellar light.

The most common type of coronagraph is the classical Lyot coronagraph (shown in Figure 4.8), which uses two masks (the occulting mask and the Lyot stop) to suppress starlight. The incoming light is collected by the telescope's primary mirror, and its pupil is optically conjugated to the entrance pupil of the coronagraphic system. In this plane, a pupil apodizer can be used to modify the phase and amplitude of the incoming wavefront in order to optimize the diffraction pattern in the subsequent focal plane, and in this case the coronagraph is denoted as Apodized Lyot coronagraph (ALC). This approach is based on the apodization technique, which reduces discontinuities at the pupil edge by decreasing the amplitude of the secondary maxima of the diffraction pattern and also reduces the contribution to the overall noise budget from speckles that are pinned to the Airy rings, that tend to be brighter than other speckles.

The starlight is focused onto a focal plane mask which, in the classical Lyot design, is a small circular opaque mask. This mask can induce spatial phase shifts or differential transmission on the electric field of the wavefront. The combined action of the focal plane mask and the apodizer (if present) separates the light of the star from that of a faint nearby object. The star's light is diffracted around the opaque mask, concentrating most of the residual starlight into a bright inner and outer ring in the pupil plane, around the conjugate position of the telescope's secondary mirror. In contrast, light from an off-axis source (such as a companion) is not focused onto the center of the focal plane mask and thus passes through the coronagraph almost unaffected. The coronagraph therefore acts as an optical filter, attenuating on-axis light while transmitting off-axis light, enabling the detection of faint objects close to the star. In the pupil plane, a Lyot stop is inserted to slightly reduce the telescope aperture

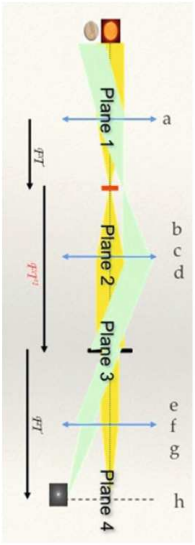

Figure 4.8: The optical scheme of a classical Lyot coronagraph, showing the light coming from the star (yellow, on axis) and from the planet (green, off axis). The scheme is so structured: (a) primary pupil for on axis source; (b) image before image plane stop; (c) image plane stop; (d) image after image plane stop; (e) pupil before Lyot stop; (f) Lyot stop; (h) final on axis image. Modified from Sivaramakrishnan et al. [2001].

and increase the central obscuration, blocking most of the remaining diffracted starlight. The final image, formed after the Lyot stop, shows the star's intensity reduced by more than 99%, while the light from a nearby object is only marginally affected, typically by a few percent. In practice, the effects of optical aberrations must be taken into account. In particular, phase aberrations, delays or advances of portions of the wavefront relative to an ideal flat wavefront, and amplitude aberrations, local variations in the beam's transmission, can have some impact on the coronagraph's ability to diffract and suppress starlight.
Each coronagraph is characterized by several parameters that describe its performance and effectiveness. The main parameter is the inner working angle (IWA), defined as the angular radius at which the peak flux of the star is attenuated by 50%. Typical IWA values range from approximately $\sim 2\lambda/D$ to $\sim 4\lambda/D$. One of the key goals of new coronagraph designs is to minimize the IWA as much as possible, enabling the detection of companions at smaller angular separations from their host stars. To detect objects located at separations smaller than the IWA, observations without a coronagraph are possible, although not recommended, as the stellar light would overwhelm the faint companion signal. Another important parameter is the planet throughput, defined as the fraction of the planet's light that survives the starlight suppression process of the

coronagraph. Most coronagraphs achieve throughputs of about $\sim 80\%$. Additionally, two parameters relate to the sensitivity of the coronagraph to low-order wavefront aberrations (such as tilt, focus, and astigmatism) and its chromaticity, which quantifies the coronagraph's ability to suppress starlight over a wide range of wavelengths. Lower chromaticity values indicate better performance. Another key quantity is the normalized intensity, representing the fraction of the incoming stellar PSF that remains after the coronagraphic suppression. Normalized intensity values typically range from 1 at the center of the focal plane in the absence of a coronagraph, down to 10^{-10} or better for high-performance coronagraphic systems. The overall performance of a coronagraph can be quantified by the standard deviation of the normalized intensity across the final image.
Apart from the classical Lyot and its apodized variant, the most widely adopted coronagraph types in HCI include:

- Four Quadrant Phase Mask (4QPM): the mask, placed in the focal plane, consists of four contiguous quadrants of transparent material, with the starlight focused at the central point of symmetry. Adjacent quadrants differ in optical thickness by $\lambda/2$, introducing a π phase shift on two quadrants in a diagonal with respect of the two others. This phase difference causes destructive interference at the center, effectively suppressing the starlight, while off-axis sources falling within a single quadrant are transmitted. 4QPM coronagraphs offer high throughput and achieve an IWA of λ/D, but are highly sensitive to the precise centering of the star in the focal plane. They are used in several ground-based instruments, including SPHERE. Figure 4.9 shows the 4QPM coronagraph used in SPHERE, as described in Boccaletti et al. [2004].

- Optical Vortex Coronagraph: the phase mask, which operates on both polarizations, imposes an azimuthally varying phase ranging from 0 to 2π, resulting in destructive interference of the starlight (Traub and Oppenheimer [2010]). This approach is particularly effective at achieving high contrast at small IWA. Vortex coronagraphs are currently employed at wavelengths $\lambda > 3\,\mu m$, particularly in the L band.

- Apodizing Phase Plate (APP): a type of coronagraph that modifies the incoming wavefront by altering only its phase (Kenworthy et al. [2007]). As a consequence, APP coronagraphs typically offer higher throughput compared to amplitude apodizers.

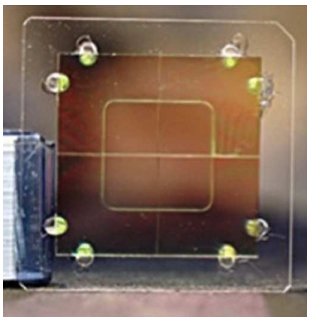

Figure 4.9: The 4QPM coronagraph of SPHERE

One practical consequence of coronagraphy is the loss of a direct measurement of the central star's astrometry and photometry. Precise knowledge of the relative position between the star and a potential companion is essential for various purposes, including the study of orbital motion and the architecture of planetary systems. A widely adopted solution to this problem was proposed by Sivaramakrishnan and Oppenheimer [2006], based on the introduction of a periodic grid of wires with known width and spacing placed in a pupil plane in front of the coronagraphic mask. Nowadays, in new-generation imagers such as SPHERE, the same effect is achieved through an apposite deformation of the instrument's deformable mirror. This configuration produces four fiducial replicas of the obscured star at known positions relative to its true location (an example is shown in Figure 4.10). The intersection point of the two diagonals connecting opposite spots provides an accurate estimate of the star's position. In addition, these calibration spots have a known brightness and can be used to photometrically calibrate other objects in the field of view, either relative to the central star or in absolute terms, provided that the star has been independently calibrated.

4.3 Differential Imaging

The use of adaptive optics systems in combination with coronagraphs, although effective in restoring the telescope's diffraction-limited performance and in suppressing the light from the central star, respectively, is not sufficient to achieve the contrast levels required for the direct imaging of exoplanets and faint companions near the host star. These techniques typically allow a contrast of $\sim 10^{-3} - 10^{-4}$, which is still 2–3 orders of magnitude too low to detect a hot, young exo-Jupiter. The limiting factor lies in the presence of quasi-static speckle patterns in the image, caused by optical aberrations within the telescope, the AO system, the coronagraph, or the science camera, which are not perfectly calibrated or corrected. These speckles closely resemble the appearance of an exoplanet, and can therefore overwhelm the signal of a faint companion.
There are two main strategies for mitigating wavefront errors: actively correct-

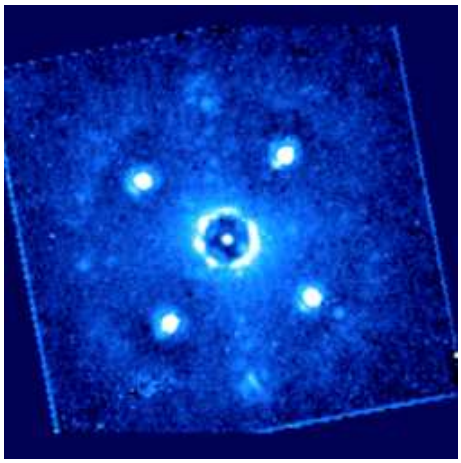

Figure 4.10: Image acquired with SPHERE, showing four symmetric calibration spots used to determine the stellar position behind the coronagraph.

ing them, or removing their manifestations, speckles, through specific data acquisition and processing techniques. Ideally, a combination of both approaches is employed, with the additional goal of further suppressing the stellar halo by several orders of magnitude and transforming the residual noise into a more Gaussian-like distribution (a process known as whitening). These processing techniques exploit the characteristic properties of speckles, particularly their dependence on time, wavelength, and the orientation of the wavefront error sources that generate them. Furthermore, speckles are typically unpolarized, as the starlight itself is generally unpolarized.
In addition to speckle suppression techniques, it is also possible to actively control both the PSF and the speckle pattern using an AO system in combination with specialized wavefront sensors. A speckle can be eliminated by identifying the sinusoidal ripple in the wavefront that produces it, and then applying the inverse ripple via the deformable mirror. This method, described in Trauger and Traub [2007] among others, is an iterative process that requires an extremely sensitive wavefront sensor, typically operating at much lower speeds than conventional AO wavefront sensors. Figure 4.11 illustrates the effect of the so-called "three pillars" of high-contrast imaging: AO, coronagraphy, and differential imaging, which collectively lead to a progressive improvement in contrast and sensitivity, enhancing the detectability of faint companions in close proximity to the host star.

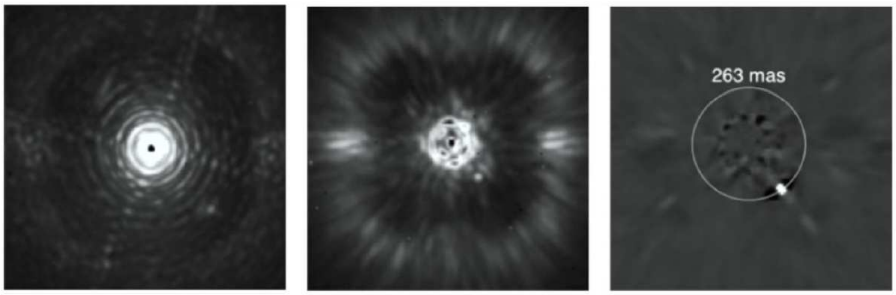

Figure 4.11: Illustration of the "three pillars" of high-contrast imaging. *Left*: raw image obtained with SPHERE/IRDIS in the J-band, using ExAO correction. *Middle*: raw coronagraphic image, where the residual speckle pattern is still visible. *Right*: final result after applying differential imaging and post-processing techniques, revealing the presence of a faint companion in close proximity to the host star.

4.3.1 Angular Differential Imaging

The angular differential imaging (ADI; Marois et al. [2006]) technique is implemented by acquiring images while keeping the instrument and telescope optics pointed on the target star, allowing the field of view to rotate with respect to the instrument due to the natural field rotation of the sky (the so-called pupil-stabilized observations). In particular, for an instrument at Nasmyth focus like SPHERE, the field rotates as the sum of the parallactic and altitude angle, while the pupil rotates as the altitude angle. An optical element can then be located in front of the instrument, stabilizing the image of the pupil on the detector: in this case the field will rotate on the detector with the parallactic angle, with the central star as the center of rotation. In this configuration, the speckle pattern remains stationary in the image plane, while astrophysical sources off axis within the FOV appear at different positions in each frame. For each image, a reference PSF is constructed using the images in the sequence and subtracted to remove the quasi-static speckle pattern, preserving only the signal from real astrophysical sources. The resulting images are then rotated to a common orientation in order to align the FOV. Typically, the reference PSF is estimated by computing the median of all frames in the sequence. However, since the speckle pattern is stable only over timescales of a few minutes, using the full sequence to construct the median PSF may lead to an imperfect subtraction, leaving residual speckle noise. To minimize this effect, only images acquired close enough in time, during which the speckle pattern can be considered approximately constant, should be used to build the reference PSF. Figure 4.12 provides a graphical representation of the ADI method.
Another limitation of the ADI technique is the so-called self-subtraction effect, which refers to the partial removal of the planetary signal, along with the speckle pattern, during the subtraction of the reference PSF. This issue is par-

ticularly pronounced at small angular separations from the host star (less than approximately λ/D). Although self-subtraction cannot be completely avoided and must therefore be modeled and corrected in post-processing, it can be mitigated through observational strategies. In particular, maximizing the field rotation is essential to ensure that the low-mass companion does not remain in similar positions across consecutive frames, thereby improving the efficiency of ADI. When the companion moves significantly over the course of the sequence, its signal becomes well distributed in the temporal median used for PSF estimation, thereby reducing the degree of self-subtraction. To maximize field rotation, targets are typically observed near their meridian passage, when the star reaches its highest altitude in the sky. The rotation rate ψ (in $^\circ/min$) of the FOV is calculated as:

$$\psi = 0.2506 \frac{\cos A \cos \phi}{\sin z} \ , \tag{4.3.1}$$

where A is the target azimuth, z the zenith distance and ϕ the telescope altitude (McLean [1997]).

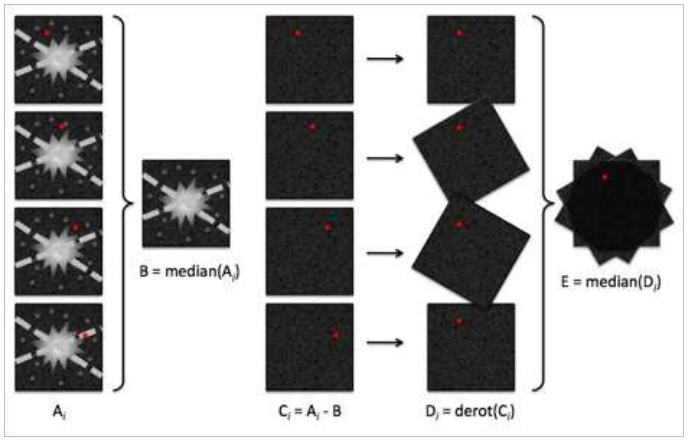

Figure 4.12: Representation of the ADI method, with the red dot indicating the position of a possible planet. Credits: MPIA (http://web.archive.org/web/20150915005746/http://www.mpia.de/homes/thalmann/adi.htm).

4.3.2 Spectral Differential Imaging

The spectral differential imaging (SDI; Racine et al. [1999]) technique exploits the fact that the speckle pattern, being a diffraction-related phenomenon, scales with wavelength, whereas real astrophysical sources such as planets remain fixed in position within the field of view regardless of the wavelength. This method can be applied when observations at multiple wavelengths are acquired simultaneously. Such images are typically acquired using so-called Integral Field Spectrographs (IFSs), which, through a lenslet-based design, generate images

composed of spectral pixels, each carrying spectral information corresponding to a specific location in the image plane (e.g. Figure 4.13).

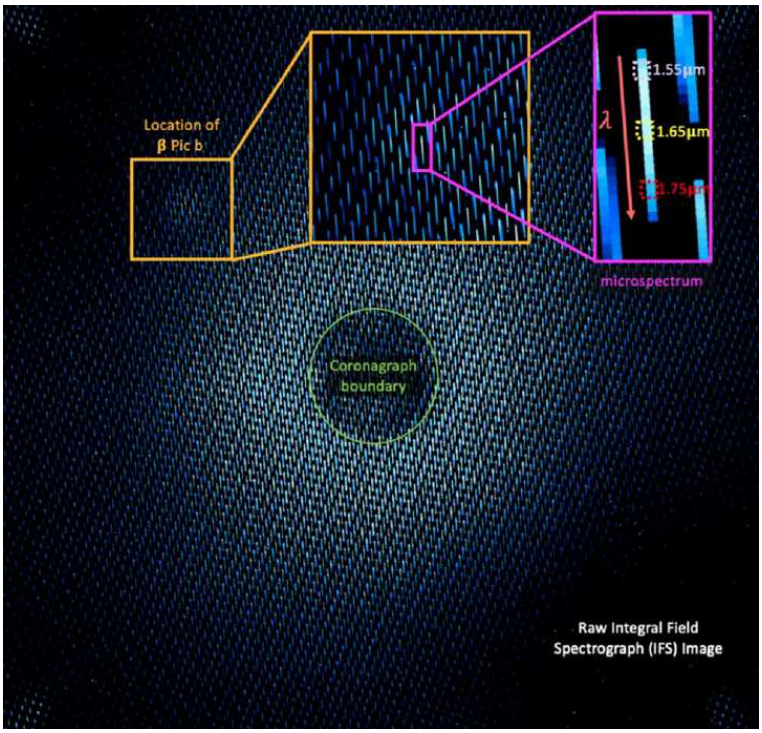

Figure 4.13: Schematic visualization of the lenslet pattern in an IFS, with a spectral pixel highlighted. The image shows a raw H-band frame of the star β Pictoris taken with the Gemini Planet Imager (GPI); its planetary companion, β Pictoris b, is visible in the upper left of the stellar PSF. Image adapted from Follette [2023].

Each image is rescaled to a common reference wavelength, allowing the construction of a reference PSF that includes only the speckle pattern and excludes any planetary signal. This reference PSF is then subtracted from each image to suppress the speckles. Finally, the images are rescaled back to their original wavelengths, realigning the planetary signals across the sequence. As with ADI, SDI also introduces a degree of self-subtraction, which must be carefully modeled and corrected to recover the true planetary signal. More sophisticated approaches combine ADI and SDI techniques, commonly referred to as ASDI (Angular and Spectral Differential Imaging), to simultaneously exploit both angular and spectral diversity. This combined strategy enables the construction of reference images in which real astrophysical sources have shifted sufficiently, either due to field rotation or spectral rescaling, to avoid being preserved in the reference PSF. As a result, the quasi-static speckle pattern can be more effec-

tively removed. A schematic illustration of the SDI method is shown in Figure 4.14. This technique also enables the retrieval of spectral information from the imaged objects. In particular, it allows to distinguish a flat spectrum, characterized by approximately constant flux across all wavelengths, from a spectrum exhibiting strong absorption in one of the channels, which will manifest as varying peak intensities at different wavelengths.

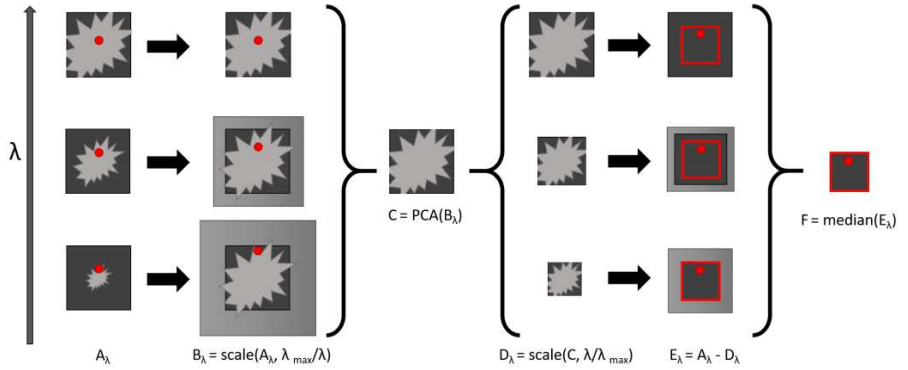

Figure 4.14: Graphical representation of the SDI technique, with the red dot indicating the position of a possible planet. Image taken from Kiefer et al. [2021].

4.4 Post-processing Algorithms

The differential imaging techniques described in the previous section are implemented through various algorithms aimed at subtracting the stellar PSF along with the speckle pattern. One such algorithm, which will be described in detail in the following, is based on the application of principal component analysis (PCA; Pearson [1901]), and it is the one used in the data analysis presented in Chapter 5.

4.4.1 PCA

The aim of principal component analysis is to identify the principal components within a dataset, allowing for a potential reduction in dimensionality while retaining most of the relevant information. Conceptually, PCA can be applied to a dataset by following the following steps.

1. The mean is subtracted from each dimension of the dataset, and each dimension is then divided by its standard deviation, resulting in a dataset with zero mean and standard deviation equal to one. This procedure is carried out on a two-dimensional array that contains, along one dimension, all the pixels of a single image, and along the other, all the images.

2. The second step involves the calculation of the covariance matrix between the different dimensions, along with its eigenvectors and eigenvalues.

3. The principal component of the dataset is identified as the eigenvector with the largest eigenvalue. To obtain the components in order of significance, the eigenvectors should be sorted by their corresponding eigenvalues, from largest to smallest.

4. The final step consists in selecting the principal components to retain for the reconstruction of the reference PSF, which will then be subtracted from the science images.

In Figure 4.15 is represented a visualization of the PCA concept, showing graphically how it works in the case of a three-dimensional dataset. To describe the position of any data point in this example dataset, the x, y and z coordinates can be provided. However, a good approximation can be obtained specifying a single coordinate along a vector that describes as much of the variation of the data as possible, and this coordinate is the so-called first principal component. If that point's location along an additional vector defined to be both orthogonal to the first principal component, and pointing along the (orthogonal) direction describing the greatest amount of additional variance in the data is also specified, this second principal component, together with the first, would provide an even better estimate of the point's location using only two (rather than the original three) coordinates.

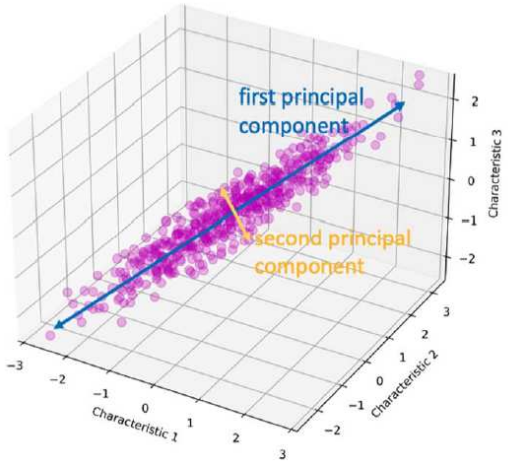

Figure 4.15: Graphical representation of the PCA concept. The first principal component of the example dataset is depicted here in blue, while the second principal component is in yellow. Image taken from Follette [2023].

This procedure can be applied to remove speckle noise in direct imaging data. In fact, the speckle pattern dominates over the signal from real astrophysical

sources, and as a result the first principal components of the science-reduced images are often largely influenced by speckle noise. By selecting a number of principal components from the dataset and subtracting them from the original images, most of the speckle noise can be removed. This enhances the detectability of faint signals associated with true companions. The selection of the number of principal components to subtract should be made carefully: the larger the number of principal components removed, the better the noise subtraction but, on the other hand, the larger the self-subtraction of the signal from faint companion objects. Another important consideration is that the speckle pattern is only quasi-static on timescales of a few minutes. If the pattern was perfectly static throughout the entire observing sequence, a simple median subtraction would be enough to eliminate it perfectly. Since this is not the case, only a limited number of principal components is used to reconstruct and subtract the speckle contribution.

To extract the principal components from the science-reduced images, an algorithm based on the singular value decomposition (SVD) is often used. First of all, the data need to be organized in a single matrix (denoted as $\mathbf{M}$) with dimensions $L_{px}^2 \times (N_{frames} \cdot N_\lambda)$, where L_{px}^2 is the area (expressed in pixels) of the image, N_{frames} is the total number of frames, and N_λ is the total number of wavelengths. In this matrix, each column corresponds to a different image, organized pixel by pixel, while the rows represent the same pixels across different images. Each column is then normalized by subtracting the mean and setting the standard deviation to one. Then, $\mathbf{M}$ is decomposed as $\mathbf{M} = \mathbf{U}\mathbf{\Sigma}\mathbf{V}^T$, where $\mathbf{U}$ is an orthogonal matrix containing the principal components of $\mathbf{M}$, $\mathbf{\Sigma}$ is a diagonal matrix with the singular values of $\mathbf{M}$, and $\mathbf{V}$ is an orthogonal matrix containing the projection coefficients (the modes) for each frame. Using the selected number of modes, the original image is reconstructed as a linear combination of the selected modes. The first row vectors of $\mathbf{V}^T$ represent the modes, and the coefficients c_i^k are the elements of the matrix $\mathbf{C} = \mathbf{U} \cdot \mathbf{\Sigma}$. The reconstructed image is then subtracted from the original image, after multiplying it by the original standard deviation and adding the mean (to denormalize). The result is an image with the selected principal modes removed. The way this procedure is applied in our work is described in Section 5.1.4.

Another algorithm is based on the application of the PCA through the Karhunen-Loève (KL) transform applied to a library of reference PSF images. This approach was first introduced in Soummer et al. [2012], together with the development of the Karhunen-Loève image projection (KLIP) algorithm. Once the target images and reference images are partitioned and their average subtracted to ensure a zero mean, the KL transform is applied to the reference PSF library. After selecting the number of modes to retain, the best estimate of the PSF to be subtracted is computed by projecting the science image onto the KL basis. The number of basis vectors corresponds to the number of retained modes. The final image is then obtained by subtracting the reconstructed PSF from the original science image.

4.5 Instrumentation

The growing interest in exoplanetary science, along with the development of HCI techniques, has led to the design and construction of numerous instruments that are either fully or partially dedicated to this type of observation. In this section, some of the currently active and future instruments will be presented, with particular focus on SPHERE, the instrument used in this work, which will be described in greater detail.

- **GPI** The Gemini Planet Imager (GPI; Macintosh et al. [2014]) was installed on the Gemini South telescope, which has an aperture of 8.2 meters. It operated in the NIR, covering a wavelength range from 1.0 to 2.5 μm, divided into five spectral bands. GPI featured an IFS with a spectral resolution between 30 and 70 and a field of view of $2.78'' \times 2.78''$. It also offered dual-channel polarimetric capabilities in the Y, J, H, and K bands. The instrument was equipped with an ExAO system, including a deformable mirror with 4196 actuators and a wavefront sensor operating at frequencies between 1 and 2 kHz. Decommissioned in 2020, GPI is currently undergoing an upgrade to GPI 2.0 (Chilcote et al. [2020]), installed on the Gemini North telescope, with scientific operations expected to resume in 2026.

- **ERIS** ERIS (Enhanced Resolution Imager and Spectrograph; Davies et al. [2023]) is an imager and spectrograph installed at the Very Large Telescope (VLT), which achieved first light in 2022. It consists of two subsystems. The first, NIX (Pearson et al. [2016]), is an imager operating in the 1–5 μm wavelength range and includes a long-slit spectroscopic (LSS) mode in the L-band with a spectral resolution of $R \sim 450$. The second subsystem is SPIFFIER, an IFS operating between 1 and 2.5 μm, offering two spectral resolutions: $R \sim 5\,000$ over the full band and $R \sim 10\,000$ over half a band. ERIS is equipped with an AO system based on the Adaptive Optics Facility (AOF) of the VLT Unit Telescope 4 (UT4).

- **SHARK** SHARK (System for coronagraphy with High order Adaptive optics from R to K band) is one of the instruments installed on the Large Binocular Telescope (LBT), which consists of two 8-meter apertures. It comprises two subsystems, able to operate simultaneously: SHARK-VIS, operating in the visible range (0.4–0.9 μm; Mattioli et al. [2018]), and SHARK-NIR, operating in the near-infrared (0.96–1.7 μm; Farinato et al. [2022]). SHARK-VIS supports high-cadence imaging between 60 Hz and 1 kHz and is capable of achieving contrasts on the order of 10^{-5} at angular separations smaller than 100 mas around bright stars. SHARK-NIR is equipped with an ExAO system and achieves a Strehl ratio of approximately 70% (for stars as faint as $R \sim 13$ mag) in its working bands (Y, J, and H), thanks to the SOUL (Single conjugated Adaptive Optics Upgrade for LBT; Pinna et al. [2021]) system. Available observing modes include classical imaging with various coronagraph types (Gaussian, shaped pupil,

and 4QPM), dual-band imaging, and LSS with both low ($R \sim 100$) and medium ($R \sim 700$) spectral resolutions. SHARK-NIR can achieve contrasts on the order of $\sim 10^{-5}$ to 10^{-6} at angular separations of 300–500 mas.

- **ELT** The Extremely Large Telescope (ELT[1]) is a next-generation 39-meter telescope currently under construction at Cerro Armazones, Chile. The first generation instruments of the ELT will comprise several high-contrast imagers and spectrographs. Among them, there are METIS (Mid-infrared ELT Imager and Spectrograph) and HARMONI (High Angular Resolution Monolithic Optical and Near-infrared Integral field spectrograph). METIS will work with a set of four different focal planes, organized in three different scientific subsystems: the imager, the spectrograph and a dedicate AO system (SCAO). The imager will operate between 3 and 13.5 μm, while the spectrograph (an IFS with $R \sim 100\,000$), will cover the 3-5 μm range. HARMONI will work between 0.47 and 2.45 μm, with a resolution between 3 000 and 18 000. It is compatible with two different AO modes, SCAO (using a single, bright reference star), and LTAO (laser tomography AO, which combines laser guide stars with fainter natural stars). Thanks to its spatial scale variable between 4 and 60 mas, HARMONI offers a variety of fields of view and spatial resolutions, making it a very versatile instrument.

Figure 4.16 presents the contrast performances, measured and predicted, of several high-contrast imaging instruments in several wavelengths regimes. To provide context, detected exoplanets (red squares) and simulated companions (orange diamonds) are overplotted, along with planets expected to be seen in reflected light (grey triangles).

[1] https://elt.eso.org/

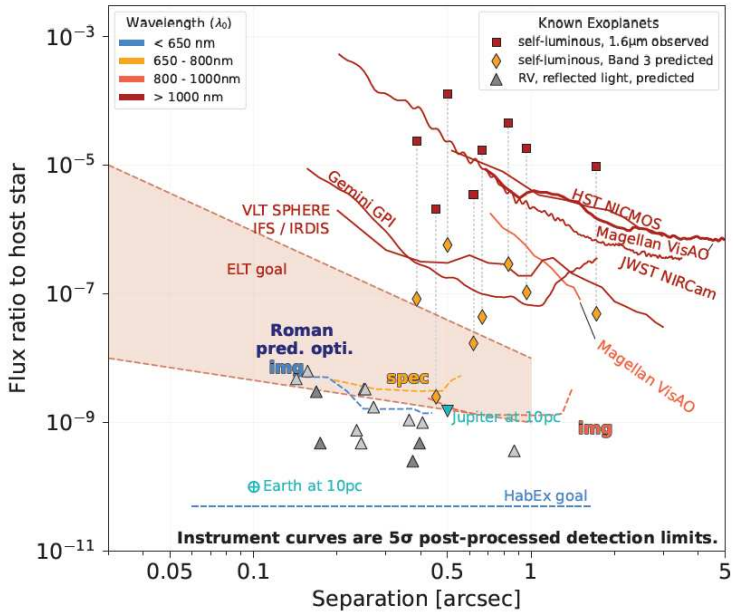

Figure 4.16: 5σ post-processed contrast curves of several ground- and space-based high-contrast imagers, including the scientific goals of upcoming instruments. Code by V. Bailey and S. Hildebrand Rafels (https://github.com/nasavbailey/DI-flux-ratio-plot), image taken from Claudi and Mesa [2025].

4.5.1 SPHERE

SPHERE (Spectro-Polarimetric High-contrast Imager for Exoplanet Research; Beuzit et al. [2019]) is a high-contrast imaging instrument installed on the UT3 telescope of the VLT at Paranal Observatory. Its primary scientific goals include the direct imaging, low-resolution spectroscopy, and polarimetric characterization of exoplanets. The instrument is specifically designed to deliver high image quality and contrast performance in both the visible and near-infrared domains. SPHERE consists of four main components: a common path system, comprising the ExAO system and the coronagraphs, collectively referred to as the Common Path and Infrastructure (CPI); the InfraRed Dual-band Imager and Spectrograph (IRDIS; Dohlen et al. [2008]); the Integral Field Spectrograph (IFS; Claudi et al. [2008]); and the Zurich IMaging POLarimeter (ZIMPOL; Schmid et al. [2018]). A conceptual overview of the SPHERE instrument is provided in Figure 4.17.

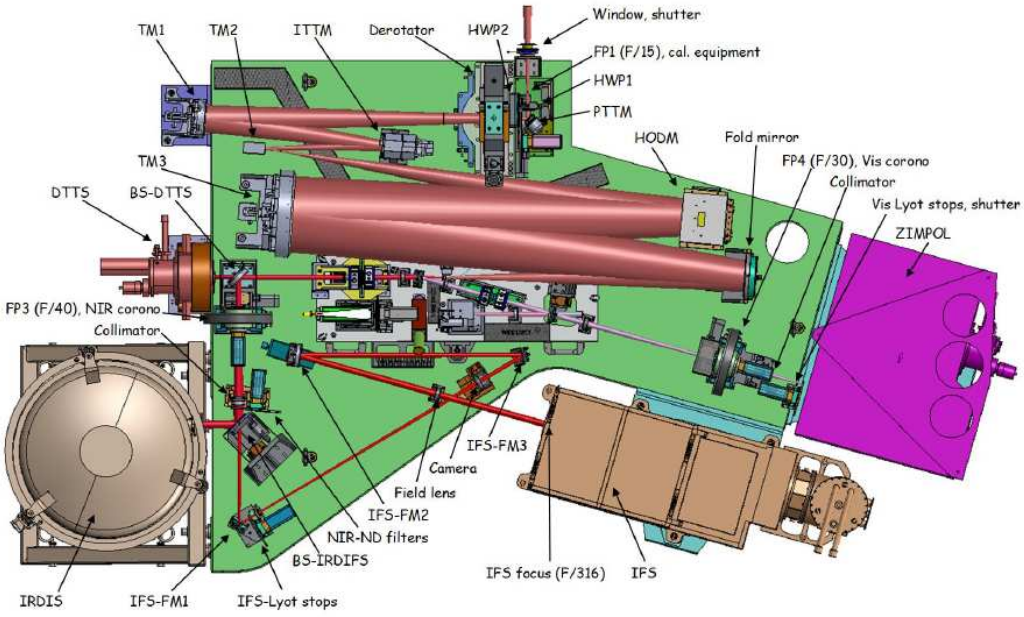

Figure 4.17: Top view of the SPHERE optical bench, with its main components labeled. The incoming light from the telescope enters from the top (Beuzit et al. [2019]).

The incoming light is split by a dichroic beam splitter into visible and infrared components before reaching the scientific instruments. A subsequent beam splitter divides the infrared light between the IRDIS dual-band imaging camera and the IFS spectrograph. A dedicated mirror enables IRDIS-only observations, while two additional dichroic splitters allow for simultaneous observations with both IFS and IRDIS.
ZIMPOL is the visible-light instrument of SPHERE, operating over a spectral range from 510 to 900 nm and offering observational modes including polarimetric differential imaging, imaging, spectral differential imaging, and angular differential imaging. Its main science goals are to detect reflected light from older exoplanets, which are more difficult to observe in their thermal emission, and to study extended structures such as circumstellar and debris disks.
The IFS, as its name suggests, is an integral field spectrograph optimized for high-contrast observations in the immediate vicinity of the host star (0.15″-0.7″), with an approximately square field of view measuring $\sim 1.73''$ per side, exploiting both ADI and SDI techniques. The IFS is designed to operate simultaneously with IRDIS and supports two observing modes: the `IRDIFS` mode, which covers the Y and J bands (0.95–1.35 μm) with a spectral resolution of $R \sim 50$, and the `IRDIFS_EXT` mode, which extends the coverage from the Y to the H bands (0.95–1.65 μm) with a spectral resolution of $R \sim 30$. The Y–H mode delivers improved contrast and better performance at smaller separations

compared to the Y–J mode. However, the use of the H band for IFS implies that only the K band is available for IRDIS, which results in a reduction of performance for the latter. IFS is based on a lenslet integral field unit (IFU), located at its focal plane. Each lenslet acts like a slit and the light from each lenslet is dispersed into a spectrum on the detector, with the lenslet centers being separated by $0.01225''$ from each other. The IFS, as shown in Figure 4.18, is composed of several main sub-systems:

- the IFU;
- the collimator;
- a filter wheel with several neutral density filters limiting the received flux;
- a prism slide to select between the two different prisms (corresponding to the two observing modes);
- a camera;
- a detector working in the wavelength range 0.95-2.32 μm;
- an internal calibration arm constituted by several light sources feeding an integrating sphere;
- a cryostat housing the IR detector.

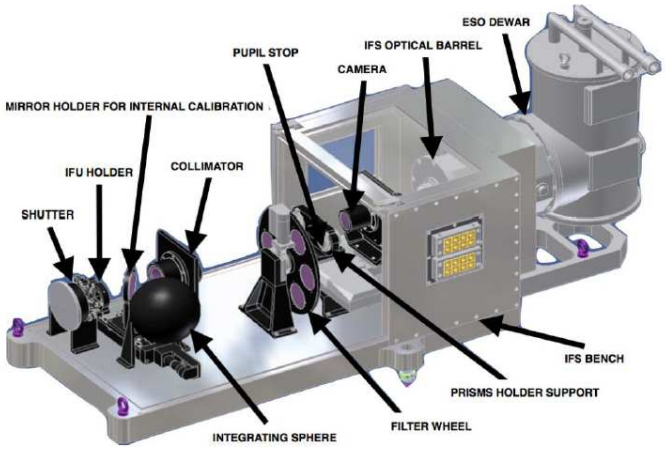

Figure 4.18: Schematic view of the IFS instrument (Claudi et al. [2008]).

On-sky observations showed that IFS is able to achieve 5σ contrasts better than 10^{-6} for bright stars ($J < 6$ mag) observed under median or good conditions. Moreover, IFS is also capable of extracting low-resolution spectra of the imaged companions, thanks to its 39 spectral channels over which the wavelength coverage is divided.

The IRDIS instrument provides imaging, spectroscopy, and polarimetry through two parallel channels, each with a circular field of view of approximately 5″ in radius, and covering a wavelength range from 0.95 to 2.4 μm. It operates in four observing modes: dual-band imaging (DBI; Vigan et al. [2010]), dual-polarimetric imaging (DPI; Langlois et al. [2010]), long-slit spectroscopy (LSS; Vigan et al. [2008]), and classical imaging (CI). Although primarily designed for exoplanet detection, IRDIS is also well suited for other scientific objectives, such as the study of circumstellar disks and close stellar environments, thanks to its versatility. The optical design of IRDIS includes a beam-splitting plate that divides the incoming light into two parallel beams, one for each channel. Three filter wheels are used for the LSS and CI modes, while an additional wheel holds the DBI filter pairs and polarizers. Finally, the two beams are projected onto the detector, as illustrated in Figure 4.19.

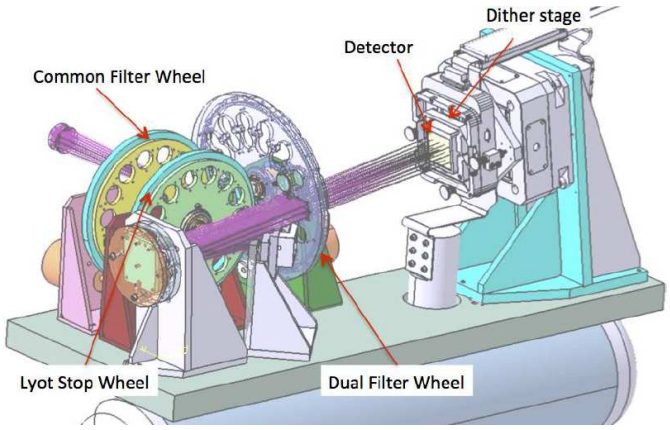

Figure 4.19: Schematic view of the IRDIS instrument (Dohlen et al. [2008]).

The main observing mode of IRDIS is DBI, which is optimized for the detection and characterization of planetary companions down to Jupiter mass around nearby young stars. Unlike the IFS, IRDIS can also operate independently, taking advantage of its full wavelength coverage. When used in parallel with IFS, two observing modes are available, as summarized in Table 4.2, which lists the spectral bands associated with each mode, the corresponding IRDIS narrow-band filters, and the optimized coronagraph configurations. In both of these modes, IRDIS is operating in DBI mode. IRDIS provides lower contrast than IFS, typically by 1 to 2 orders of magnitude but, thanks to its larger field of view, it is well suited for detecting faint companions at wider separations from the star, effectively probing the outer regions of planetary systems.
SPHERE is equipped with an ExAO system called SAXO (SPHERE extreme AO system), which includes a deformable mirror with 1377 actuators and a WFS based on an EMCCD detector capable of operating at frequencies up to 1380 Hz, with an equivalent readout noise of less than 0.1 e^-. SAXO enables high-performance correction, routinely achieving Strehl ratios of approximately

Observing mode	IRDIFS	IRDIFS_EXT
IFS	Y-J bands	Y-H bands
IRDIS	$H2$ ($\lambda = 1.587\ \mu m$)	$K1$ ($\lambda = 2.110\ \mu m$)
	$H3$ ($\lambda = 1.667\ \mu m$)	$K2$ ($\lambda = 2.251\ \mu m$)
Coronagraph	APO1/ALC2	APO1/ALC3

Table 4.2: Observing modes available when IFS and IRDIS operate in parallel, including their corresponding spectral bands and optimized coronagraph configurations.

90% in the H-band under high-flux conditions and for median seeing conditions ($0.8'' - 1.2''$), as illustrated in Figure 4.20.

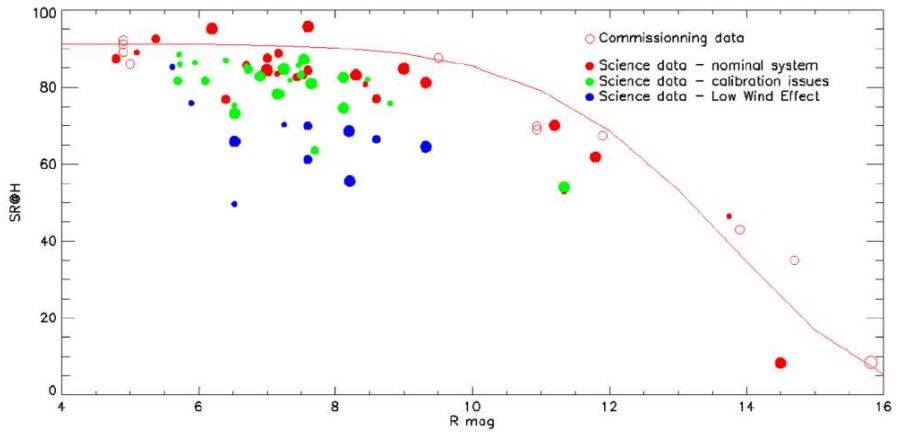

Figure 4.20: Strehl ratio in H-band, measured on-sky during commissioning and SPHERE science verification. Nominal performances are shown as red circles, while data points corresponding to different problematic regimes are indicated in green and blue circles. The expected nominal trend is overplotted as a solid red line (Beuzit et al. [2019]).

SPHERE offers several types of coronagraphs designed to cover a broad wavelength range and deliver high-contrast performance at small angular separations. The apodizers and focal plane masks are located within the CPI, with separate channels for the NIR and visible. The NIR channel includes two coronagraph types: the apodized-pupil Lyot coronagraph (APLC) and the half-wave four-quadrant phase mask (HW-4QPM). The APLC design integrates a pupil-plane apodizer (APO), a focal-plane mask (ALC), and a Lyot stop. Six APLC configurations are available, combining two apodizers and three focal masks. APO1 and APO2 feature IWA of $2\lambda/D$ and $2.6\lambda/D$, with transmission values of 63%

and 48% relative to the VLT pupil, respectively. The ALC1, ALC2, and ALC3 focal masks have diameters of 145, 185, and 240 mas. Each configuration has a defined upper wavelength limit, making them optimal for specific spectral bands. In the visible channel, ZIMPOL employs classical Lyot masks and two 4QPMs designed for achieving very small IWAs. The different coronagraph configurations were tested during the commissioning phase under various observing conditions, achieving contrast levels ranging from 10^{-3} to 10^{-5} in the H and K bands.

Operational since 2015, SPHERE has achieved significant results, detecting and characterizing numerous exoplanets (e.g. Figure 4.21). One of the largest surveys carried out with SPHERE is SHINE (SpHere INfrared survey for Exoplanets; Chauvin et al. [2017a]), which ran from 2015 to 2021 and observed 150 stars over more than 200 nights. The detection capabilities and final outcomes of the survey are presented in Chomez et al. [2025]. Designed to discover and characterize new exoplanets and brown dwarfs, the survey led to the detection of two exoplanets, HIP 65426 b (Chauvin et al. [2017b]) and PDS 70 b (Keppler et al. [2018]), and one brown dwarf, HIP 64892 b (Cheetham et al. [2018]). The nature of 1220 companion candidates, detected around 133 stars, remains unconfirmed due to incomplete follow-up observations.

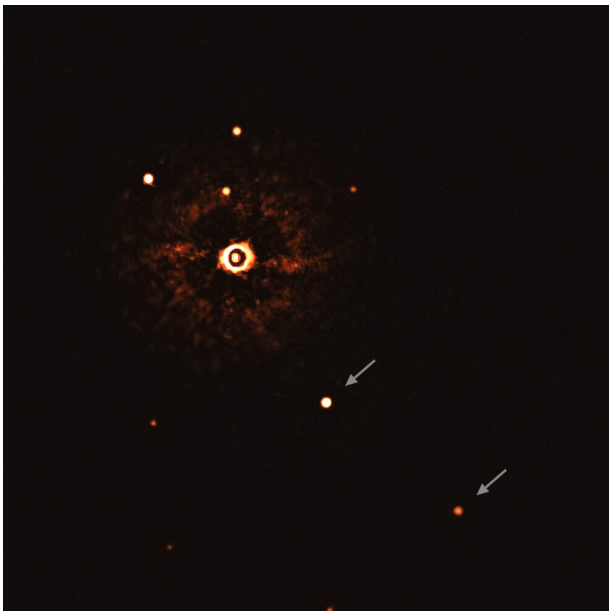

Figure 4.21: SPHERE image of the first directly imaged multi-planet exoplanetary system, orbiting the star TYC 8998-760-1 (Bohn et al. [2020]).

Chapter 5

TOI-201

All truths are easy to understand once they are discovered; the point is to discover them.
– G. Galilei

TOI-201 (also known as HD 39474 and HIP 27515), the target of our study, is a young F6V-type star whose stellar parameters are reported in Table 5.1. The presence of a planet orbiting this star was first confirmed by Hobson et al. [2021], where the authors validated the candidate planet TOI-201.01 (hereafter referred to as TOI-201 b), initially detected by TESS. As reported in this study, TOI-201 b has a radius of $1.008^{+0.012}_{-0.015}$ R_J and orbits its host star with a period of 52.97818 ± 0.00004 days. The confirmation of the planetary nature of the TESS candidate was made possible by the availability of radial velocity measurements collected with HARPS, FEROS, CORALIE, and MINERVA-Australis (see Section 5.2.2 for a detailed description of the RV data used in Hobson et al. [2021]). These data enabled a precise estimation of the planet's mass and semi-major axis, which are respectively $0.42^{+0.05}_{-0.03}$ M_J and $0.30^{+0.02}_{-0.03}$ AU, thus classifying TOI-201 b as a warm Jupiter.
In addition to TOI-201 b, another planetary candidate, TOI-201.02, is listed in the TESS database but still remains unconfirmed. This candidate, catalogued in the ExoFOP-TESS archive with an orbital period of 5.84924 ± 0.00004 days, has an estimated mass of $M \sim 6.38 M_\oplus$, as derived from the mass-radius relations detailed in Otegi et al. [2020]. This corresponds to an expected RV semi-amplitude of $K \sim 1.88$ m/s, which is significantly smaller than the median error of the RV measurements used in Hobson et al. [2021], $\sigma_m = 10.55$ m/s. Combined with the lack of dense RV sampling necessary to detect a planet at such close separation from its host star, this renders TOI-201.02 undetectable with the available data, and its presence therefore remains unconfirmed.

Parameter	Value	Reference
Names	TOI-201, HD 39474, HIP 27515	
π (mas)	8.914 ± 0.014	Gaia EDR3
T (mag)	8.5822 ± 0.006	TESS
B (mag)	10.104 ± 0.055	APASS
V (mag)	9.715 ± 0.079	APASS
J (mag)	8.103 ± 0.029	2MASS
H (mag)	7.923 ± 0.036	2MASS
K (mag)	7.846 ± 0.024	2MASS
G (mag)	8.94929 ± 0.00028	Gaia EDR3
T_{eff} (K)	6394 ± 75	Hobson et al. [2021]
Spectral type	F6V	PM13
Fe/H (dex)	0.240 ± 0.036	Hobson et al. [2021]
$\log g$ (dex)	4.318 ± 0.014	Hobson et al. [2021]
$v \sin i$ (km s^{-1})	9.52 ± 0.28	Hobson et al. [2021]
$R_\star$ ($R_\odot$)	1.317 ± 0.011	Hobson et al. [2021]
$M_\star$ ($M_\odot$)	1.316 ± 0.027	Hobson et al. [2021]
$L_\star$ ($L_\odot$)	2.6 ± 0.1	Hobson et al. [2021]
$\rho_\star$ (g cm^{-3})	0.81 ± 0.03	Hobson et al. [2021]
Age (Gyr)	$0.87^{+0.46}_{-0.49}$	Hobson et al. [2021]

Table 5.1: Stellar parameters of TOI-201. Gaia EDR3: Gaia Early Data Release 3 (Gaia Collaboration et al. [2021]); TESS: TESS Input Catalog (Stassun et al. [2019]); APASS: AAVSO Photometric All-Sky Survey (Munari et al. [2014]); 2MASS: Two-Micron All Sky Survey (Skrutskie et al. [2006]); PM13: Pecaut and Mamajek [2013].

TOI-201 is known to be an accelerating star, exhibiting a significant proper motion anomaly (PMa), first reported in the catalogue by Kervella et al. [2019] and later updated by Kervella et al. [2022]. The PMa values, presented in Table 5.2, are derived from the comparison of the proper motion measurements of TOI-201 as recorded in the Hipparcos catalogue (Perryman et al. [1997]) and the Gaia DR3 catalogue (Gaia Collaboration et al. [2023]). Moreover, the Signal-to-Noise ratio of the PMa values for the star derived from Gaia DR3 data is notably high, reaching 5.85. As this value exceeds the traditional threshold of 3, it provides strong evidence for the presence of a companion responsible for the observed anomaly. Moreover, the reported RUWE value for TOI-201 is 1.098. Since this lies well below the commonly adopted threshold of 1.4, it provides no indication of binarity, suggesting that no massive companion is located in close proximity to the star.

	$\Delta\mu_\alpha$ **(mas/yr)**	$\Delta\mu_\delta$ **(mas/yr)**	**SNR**
Hipparcos	0.901 ± 0.821	0.199 ± 0.960	0.73
Gaia DR3	-0.179 ± 0.036	-0.235 ± 0.035	5.85

Table 5.2: Proper motion anomaly values and associated SNR for TOI-201 from Hipparcos (epoch 1991.25) and Gaia DR3 (epoch 2016.0) (Kervella et al. [2022]).

However, neither the confirmed planet nor the candidate can account for the observed proper motion anomaly of TOI-201. Figure 5.1 shows the companion mass compatible with the observed PMa signal as a function of its orbital separation from the star, measured at the Gaia EDR3 epoch. The companion mass is calculated from the PMa values following the procedure outlined in Section 3.3, with further details provided in Kervella et al. [2019]. The figure also includes the position of TOI-201 b, clearly illustrating why it cannot be the source of the detected PMa. At its orbital distance, an object capable of generating the observed anomaly would need to have a mass of at least $\sim 200\,M_J$, whereas TOI-201 b has a mass of only $\sim 0.4\,M_J$.

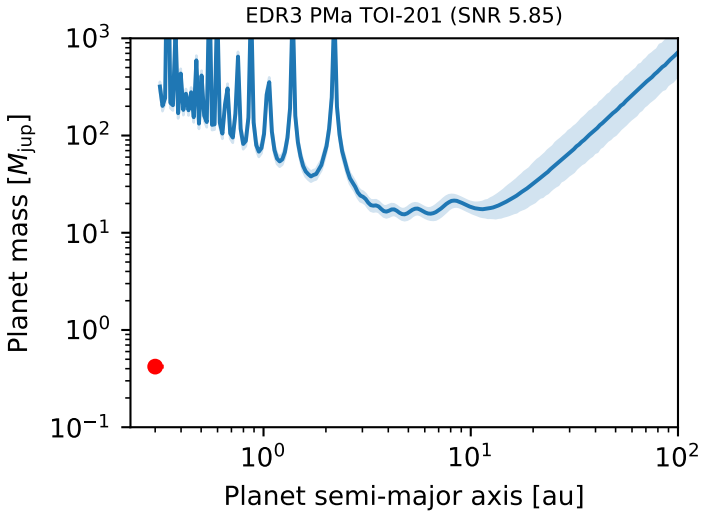

Figure 5.1: Proper motion anomaly results for TOI-201. The blue line shows the PMa-compatible companion masses as a function of orbital separations, and the shaded region corresponds to the 1-σ uncertainty range. The red circle represents the position of TOI-201 b on the parameter space, with error bars too small to be seen at this scale.

This discrepancy suggests the presence of an as-yet undiscovered companion in the brown dwarf regime, with a mass around $\sim 18 - 19\,M_J$, for orbital separa-

tions between approximately 3 and 20 AU, while at larger separations the PMa signal is compatible with the presence of a more massive object, towards the stellar regime. This makes TOI-201 a particularly interesting target for further study. To investigate whether this object can be directly detected and confirm its presence, a reduction of the available data collected from VLT/SPHERE was performed.

5.1 SPHERE data reduction

5.1.1 Datasets

TOI-201 was observed by SPHERE at three different epochs: October 14, 2023, November 19, 2023 and December 2, 2023, with all the observations conducted in the `IRDIFS_EXT` observing mode (see Section 4.5.1 for more details). The October 14 observation consisted of 80 scientific frames, each with an exposure time of 32 seconds, leading to a total integration time of 2560 s on the target. The total Field of View (FoV) rotation, quantified as the difference between the parallactic angle at the first and the last frame, was 22.55° for IRDIS and 15.44° for IFS. The November 19 observation consisted of 20 scientific frames, each with an exposure time of 32 seconds, leading to a total integration time of 640 s on the target. The total FoV rotation was 3.81° for both IRDIS and IFS. The December 2 observation consisted of 80 scientific frames, each with an exposure time of 32 seconds, leading to a total integration time of 2560 s on the target. The total FoV rotation was 30.95° for IRDIS and 30.96° for IFS. The details on the atmospheric conditions at the epochs of the three observations (seeing, coherence time τ_0 and the wind speed) are summarized in Table 5.3.

October 14, 2023 dataset			
Instrument	**Seeing (arcsec)**	τ_0 **(ms)**	**Wind speed (m/s)**
IFS	0.74 ± 0.02	6.00 ± 0.43	3.58 ± 0.64
IRDIS	0.71 ± 0.03	6.05 ± 0.32	3.85 ± 0.10
November 19, 2023 dataset			
IFS	0.64 ± 0.01	4.8 ± 0.1	7.25 ± 0.01
IRDIS	0.52 ± 0.04	5.90 ± 0.15	6.67 ± 0.08
December 2, 2023 dataset			
IFS	0.65 ± 0.04	5.10 ± 0.48	4.22 ± 0.06
IRDIS	0.60 ± 0.02	5.95 ± 0.33	4.30 ± 0.08

Table 5.3: Atmospheric parameters retrieved from the datasets acquired on different epochs.

In addition to the science frames, several calibration frames were acquired dur-

ing the observations. Among these, centering frames with satellite spots symmetrically disposed around the central star were obtained (star center frames). These frames allow for an accurate determination of the star's position behind the coronagraph, enabling a precise centering of the data (see Section 4.2 for more details). Figure 5.2 presents two examples of centering frames, one for IFS and one for IRDIS.

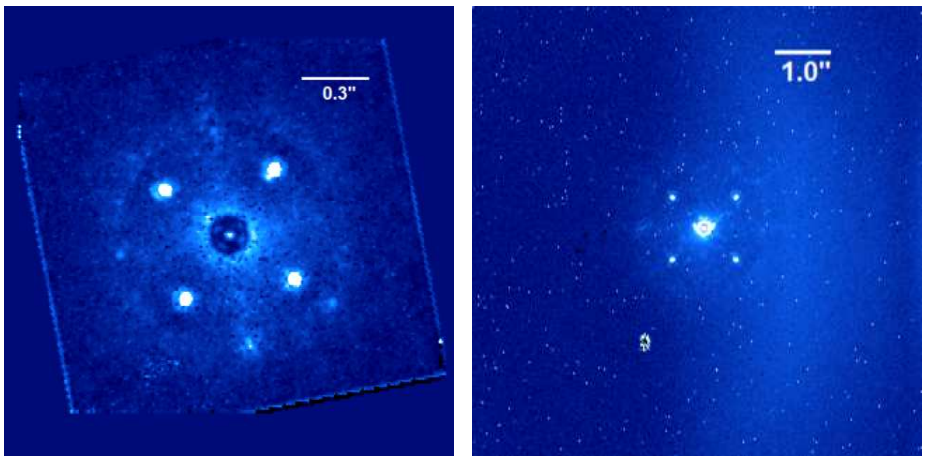

Figure 5.2: Centering frames acquired with IFS (*left*) and IRDIS (*right*), with the symmetric spots clearly visible around the star. The IRDIS image is a raw frame, while the IFS image has been reduced following the procedure outlined in section 5.1.3.

Furthermore, observations of the star taken outside the coronagraph were acquired with the purpose of flux calibration. These exposures, commonly referred to as flux calibration frames, were taken with shorter integration times compared to the science frames, and using a neutral density filter to avoid saturation. In particular, an ND1 filter was applied, which attenuates the stellar flux by a factor of 10. Figure 5.3 presents two examples of flux frames, one for IFS and one for IRDIS.
Multiple types of flat frames were obtained for both IRDIS and IFS. In the case of IRDIS, they differ mainly in their median count levels. For IFS, each flux frame is associated with a specific calibration lamp, resulting in a total of five different flat fields. Due to the instrumental characteristics of IFS, its calibration set also includes: a spectral position raw frame (specpos), used to obtain the position of the spectra produced by the lenslet array on the detector; a wavelength calibration raw frame, which provides the wavelength calibration for each individual spectrum; and an instrument flat (ifsflat), employed to generate the IFU flat field, accounting for the lenslet array's response to a uniform illumination. A set of dark frames with varying exposure times was also acquired. The reduction of the SPHERE data was carried out using the Data Reduction and Handling (DRH) pipeline (Pavlov et al. [2008]). This pipeline

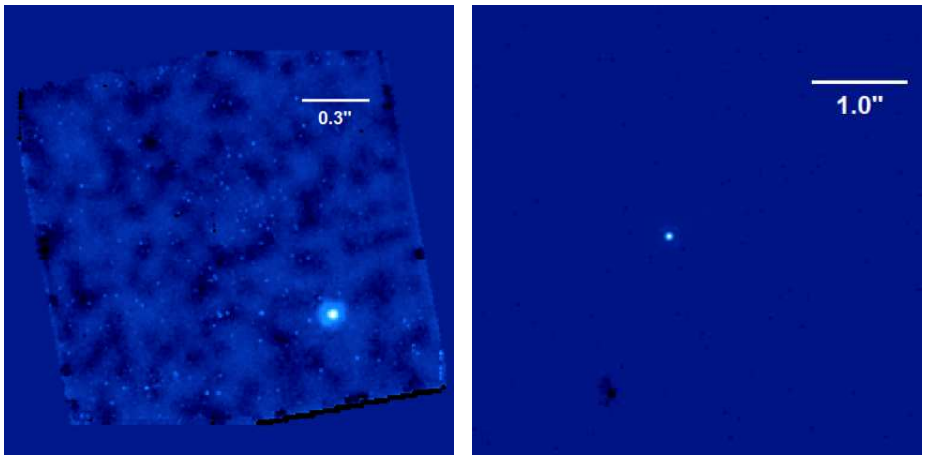

Figure 5.3: Flux frames acquired with IFS (*left*) and IRDIS (*right*). The star's PSF is off-axis, outside the coronagraph. The IRDIS image is a raw frame, while the IFS image has been reduced following the procedure outlined in section 5.1.3.

consists of procedures known as recipes, which are specifically designed for different types of data, suitable for both calibration and science data reduction, and are detailed in the following subsections. Each recipe is applied to a set of input FITS files. To run a recipe, the filenames must be listed along with their corresponding data categories in a set-of-frames (SOF) file, which is required when executing the recipe.

5.1.2 IRDIS data reduction

The first task in the reduction of IRDIS raw data is the creation of the master dark frame, along with a bad pixel map. This map identifies the pixels that significantly deviate from the mean of the image and are marked as bad. The same procedure is performed on both the science and flux raw frames, using their corresponding exposure times. The next step is the determination of the instrument flat field. This procedure requires as input a series of flat-field exposures with different median count levels, obtained by varying the intensity of the illuminating lamp. It also requires information on the dark frame, which is provided by supplying the bad pixel map associated with the science frames, as calculated in the previous step. The flat fielding procedure is applied separately to the IRDIS left and right spectral channels.
Before actually proceeding with the reduction of the science raw frames, it is fundamental to determine the field center, precisely defining the position of the star behind the coronagraph. The procedure, which makes use of the star center raw frame, is described in Section 4.2; additional details can be found in, among others, Sivaramakrishnan and Oppenheimer [2006]. With all the calibration steps completed, the reduction of the science raw frames can proceed.

First, the raw frames undergo dark subtraction, followed by division by the flat field. Then, the left and right subframes are extracted and, to recenter the images, a fast Fourier transform is applied. Before transforming the images, bad pixels are interpolated using an eight-neighbor pixel average. The output reduced datacubes have dimensions $1024 \times 1024 \times N_{frames}$, where the first two dimensions correspond to the spatial dimensions of each image (in pixels) and N_{frames} is the total number of frames. For each raw frame, reduced frames for both the right and the left channel are produced. An example of an IRDIS raw and reduced science frame is shown in Figure 5.4. The last step is the flux calibration, the purpose of which is to measure the unsaturated peak flux of the star by offsetting it from the coronagraph spot, in order to ensure accurate relative photometry, and thus contrast calibration.

5.1.3 IFS data reduction

The first step in the IFS data reduction process is the creation of the master dark frame. Similar to the IRDIS process, this procedure generates the master dark frame along with the associated bad pixel map for the detector. The master detector flat frame is then produced using input exposures acquired with different calibration lamps, each producing a different type of flat field. Since in these observations the IFS is operating in the Y, J, and H spectral bands, the calibration lamps employed include a broadband (white) lamp, along with four narrowband lamps centered at wavelengths of 1.02, 1.23, 1.30, and 1.55 μm.
The next task is to determine the positions of the spectra on the detector, associating the IFS spectra with the lenslets and linking each pixel to a corresponding wavelength. This step requires the raw specpos frame, acquired by illuminating the IFS with a broadband light source connected to an integrating sphere in the calibration arm. This first estimate is then refined with a precise wavelength calibration of each individual spectrum. The initial wavelength assignment to each pixel is refined using data obtained by illuminating the IFS with four laser light sources at wavelengths of 0.9877, 1.1237, 1.3094, and 1.5451 μm. Before reducing the science frames, it is necessary to create the IFU flat field to properly account for the response of all IFU lenslets under uniform illumination. The result is a table containing the flat field values for all lenslets.
At this stage, two corrections are applied to the raw science frames. The first is an improved bad pixel correction, which refines the preliminary estimation performed in the earlier steps. This procedure operates two corrections, here described.

1. The first correction applies only to the pixels marked as bad, which are read from the bad pixel map provided as input. For each bad pixel, the median is calculated within its column. Then, from the eight neighboring pixels, only those not marked as bad are selected, and their values are normalized relative to the median of the column they belong to. Finally, if at least one non-bad neighboring pixel is found, the value of the original bad pixel is replaced with the median of the normalized values of the good

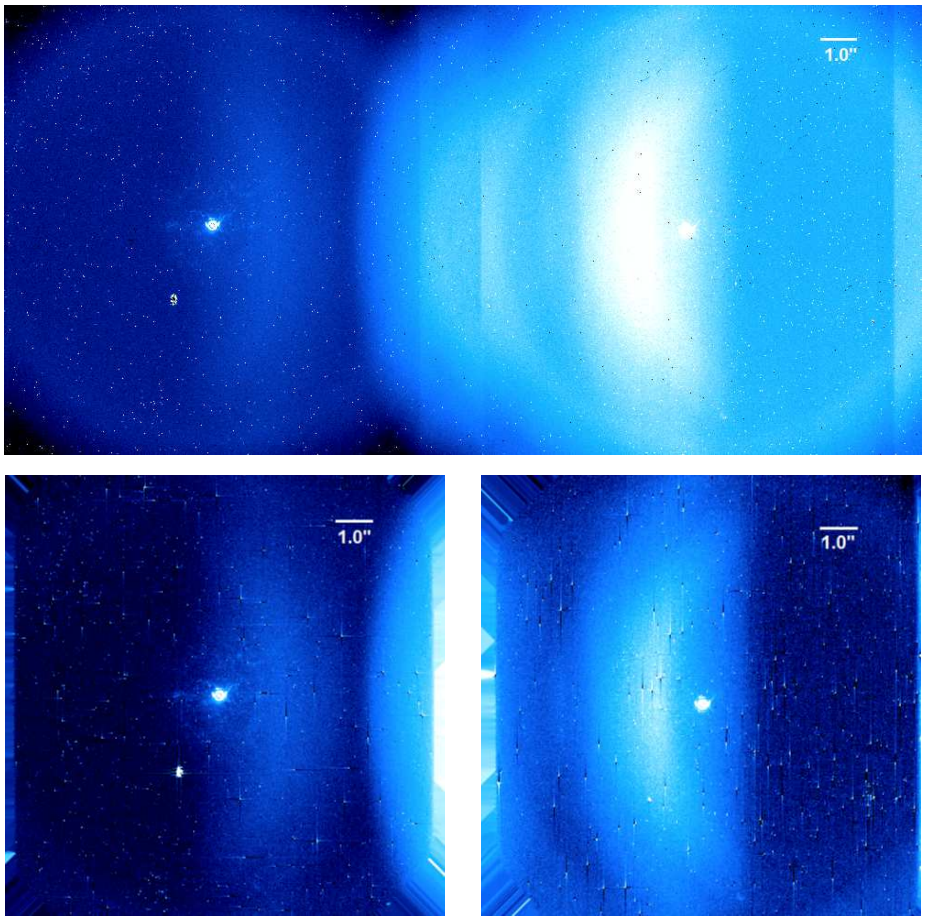

Figure 5.4: IRDIS science frames. *Top*: raw science frame, showing the K1 ($\lambda = 2.110\ \mu m$) and K2 ($\lambda = 2.251\ \mu m$) wavelength channels. *Bottom left and right*: the same science frame after reduction, with the left and right channels extracted separately.

neighboring pixels. If all eight neighboring pixels are marked as bad, all of them are included in the median calculation to replace the original bad pixel.

2. A second correction, applied to every pixel in the image (except for those on the borders), is necessary to correct for outliers and anomalies not detected in the initial bad pixel map. First, the median of each column in the image is calculated. Then, for every pixel, the values of its eight neighboring pixels are extracted and normalized based on the median of their respective columns, creating an unique median value. If the value of the central pixel is greater than five times the median of its neighbors and

exceeds a predefined threshold, its value will be replaced with the median of the neighbors.

The second correction addresses cross-talk, which is the effect where light collected by a lenslet diffuses into neighboring ones. To accurately model and mitigate this effect, two corrections are applied: a small-scale correction and a large-scale correction, both of which are described here.

1. The small-scale correction involves creating a correction matrix for each pixel in a window centered on the pixel to be corrected. This matrix models the cross-talk effect, accounting for the fact that the effect weakens as the distance from the central pixel increases, and includes a scale factor. The elements of this matrix are defined as:

$$M(k,j) = \frac{1}{1 + \left(\frac{r_{kj}}{b}\right)^3} , \tag{5.1.1}$$

   where r_{kj} is the distance between the pixel inside the window at which this element is calculated and the central pixel, and b is a parameter controlling the intensity of the effect. Once these matrix elements are computed, the correction is applied to every pixel in the image. The correction consists of subtracting from the original pixel the correction matrix element corresponding to a pixel in the window, multiplied by the intensity of that pixel, iterated for all pixels in the window. This approach is based on the model proposed by Antichi et al. [2009].

2. The large-scale correction, aimed at subtracting the wide-scale structures present in the images due to cross-talk, is divided into two parts: the computation of the large-scale effect and its subsequent subtraction. First, a correction for saturated pixels is applied by replacing the values of pixels exceeding a predefined threshold with the median intensity of the image. Next, the original image is divided into several blocks. For each block, a histogram of pixel intensities is generated. The most populated bin of each histogram is then selected, and the entire block is replaced with this dominant intensity value, producing an image composed of uniform blocks. This resulting image is subsequently smoothed to avoid sharp discontinuities and used as a model of the large-scale cross-talk effect, which is finally subtracted from the previously small-scale corrected image.

After these corrections, the science raw frames are finally reduced. First, the input data are corrected for large-scale systematics by constructing a super flat, which combines flat fields acquired with different calibration lamps. The resulting science-reduced data are stored as three-dimensional datacubes composed of uniformly spaced monochromatic planes. Each datacube has dimensions $291 \times 291 \times 39$, where the first two dimensions correspond to the spatial dimensions of each image (in pixels), and the third dimension represents the IFS spectral channels. Figure 5.5 shows the same science frame at different

stages of the reduction process. After the bad pixel correction, the clump located at the bottom left of the image, along with other outliers, appears significantly smoothed. Following the cross-talk correction, the effect of dispersed light between neighboring lenslets, visible as a halo covering the image, is largely removed. Finally, after the science reduction step, the image appears more uniform, as the imprint of the individual lenslets is no longer visible.

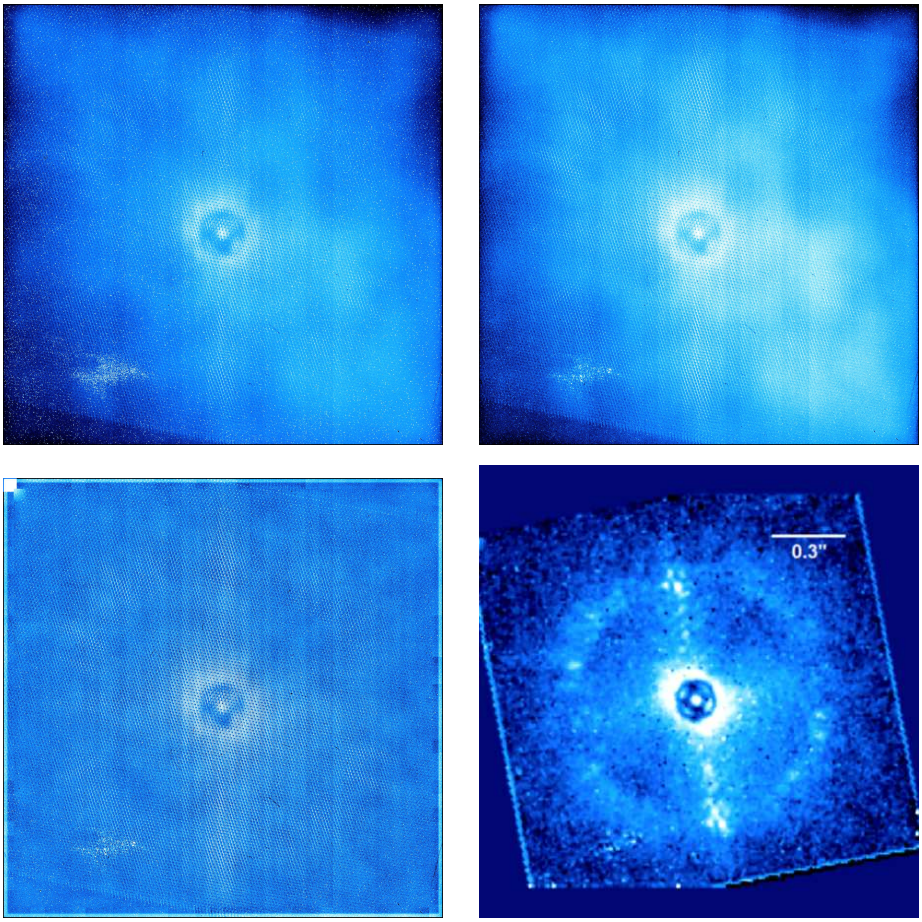

Figure 5.5: IFS images illustrating the reduction and correction procedure. *Upper left*: Raw science image. *Upper right*: Raw image after bad pixel correction. *Bottom left*: Image after bad pixel and cross-talk correction. *Bottom right*: Final science reduced image, with scale. The last image shows the 3^{rd} channel of IFS at $\lambda = 0.991\ \mu m$.

A similar procedure is applied in the following step, the star center determination. As in the science data reduction, the raw starcenter frame undergoes preliminary corrections for cross-talk and bad pixels before being processed. To

accurately determine the center of the stellar point spread function (PSF), this procedure provides a consistent and precise centering solution across all spectral channels. Starting from an initial guess of the center position, the distances between this guess and the centers of the four satellite spots are calculated, using as reference the image corresponding to the mean wavelength of the spectral range. These distances are then used to refine the estimate of the PSF center, as well as to associate each image with its corresponding wavelength.
The final step, flux calibration, closely follows the procedure used for IRDIS. In this case a low-resolution spectrum is produced through further processing, providing the center position along with the photon counts for the 39 wavelengths at which IFS operates, evenly spaced between 0.95 μm and 1.65 μm, covering the Y, J, and H spectral bands.

5.1.4 Post-processing

This section outlines the various post-processing techniques applied to the data reduction products obtained through the DRH pipeline. The procedures are very similar for both IRDIS and IFS instruments. Except for a few specific differences, which will be explicitly described, the post-processing steps will be presented in a unified manner without referring to the specific instrument in each step.
Before beginning the actual post-processing, some preliminary operations must be performed on the reduced science frames. First of all, each datacube resulting from the science reduction step must be centered, so that the star is located at the center of the image for each wavelength, using the previously determined star center positions. The datacube is then normalized by the exposure time of the science frames. The result is a four-dimensional datacube, with dimensions $L \times L \times N_{frames} \times N_\lambda$, where L is the length in pixels of one side of the image, N_{frames} is the total number of frames, and N_λ is the total number of wavelengths. This datacube contains all the normalized and centered images in a format suitable for further processing. An array containing the wavelengths associated with each instrument is also created. Then, based on the flux calibration data, a three-dimensional datacube of dimensions $64 \times 64 \times N_\lambda$ is created, containing an unsaturated PSF for each wavelength in a small window centered on the PSF (with dimensions 64×64 pixels). These images are normalized with respect to the exposure time of the flux frames and corrected for the spectral transmission of the filter used during the observations. This datacube represents the stellar PSF, which will also be used in subsequent analysis steps. Lastly, a correction is applied to the parallactic angle taking into account the True North angle in order to be able, in the subsequent steps, to align each frame with the North up and the East to the left
The presence of speckle patterns in the reduced science images significantly limits the achievable contrast, thereby reducing the capability to detect potential companions to the target star. In order to suppress speckle noise, a Principal Component Analysis (PCA) was performed on the four-dimensional datacube obtained from the previous step, following the procedure detailed in Section

4.4.1. In this specific situation, the PCA is applied implementing both the Angular Differential Imaging technique and the Spectral Differential Imaging technique (ASDI). The first step consists in rescaling all the images acquired at different wavelengths (2 for IRDIS, 39 for IFS). To achieve this, scale factors for each wavelength are calculated, taking as reference the wavelength associated with the eighteenth frame for IFS and the first frame for IRDIS, according to:

$$f(k) = \frac{\lambda_{ref}}{\lambda_k} \ , \ k = 1, \ldots, n \ , \tag{5.1.2}$$

with $n = 2$ for IRDIS and $n = 39$ for IFS, λ_{ref} is the reference wavelength and $f(k)$ the scale factor associated to the k-th wavelength. Then, a datacube is produced with all the images rescaled according to their respective wavelengths. The data are then organized into a matrix (denoted as $\mathbf{M}$) with dimensions $L_{px}^2 \times (N_{frames} \cdot N_\lambda)$, where L_{px}^2 is the area (expressed in pixels) of the image, N_{frames} is the total number of frames, and N_λ is the total number of wavelengths. On this matrix, in order to extract the principal components which will be subsequently removed, an algorithm based on singular value decomposition (SVD) was applied, following the procedure detailed in Section 4.4.1. Finally, the resulting images are derotated by the corresponding parallactic angle to align them with each other, ensuring that North points up and East points left. The number of principal modes to subtract is not fixed and depends on the specific case. In this analysis, various numbers of principal modes were subtracted to allow for a comparison at the end and to select the choice that provided the best results. Specifically, 5, 10, and 15 principal components were subtracted from the IRDIS data, while from the IFS data 10, 50, 100, and 150 principal components were subtracted. In none of the resulting PCA-subtracted images is any companion evident, as there are not planet-like structures distinguishable from the background. Figure 5.8 shows four examples of PCA-subtracted images, two from IRDIS and two from IFS, comparing the effect of subtracting different numbers of modes. The images clearly show that subtracting a higher number of principal components leads to a more effective removal of speckle noise, as well as a stronger attenuation of the coronagraphic residuals around the star.

A Signal-to-Noise Ratio (S/N) map is then created for the PCA-subtracted images to identify regions where the signal of an object, if present, is distinguishable from the background noise. It has to be determined in which case a planet is detectable, and here it was assumed that a planet is detectable if its Signal-to-Noise ratio is above the value of 5. The S/N is defined and calculated as follows:

1. for each pixel (hereafter denoted as p), the integrated flux (F) is calculated within an aperture of radius $0.5\lambda/D$, and then normalized by the area of the aperture. Here, λ is equal to $2.251\,\mu m$ for IRDIS and $1.30\,\mu m$ for IFS, corresponding to the mean value of their respective covered spectral bands, and D is the telescope diameter;

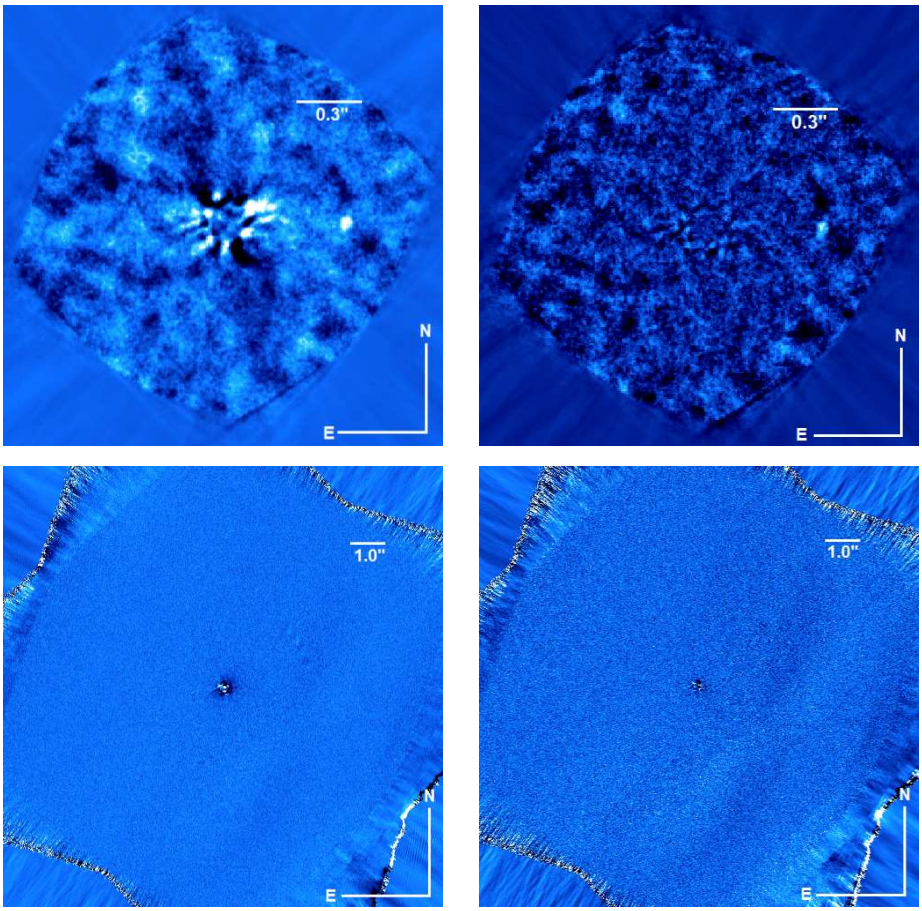

Figure 5.6: Images obtained by applying the PCA method. *Upper panel*: IFS images obtained by subtracting 50 principal components (upper left) and 150 principal components (upper right). *Bottom panel*: IRDIS images obtained by subtracting 5 principal components (bottom left) and 15 principal components (bottom right).

2. an annulus, with inner radius $3\lambda/D$ and outer radius $6.5\lambda/D$, centered on p, is considered;

3. another annulus, centered on the star and with outer and inner radii of $r \pm 0.5\lambda/D$, respectively, is considered, where r is the distance between the star center and p;

4. the noise is estimated as the standard deviation σ of the pixel intensities within the region defined by the intersection of the two annuli. The Signal-to-Noise ratio for each pixel p is then defined as $S/N = F/\sigma$.

To avoid an overly computationally intensive procedure, the S/N is not computed across the entire image but only within a region centered on the star. Specifically, for IRDIS, the S/N is calculated for each pixel located within a 600×600 pixel window centered on the image, while for IFS the same approach is applied using a 200×200 pixel window. An inspection of the resulting S/N maps reveals that none of them show any signal of significant importance, with no detections reaching a S/N greater than 5. Consequently, no candidate companion is identified from these maps. Two examples of S/N maps, one for IRDIS and one for IFS, are shown in Figure 5.7

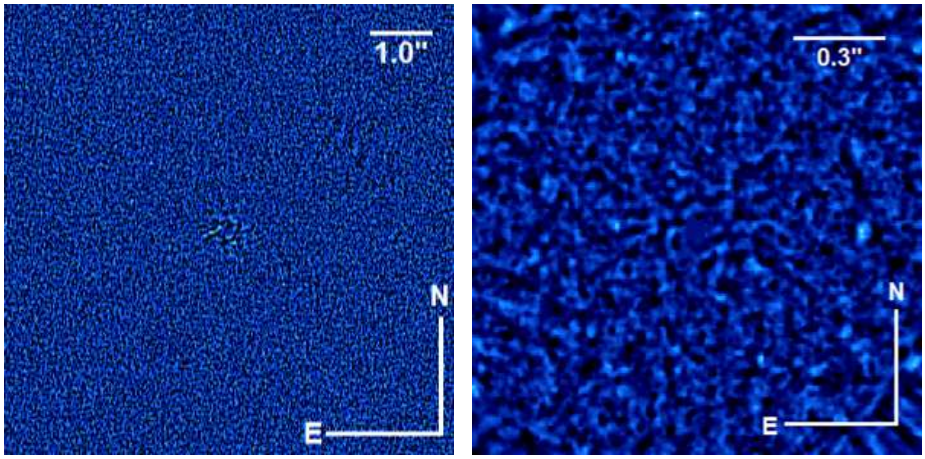

Figure 5.7: S/N maps both for IRDIS (*left*) and IFS (*right*). The IRDIS image is obtained by applying a PCA subtracting 5 principal components, while for IFS 50 principal components were subtracted.

The next step involves modeling and correcting the self-subtraction effect introduced by the application of differential imaging techniques. One of the most commonly used techniques to correct for self-subtraction, and the one adopted in this work, is based on the injection of synthetic planets into the datacube containing all the science-reduced images. These simulated planets, characterized by a known PSF shape and contrast with respect to the stellar flux, serve as a tool to model the self-subtraction effect and to quantify how the PCA process attenuates the signal of actual companion candidates. The modified datacubes, now containing the synthetic sources, are then processed with PCA using the same number of principal components subtracted from the original science data. This approach allows to assess how PCA affects the detectability of planets with known properties (such as flux and spatial profile), and to derive the detection limits, beyond which a companion's presence should be revealed, and below which its existence cannot be confirmed nor excluded.
In this work, seven simulated planets with a contrast of 10^{-4}, evaluated using the off-axis PSF employed in the flux calibration step, were injected into the IFS scientific datacubes, at different angular separations from the host star: 0.2,

0.3, 0.4, 0.5, 0.6, 0.7, and 0.8 arcseconds. For IRDIS, thirteen simulated planets with the same contrast were injected at the following separations: 0.2, 0.3, 0.4, 0.5, 0.6, 0.7, 0.8, 0.9, 1.0, 1.5, 2.0, 2.5, and 3.0 arcseconds. The injected planets are also rotated by the same parallactic angle associated with each image, ensuring that their position changes from frame to frame, as it would for real planets observed in actual observations. To model this effect, the peak value of the PSF for each synthetic planet is normalized by subtracting the mean background value and then dividing by the maximum value of the entire datacube containing the injected planets. As expected, the self-subtraction effect is more pronounced closer to the star and increases with the number of PCA modes subtracted. These results are then used to calculate the contrast, as explained in the following section. Four examples of PCA-subtracted images containing synthetic planets are shown in Figure 5.8, with two examples for each instrument, comparing the effect of subtracting different numbers of modes.

5.1.5 Results

The first key result obtained in this work is the limiting contrast reached during the observations. This contrast strongly depends on the angular separation from the host star: it is lower at small separations and improves at larger distances. The contrast is typically presented in the form of contrast curves in flux-separation (or Δmag-separation) space. These curves indicate the detection limits of the observation: sources falling below the curve are not detectable, while sources above the curve are, in principle, detectable.
In this work, the limiting contrast is derived through the following steps. First, both the original datacube and the PCA-subtracted images, corresponding to each choice of the number of principal components, are used to compute a one-dimensional radial profile of the residual noise. This is done by calculating the standard deviation of the pixel values at increasing radial separations from the star. To estimate the 5σ contrast, the standard deviation at each separation is multiplied by 5 and normalized by the median peak intensity of the stellar PSF. Subsequently, a correction for the self-subtraction induced by the PCA process is applied. This correction is based on the analysis of the peak flux attenuation observed in the synthetic planets injected at various separations. An interpolation of the self-subtraction values is performed to obtain a continuous correction as a function of separation. The final contrast curve is obtained by dividing the initial 5σ contrast by this correction factor, separately for each PCA configuration. As an example, the resulting contrast curves for the observations of December 2 , obtained subtracting a different number of principal modes, are shown in Figure 5.9. It is evident that the application of PCA leads to a contrast improvement exceeding two orders of magnitude compared to images where the speckle noise has not been subtracted. Furthermore, increasing the number of subtracted principal components generally results in a marginally better contrast. Finally, a combined contrast curve is computed by taking the lowest value at each separation among the available curves, and this will be used in the subsequent analysis. This procedure was applied separately

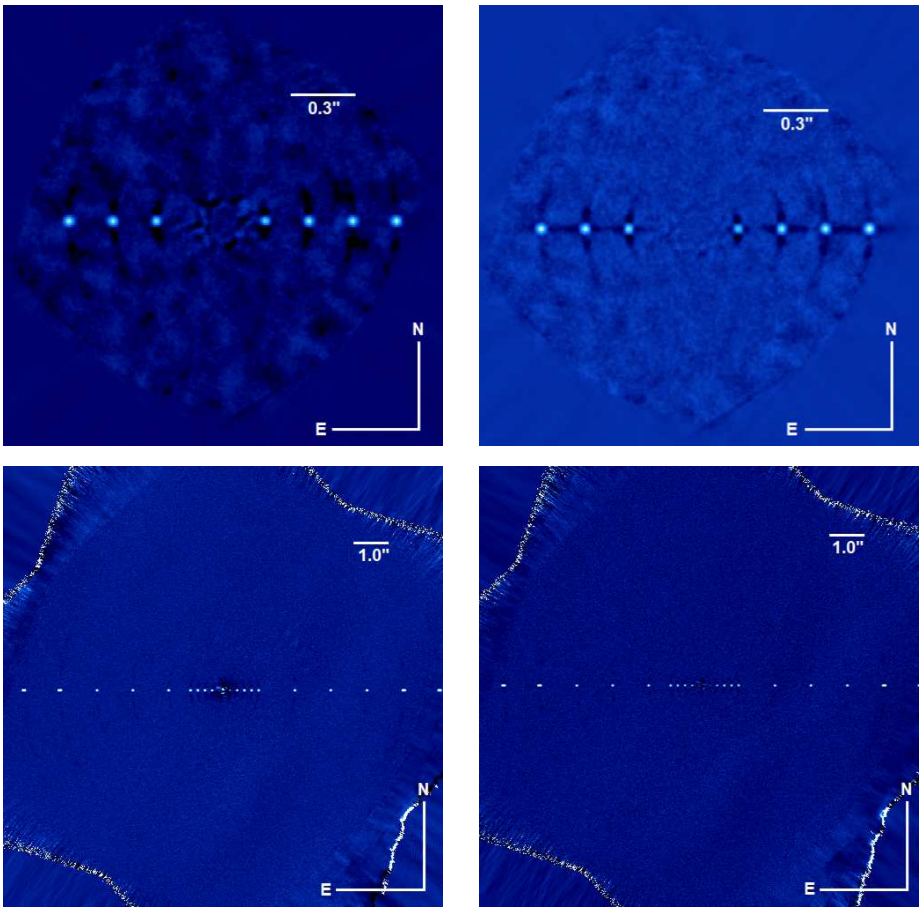

Figure 5.8: Images obtained by applying the PCA algorithm to datasets with injected synthetic planets. *Upper panels*: IFS images obtained by subtracting 50 principal components (upper left) and 150 principal components (upper right). *Lower panels*: IRDIS images obtained by subtracting 5 principal components (bottom left) and 15 principal components (bottom right).

for both IRDIS and IFS.
For the final analysis, the dataset of highest contrast among the three available was selected. Figure 5.10 presents the best contrast curves in both flux and magnitude for all epochs. In these plots, the solid lines extending to $5''$ correspond to IRDIS, while the shorter and dashed ones represent IFS. The results indicate that the November observation yielded the poorest contrast, whereas the October and December observations achieved comparable performance. However, the December dataset provided slightly better contrast, particularly with IFS. Moreover, when comparing only the October and December datasets, the December observation stands out for its superior atmospheric conditions, char-

acterized by lower seeing and a comparable coherence time (τ_0). Due to all these factors, after completing the data reduction, the post-processing and the contrast calculation for all three available epochs, the December dataset was selected for the final analysis. Moreover, it offers a larger field-of-view rotation, a key factor in ADI.

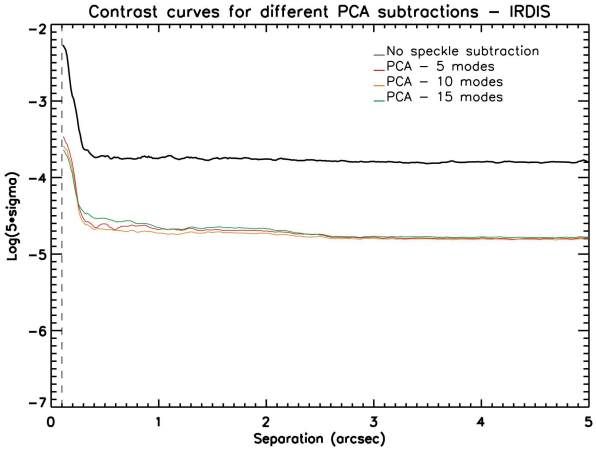

(a)

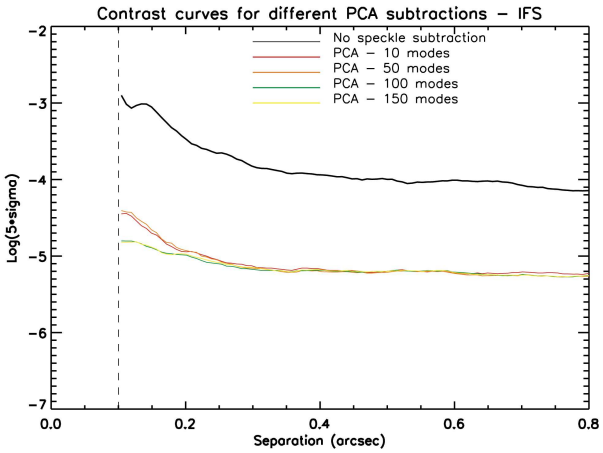

(b)

Figure 5.9: Contrast curves from IRDIS (a) and IFS (b) data processed with PCA, illustrating the impact of increasing the number of subtracted principal components on speckle noise suppression. For IRDIS, 5, 10, and 15 components were subtracted, while for IFS 10, 50, 100, and 150 components were used. The vertical dashed line indicates the radius of the coronagraph. These plots relate to the December 2 observations.

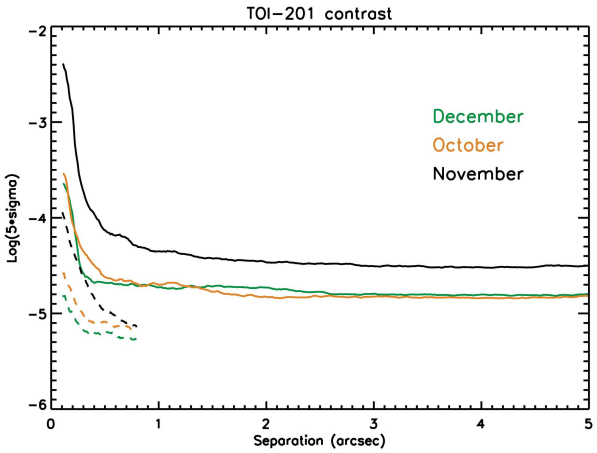

(a)

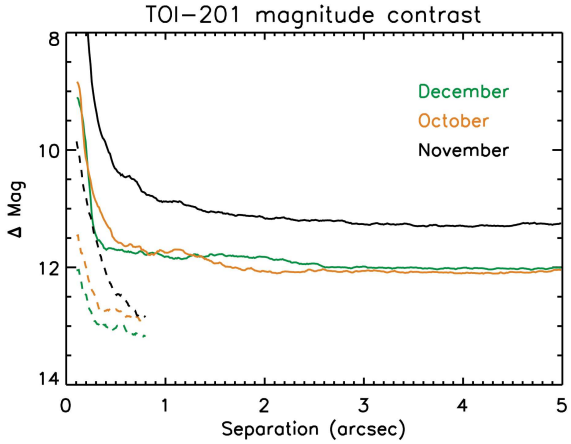

(b)

Figure 5.10: Comparison of the 5σ flux (a) and magnitude (b) contrast across the three observation epochs.

From the contrast achieved before, it is possible to derive the detection upper limits for the mass of the companion. The estimation of these upper limits was performed using the AMES-COND atmospheric models (Allard et al. [2001]), which are specifically designed to describe the atmospheres of cold substellar objects, such as brown dwarfs and giant exoplanets. These models are fully valid for effective temperatures $T_{eff} \lesssim 1300\ K$, and partially valid in the range between 1300 and 1800 K. The main assumption of the COND model is that cloud layers form below the photosphere, where gravitational settling efficiently removes dust from the visible atmosphere. The model assumes equilibrium

chemistry, where dust condenses and rains out of the atmosphere, resulting in dust-free spectra, hence the name "COND" (for condensed). For objects with T_{eff} between approximately 1300 and 1800 K, partial settling occurs, and some dust remains suspended in the atmosphere. At even higher temperatures ($T_{eff} \gtrsim 1800\ K$), dust remains in equilibrium with the gas phase, with negligible sedimentation (the so-called dusty regime). The AMES-COND model is therefore suitable for this study, which, based on the PMa data, focuses on the search for cold substellar companions. For these objects, the model operates well within its full range of applicability.

The contrast limits obtained for both IRDIS and IFS in the H and K spectral bands are first converted into limiting magnitudes, yielding the minimum absolute magnitude that an object must have to be detectable in each band. The limiting magnitudes are then directly translated into upper mass limits through the model, determining the minimum companion mass that would be detectable given the achieved contrast. This is performed for the central value of the stellar age, as well as for its upper and lower uncertainty bounds, through interpolation. The AMES-COND models are in fact provided for discrete ages ranging from 1 Myr to 10 Gyr; in this case, the age of TOI-201 is estimated to be 870 Myr, with an upper limit of 1.33 Gyr and a lower limit of 380 Myr, as reported in Table 5.1. As a result, upper mass limits for potential companions are derived separately for both IRDIS and IFS. The inner separation boundary is dictated by the presence of the coronagraph and the distance of the target. Specifically, the coronagraph used during the SPHERE observations has an inner working angle (IWA) of $0.12''$. Given that TOI-201 is located at a distance of 112.18 pc from Earth (as derived from the Gaia EDR3 parallax of 8.914 ± 0.014 mas), this angular separation corresponds to a projected orbital distance of approximately 13.46 AU. Consequently, any object located within this region is masked by the coronagraph, and its presence or absence cannot be confirmed nor excluded based solely on the imaging data, as the instrument is effectively blind in this inner region. The derived upper mass limits are shown in Figure 5.11, where the limits obtained from the IRDIS 5σ contrast are plotted in green and those from the IFS 5σ contrast in orange. Solid lines correspond to the central value of the stellar age, while dashed and dash-dotted lines represent the upper and lower age estimates, respectively.

From these results, the difference in detection capability between IRDIS and IFS becomes evident. IFS achieves a deeper contrast, potentially allowing the detection of lower-mass objects compared to IRDIS. However, due to its smaller field of view, its detection capability is confined to a narrower region around the star. Specifically, the FoV of IFS limits the observable region to within $0.8''$ from the star, excluding the edges, which often present unreliable behavior. Given the distance of TOI-201 from the Earth, this angular separation corresponds to approximately 89.74 AU from the central star. IRDIS, on the other hand, although not capable of achieving the same contrast depth as IFS, has a significantly larger FoV, covering a circular region with a radius of approximately $5''$. This translates to an orbital separation of about 560.91 AU from the star, allowing the detection of objects at larger distances, albeit in a

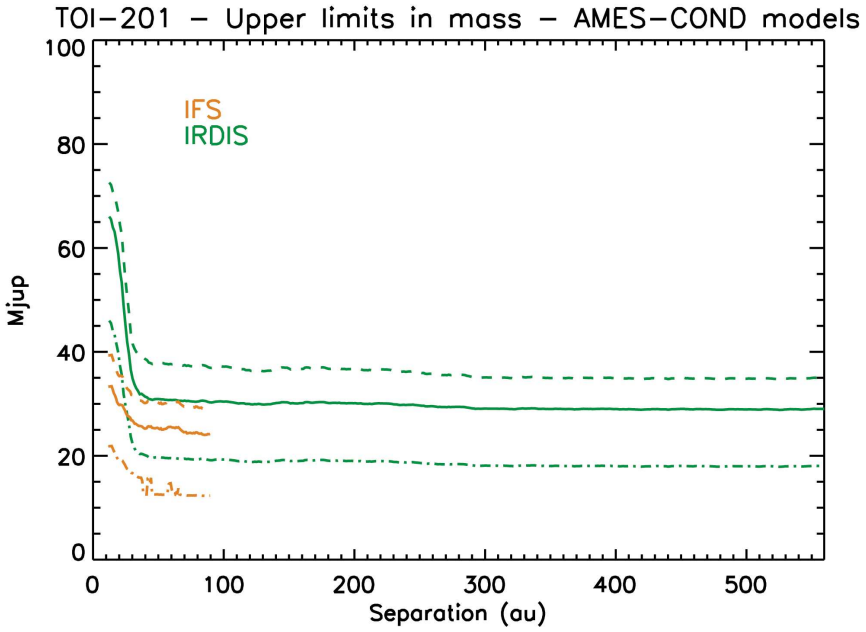

Figure 5.11: Upper mass limits obtained from AMES-COND models for both IRDIS (green lines) and IFS (orange lines).

higher mass regime. A combined contrast curve is then calculated by selecting, at each separation, the lowest contrast value between the two instruments.
For a stellar age of 870 Myr, the upper mass limit is approximately 33 M_J at the inner detectable boundary, decreases to a minimum of $\sim$ 24 M_J at around 90 AU, rises again to about 30 M_J, and eventually settles at $\sim$ 29 M_J at the widest separations. For an older age of 1.33 Gyr, the limit starts at $\sim$ 39 M_J, reaches a minimum of $\sim$ 29 M_J, increases to $\sim$ 37 M_J, and flattens at about 35 M_J at 560 AU. Conversely, for a younger age of 380 Myr, the mass limit begins at $\sim$ 22 M_J, drops to a minimum of $\sim$ 12 M_J, rises to $\sim$ 19 M_J, and eventually stabilizes at $\sim$ 18 M_J. The observations did not reveal any evidence for the presence of companions orbiting TOI-201. Overall, under the most conservative scenario, we can exclude the presence of brown dwarfs and stars with masses $M \gtrsim 39\ M_J$ around TOI-201 between $\sim$ 13.5 and $\sim$ 561 AU from the host star. However, no constraints can be placed, based on direct imaging alone, on the existence of lower-mass substellar companions.
To place tighter constraints on the mass of a potential companion, a combined analysis of direct imaging and proper motion anomaly data has been performed. The PMa values, summarized in Table 5.2, and the corresponding companion mass estimates as a function of orbital separation, shown in Figure 5.1, provide significant constraints on the possible orbital configurations for a wide range of separations. In particular, assuming a $1.30 \pm 0.06\ M_\odot$ mass for the host star,

the Kervella et al. [2022] catalogue estimates a companion dynamical mass of 26.26 M_J at a separation of 3 AU, of 18.32 M_J at 5 AU, of 20.97 M_J at 10 AU and of 75.90 M_J at 30 AU, indicating that the observed PMa is compatible with a brown dwarf across this entire range of separations, and with a stellar companion at even larger distances. These can be further refined by including the upper mass limits derived from direct imaging. The resulting combined constraints in the mass–separation parameter space for TOI-201 are illustrated in Figure 5.12.

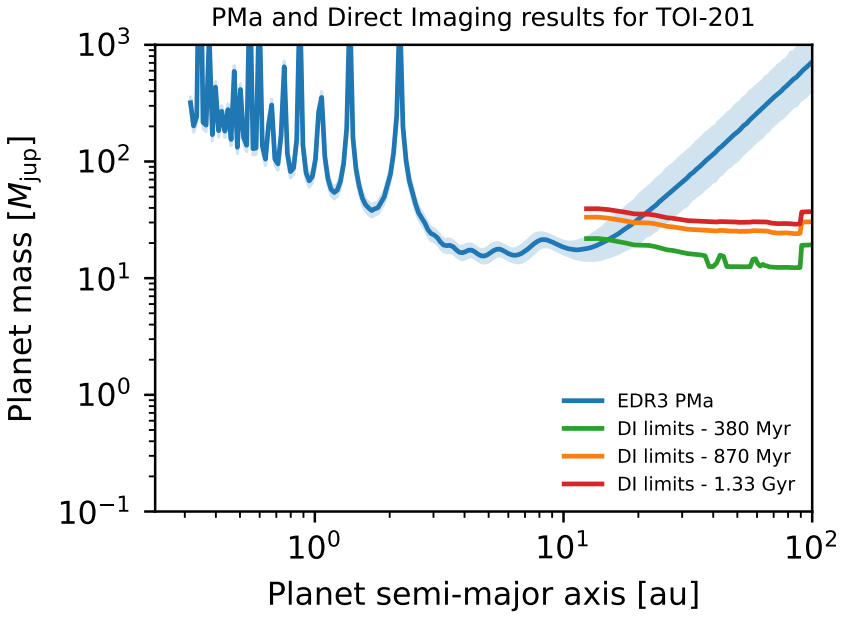

Figure 5.12: Comparison between the mass limits obtained from the SPHERE observations with the PMa. The upper mass limits obtained from the SPHERE observations for the minimum, expected and maximum ages are represented by the green, orange and red solid lines, respectively. The blue solid line represents the companion mass compatible with the PMa data.

With this combined analysis, the presence of a stellar object orbiting TOI-201 beyond $\sim$ 20 AU can be excluded. In this separation range, the observed PMa would correspond to a companion more massive than $\sim$ 35 M_J, which would have been detected in the SPHERE observations. In the region between $\sim$ 13 and 20 AU, the PMa signal is consistent with a companion mass between $\sim$ 19 and 35 M_J. The presence of such an object in this range of separation and mass cannot be ruled out based on imaging data alone. Indeed, around 20 AU, the expected mass from PMa is in the range of 20–40 M_J: detectable

for the minimum stellar age of 380 Myr, but below the detection threshold in the case of the older age estimate of 1.33 Gyr. Closer to the star, between approximately 17 and 20 AU, the PMa corresponds to a mass between $\sim$ 20 and 31 M_J, which would remain undetected for a stellar age of 870 Myr but would be detectable in the younger age scenario of 380 Myr. Finally, in the innermost detectable region between $\sim$ 13.5 and 17 AU, the inferred mass is in the range of $\sim$ 18 to 20 M_J, which lies below the detection threshold even for the lower age estimate. As previously discussed, direct imaging cannot constrain the presence of any companion at separations smaller than $\sim$ 13.46 AU due to the coronagraphic mask. Additional constraints on the innermost part of the system require further information from techniques capable of probing closer-in regions, which will be discussed in the following section.

5.2 RV and PMa joint fit

As discussed in the previous section, imaging data provided upper limits on the mass of the potential companion, and the joint analysis with PMa data allowed us to exclude the presence of a stellar or massive brown dwarf companion orbiting TOI-201 beyond approximately 20 AU. Furthermore, the inner region of the system, specifically within $\sim$ 13.46 AU, is not accessible through direct imaging due to the coronagraph, which masks the central area around the star. As a result, no conclusions can be drawn from imaging in this region, and the presence of potential companions remains unconstrained by this technique. The PMa data, nevertheless, provide information on this inner zone. Between $\sim$ 3 and 10 AU, the estimated dynamical mass ranges from approximately 18 to 27 Jupiter masses, which rules out both planetary and stellar companions in this range, suggesting that the observed PMa is likely caused by a low-mass brown dwarf orbiting TOI-201.
However, it is important to note that PMa data are less reliable for lower separations, as evidenced by the spikes in the mass–separation plot shown in Figure 5.12, and these fluctuations arise from several limiting factors, one of them being the so-called window smearing. In fact, the proper motion measurements are not instantaneously measured quantities, but they result from several observations of the field of view obtained over a period of δt_H = 1227 d for Hipparcos and δt_{G3} = 1038 d for Gaia DR3. The PMa $\boldsymbol{\Delta\mu}$ is therefore a time average of the intrinsic velocity vector of the star over the observing period. This drastically reduces the sensitivity to companions with orbital periods shorter than these time windows and, in the extreme case that the orbital period is exactly δt, no PMa will be detectable. In order to estimate this effect, it is useful to compute the orbital separations corresponding to the Hipparcos and Gaia DR3 baselines, under the simplified assumptions of a circular orbit and negligible companion mass. In particular, an orbital period equal to δt_H corresponds to a separation of approximately 2.46 AU, while a period equal to δt_{G3} corresponds to about 2.19 AU. Although these are idealized scenarios, they are not far from reality. Indeed, by analyzing the plot, it can be observed that the anomalous behavior

begins shortly after 2 AU.
In order to obtain reliable results and better constraints on the properties of the companion, a multi-technique approach can be adopted. In particular, a combined analysis including the available radial velocity measurements for TOI-201 can be performed. To integrate the various datasets obtained through different techniques, the orvara code (Orbits from Radial Velocity, Absolute, and/or Relative Astrometry; Brandt et al. [2021]) was used. A detailed description of its functionality will be provided in the next section.

5.2.1 orvara

The orvara tool, distributed as an open-source Python package, is capable of performing parameter fits for multi-planetary systems or binary stars by combining data from the Hipparcos-Gaia Catalog of Accelerations (Brandt [2018]; Brandt [2021]), radial velocity measurements, and relative astrometry. The strength of this approach lies in its versatility, as it allows for the joint analysis of data collected using different observational techniques. As previously discussed in Chapter 3, each detection method is particularly sensitive to planets within specific ranges of mass and orbital separation from the host star. A multi-technique approach is therefore the most effective way to accurately sample the parameter space. Absolute astrometry can provide strong constraints on orbital parameters even when only a small fraction of the orbit is observed, the combination of proper motions from Gaia and Hipparcos enables the measurement of accelerations in the plane of the sky, while radial velocity trends add complementary information by constraining the acceleration along the line of sight. Finally, direct imaging supplies projected separations and position angles of the companions, which contribute to refining orbital solutions even in the absence of long-term orbital monitoring.
This tool is also capable of modeling systems with multiple companions orbiting the primary star, by approximating the star's motion as a superposition of Keplerian orbits, one for each companion. While using the orbital elements of each object, the code modifies the total mass accordingly. Specifically, when computing the mutual orbit between the primary star and a given companion, the mass of all companions located interior to that orbit is added to the stellar mass. This effectively treats the star and its inner companions as a single body, and computes its motion around the barycenter induced by the companion under consideration. The resulting contributions to the primary star's motion from all companions are then summed for both radial velocity and absolute astrometry. In the case of relative astrometry, the tool assumes that companions exterior to the one under consideration have negligible influence. It first models the relative orbit between the companion and the barycenter of the star plus all inner companions, and then includes the offset of the star relative to this barycenter, as induced by the inner companions.

5.2.2 Data used

Since the SPHERE observations resulted in no detected companions, relative astrometry data were not available for the subsequent analysis. Therefore, the combined fit was performed using only absolute astrometry and radial velocity measurements. The absolute astrometry measurements for TOI-201 were obtained from the Hipparcos-Gaia Catalog of Accelerations. This catalogue, based on a cross-calibration between the Hipparcos and Gaia EDR3 data aimed at identifying accelerating stars, provides three distinct proper motion measurements, each with calibrated uncertainties in the Gaia EDR3 reference frame: the Hipparcos proper motion, the Gaia EDR3 proper motion, and the long-term proper motion, calculated from the positional difference between the Hipparcos and Gaia EDR3 epochs. The values of these three proper motions, along with their associated uncertainties, are summarized in Table 5.4.

	μ_α **(mas/yr)**	μ_δ **(mas/yr)**
Hipparcos	8.950 ± 0.870	67.196 ± 1.000
Gaia EDR3	8.032 ± 0.025	66.633 ± 0.026
Long-term	8.164 ± 0.032	66.847 ± 0.031

Table 5.4: Proper motion of TOI-201 from Hipparcos (epoch 1991.25), Gaia DR3 (epoch 2016.0) and long-term obtained from Gaia EDR3 and Hipparcos positional difference.

From these values, it is possible to compute (with the procedure detailed in Section 3.3) the PMa vectors for both Hipparcos and Gaia DR3 epochs, together with their corresponding Signal-to-Noise ratios. The PMa values derived from the Brandt catalogue are reported in Table 5.5.

	$\Delta\mu_\alpha$ **(mas/yr)**	$\Delta\mu_\delta$**(mas/yr)**	**SNR**
Hipparcos	0.786 ± 0.871	0.349 ± 1.000	0.65
Gaia EDR3	-0.132 ± 0.041	-0.214 ± 0.041	4.39

Table 5.5: Proper motion anomaly values and associated SNR for TOI-201 from Hipparcos (epoch 1991.25) and Gaia DR3 (epoch 2016.0).

Radial velocity measurements for TOI-201 were collected using FEROS, HARPS, CORALIE, and MINERVA-Australis, and were published and analyzed in Hobson et al. [2021] to validate and characterize the planet TOI-201 b. A total of 163 spectra were obtained, covering the time period from November 27, 2018 to May 9, 2020.

- **FEROS** A total of 52 spectra were obtained with the FEROS échelle spectrograph (Kaufer et al. [1999]), mounted on the MPG/ESO 2.2 m

telescope at La Silla Observatory, between November 27, 2018 to May 9, 2020. The spectra, which have a median S/N of 167, have a median error of $\sigma_{FEROS} \approx 9.1\ m/s$.

- **HARPS** The HARPS spectrograph (Mayor et al. [2003]), attached to the ESO 3.6 m telescope at La Silla Observatory, collected 39 spectra in the period between December 12, 2018 to February 22, 2020. The collected spectra, which have a median S/N of 109, have a median error of $\sigma_{HARPS} \approx 2.0\ m/s$.

- **CORALIE** 10 spectra of TOI-201 were obtained with the CORALIE spectrograph (Queloz et al. [2001]), installed at the 1.2 m Swiss telescope at La Silla Observatory, between December 10, 2018 and March 27, 2019. The spectra, which have a median S/N of 45.7, have a median error of $\sigma_{CORALIE} \approx 12\ m/s$

- **MINERVA-Australis** MINERVA-Australis is an array of four 0.7 m telescopes located in Queensland, Australia, fully dedicated to the precise RV follow-up of TESS candidates (Addison et al. [2019]). 62 spectra were collected between January 2, 2019 to April 15, 2019. The retrieved spectra have a median error of $\sigma_{MINERVA} \approx 15.5\, m/s$.

For the subsequent analysis, only the radial velocity data collected with HARPS and FEROS were used, as they are the most reliable, exhibiting higher signal-to-noise ratios and lower median uncertainties compared to the CORALIE and MINERVA spectra. Furthermore, the time coverage of the CORALIE and MINERVA datasets is fully encompassed by that of HARPS and FEROS, providing no additional temporal information. Therefore, their exclusion does not result in any loss of accuracy or completeness.
As reported in Hobson et al. [2021], RV data confirm the presence of TOI-201 b, characterized by an orbital period of 52.97818 ± 0.00004 days, a radius of $1.008^{+0.012}_{-0.015}\ R_J$ and a mass of $0.42^{+0.05}_{-0.03}\ M_J$, while the second TESS candidate, TOI-201.02, remains undetected. However, the RV data also show a long-term trend, which Hobson et al. [2021] interpreted as a stellar activity signal. This interpretation is supported by the periodogram of the H_α activity indicator, which exhibits a significant peak, well above the 0.01% False Alarm Probability (FAP), at long periods, around 300 days. Nevertheless, a long-term trend in the RV signal may also indicate the presence of an additional companion orbiting at a larger distance from the host star than TOI-201 b. This hypothesis is further supported by the proper motion anomaly data. The PMa data, which were neither mentioned nor used in Hobson et al. [2021], are consistent with the presence of a long-period companion. For this reason, in the present work, the observed RV trend will be interpreted as a potential indicator of such a companion. However, the effect of stellar activity should not be neglected, as it can introduce distortions in the radial velocity curve, causing deviations from the signal expected from a purely planetary origin. To model its effect, we included a RV jitter term in our analysis (described in detail in Section 5.2.4).

A multi-technique approach, as described in the previous sections, will be employed to determine the most probable set of orbital parameters consistent with the available data.

5.2.3 RV data analysis

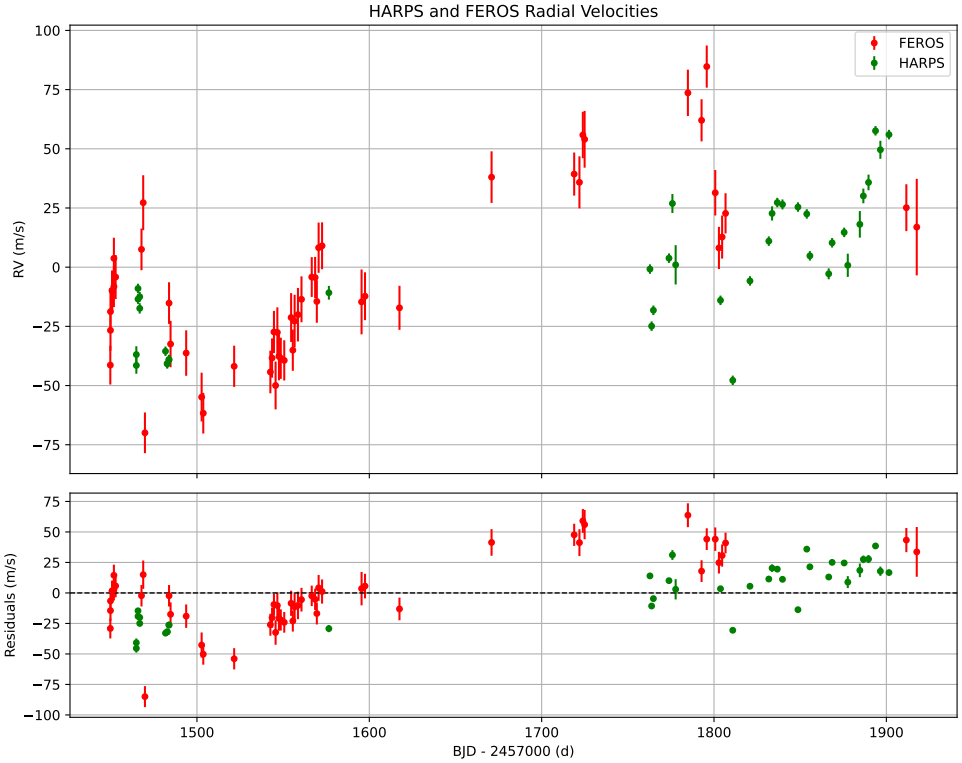

Figure 5.13: *Upper panel*: RV measurements for TOI-201 from FEROS and HARPS. *Bottom panel*: residuals after the modeling of the 53-day planetary signal.

To isolate the signal potentially associated with an outer companion, a single-planet fit was initially performed using the PyORBIT package for Markov Chain Monte Carlo modeling of radial velocity data (Malavolta et al. [2016]; Malavolta et al. [2018]), focusing on the 53-day signal produced by TOI-201 b. The resulting single-Keplerian model was subtracted from the original RV time series to remove the contribution of the known inner planet. This step is justified by the fact that TOI-201 b cannot account for the observed PMa signal, given that its mass and orbital separation are incompatible with the mass–separation relation inferred from the PMa. Subtracting its contribution leaves a residual RV signal attributable only to a possible long-period companion. This step facilitates

convergence in the subsequent modeling phase and improves the accuracy of the single-planet fit for the outer companion. As a result, the RV data input to orvara consisted of these one-Keplerian residuals, allowing the tool to focus exclusively on modeling the long-term trend without refitting the known inner planet. Figure 5.13 shows the original HARPS and FEROS radial velocity data, along with the residuals following the fit of the 53-day planetary signal.

In order to determine the detection limits of the radial velocity data, an injection and retrieval technique, with a similar approach to the one used in Barbato et al. [2018b], was applied. Synthetic companion signals were injected into the residual radial velocity time series. The injections were performed over a 200×200 grid, evenly spaced in logarithm in semi-major axis from 0.05 to 100 AU and in minimum mass from 0.01 to 1000 Jupiter masses. For each of the resulting $4 \cdot 10^4$ configurations, 100 radial velocity curves were generated using random values of eccentricity (drawn from a Kipping Beta distribution describing the observed exoplanetary eccentricities; Kipping [2013]), mean longitude, and argument of periastron (both uniformly distributed between 0 and 360 degrees), leading to a total of $4 \cdot 10^6$ synthetic RV curves. These curves were computed by evaluating the theoretical RV signal induced by such companions at the actual epochs of the RV observations. Each synthetic curve was then added to the real residuals, and a periodogram was computed, calculating the FAP of the injected signal. An injected planet was considered detectable if the FAP at its orbital period is lower than 0.1 % The results were used to construct a 100 % detection completeness curve, which is shown in Figure 5.14, together with the detection limits derived from imaging and PMa data. The RV detection curve has been truncated at orbital separations beyond ~ 15 AU to avoid overlapping with the mass limits derived from the imaging observations.

This curve can be used to rule out the presence of additional companions beyond those already detected in the radial velocity data, namely the inner confirmed planet with a period of 52.9 days and the long-period object responsible for the observed trend. All mass–separation realizations lying above the detection curve correspond to objects that would have been detectable with the available RV data. Since no additional signals are observed beyond those already known, the existence of such objects can be excluded. Conversely, the presence of companions with mass–separation combinations lying below the detection curve cannot be confirmed nor excluded based on the RV data alone, as they fall below the sensitivity threshold of the observations. Additional information about the long-period object can also be inferred. Since it is detected in the radial velocity data as a long-term trend, its mass–separation combination must lie above the RV detection curve. Moreover, being responsible for the observed PMa signal, it is expected to lie close to the PMa sensitivity curve. The intersection of these two constraints allows to place strong limits on its mass and orbital separation from the host star.

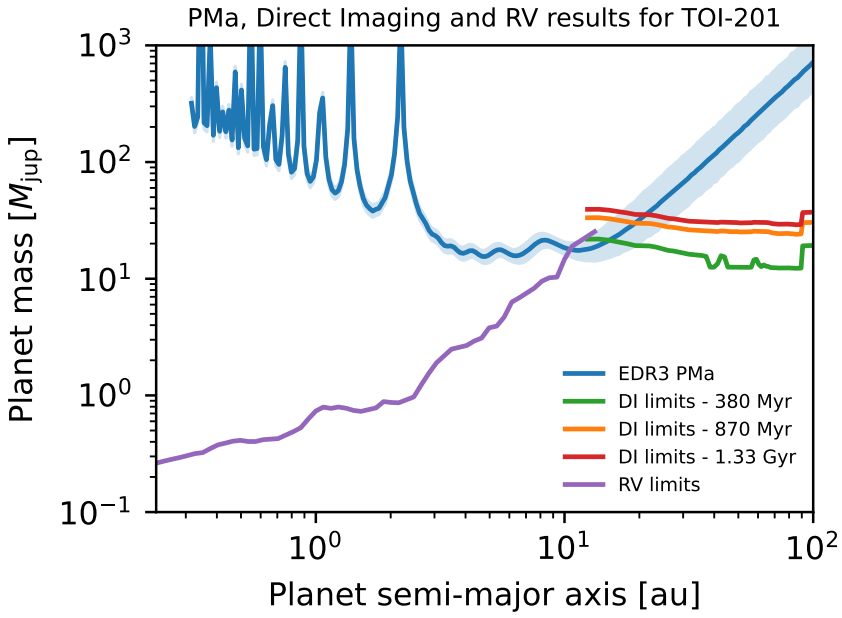

Figure 5.14: Comparison of the mass detection limits derived from SPHERE observations (red, orange, and green lines), the PMa (blue line), and the 100% RV detection curve (purple line).

5.2.4 Joint fit and data analysis

orvara computes the likelihood of an orbit (in absence of relative astrometry data) as:

$$-2\ln\mathcal{L} = \chi^2 = \chi^2_{RV} + \chi^2_{abs\,ast}\,, \tag{5.2.1}$$

where χ^2_{RV} is the chi-squared related to radial velocity data, and $\chi^2_{abs\,ast}$ is the chi-squared related to absolute astrometry data. For the RV, the chi-squared is defined as:

$$\chi^2_{RV} = \sum_{j=1}^{N_{inst}} \sum_{k=1}^{N_{RV}} \left[\frac{(RV_k + ZP_j - RV(t_k))^2}{\sigma^2(RV_k) + \sigma^2_{jit}} + ln[\sigma^2(RV_k) + \sigma^2_{jit}] \right]\,, \tag{5.2.2}$$

where ZP_j is the zero point of the j-th instrument, σ^2_{jit} is a jitter term, RV_k indicates the measured RV at epoch t_k, $RV(t_k)$ the model-predicted RV, and $\sigma^2(RV_k)$ is its variance. The jitter term, typically distinct for each instrument due to differences in instrumental precision, is instead assumed to be the same across all the combined RV time series. As a result, its origin is entirely interpreted as being due to stellar activity.

The absolute astrometry chi-squared is defined as:

$$\begin{aligned}\chi^2_{abs\,ast} = (\boldsymbol{\mu}_{H,o} - \bar{\boldsymbol{\mu}} - \pi\boldsymbol{\mu}_H)^T C_H^{-1}(\boldsymbol{\mu}_{H,o} - \bar{\boldsymbol{\mu}} - \pi\boldsymbol{\mu}_H) + \\ (\boldsymbol{\mu}_{HG,o} - \bar{\boldsymbol{\mu}} - \pi\boldsymbol{\mu}_{HG})^T C_{HG}^{-1}(\boldsymbol{\mu}_{HG,o} - \bar{\boldsymbol{\mu}} - \pi\boldsymbol{\mu}_{HG}) + \\ (\boldsymbol{\mu}_{G,o} - \bar{\boldsymbol{\mu}} - \pi\boldsymbol{\mu}_G)^T C_G^{-1}(\boldsymbol{\mu}_{G,o} - \bar{\boldsymbol{\mu}} - \pi\boldsymbol{\mu}_G)\,,\end{aligned} \tag{5.2.3}$$

where, as an example, $\boldsymbol{\mu}_{H,o}$ is the observed Hipparcos proper motion, $\boldsymbol{\mu}_H$ is the model orbit's predicted Hipparcos proper motion and the parallax is denoted by π. The matrices C_i^{-1} represent the inverses of the covariance matrices associated with the astrometric parameters for each instrument. Absolute astrometry measurements include a velocity zero-point, here expressed as $\bar{\boldsymbol{\mu}}$, which corresponds to the proper motion of the system's barycenter projected onto the plane of the sky.

The Monte Carlo simulation was carried out using an ensemble sampler with 100 walkers, each generating five independent chains. Each chain consisted of $2.5 \cdot 10^6$ steps, and a thinning factor of 50 was applied. Additionally, an initial burn-in phase of 1500 steps was discarded for each chain to allow the walkers to converge towards regions of higher posterior probability. The simulation employed a set of prior distributions for the model parameters. The prior on the stellar mass was defined as a normal distribution with a mean of $1.316\,M_\odot$ and a standard deviation of $0.027\,M_\odot$, based on the value reported by Hobson et al. [2021] and also listed in Table 5.1. For the RV jitter term, a broad prior range was selected to avoid underestimating its contribution and to ensure that its impact was properly accounted for in the simulation. Specifically, a log-uniform distribution between $10^{-5}\,m/s$ and $50\,m/s$ was used.

For the semi-major axis prior, a different approach was adopted, based on the constraints provided by the PMa signal, imaging data and radial velocity measurements. As a result, a normal distribution with a mean of 6 AU and a standard deviation of 4 AU was chosen. The available RV data span approximately one and a half years. If the companion had an orbital period equal to or shorter than this timespan, the RV measurements would be expected to show a full oscillation. However, since no such complete oscillation is observed, it is reasonable to conclude that the companion's orbital period must be longer than the duration of the RV monitoring. Assuming a circular orbit and neglecting the companion's mass, this allows us to rule out orbital separations smaller than ~ 1.4 AU. Additionally, within this separation range, the PMa signal would correspond to an object with a mass of $M \gtrsim 40 - 50\ M_J$. Such high masses are inconsistent with the amplitude of the observed RV trend, which favors the presence of a less massive companion. Even for orbital periods which are longer than the RV baseline, for example 2, 3, or 4 times longer (3, 4.5 or 6 years), at least part of the oscillation should be detectable in the data. Instead, the RVs display only a monotonic, approximately linear trend. This further supports the hypothesis of a longer orbital period and allows for tighter constraints on the companion's orbit. Under the same assumptions as before, the orbital separations corresponding to periods of 3, 4.5 and 6 years are approximately 2.3, 3.0, and 3.6 AU, respectively. Separations smaller than ~ 3.6 AU can therefore

be confidently excluded, as the RV data do not show the expected curvature associated with such orbital timescales.
According to imaging observations, the presence of stellar companions at separations larger than $\sim$ 13.5 AU can be ruled out, as such objects would have been detectable. Furthermore, in the range between $\sim$ 10 and 13.5 AU, the companion mass inferred from the PMa signal falls below the RV detection curve; however, since the long-term trend is clearly observed in the RV data, this region can also be excluded from further analysis. In conclusion, the combination of PMa, imaging, and radial velocity constraints supports the adoption of a prior on the semi-major axis spanning approximately from $\sim$ 3.6 to 10 AU. However, the prior used in this analysis extends slightly beyond this estimate, with a lower bound set at 2 AU. This choice was made to encompass a broader range of possible orbital configurations and to avoid prematurely excluding a significant number of orbits based on rough estimates and idealized assumptions. The Monte Carlo simulation showed regular convergence, with no chains becoming trapped in local minima, as confirmed by the diagnostic plot shown in Figure 5.15.

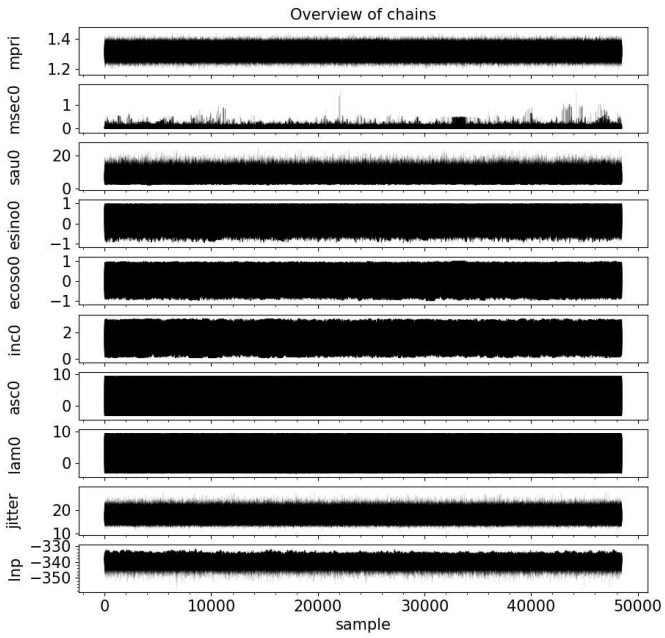

Figure 5.15: Diagnostic plot displaying the MCMC simulation chains used in the orbital parameter estimation. This figure illustrates the evolution of the Markov chains over the sampling steps for several fitted parameters, providing a visual proof of convergence.

The analysis performed with orvara provides several output plots, including the predicted astrometric position at a selected epoch, the temporal evolution of the position angle and relative separation between the companion and the host star, as well as the best-fit solutions for the proper motion and the input radial velocity data. However, since no relative astrometry data were available for this analysis, the astrometric prediction and position angle results are not considered reliable and will therefore not be discussed here. The proper motion values, along with the best-fit solution and the residuals both in right ascension and declination are shown in Figure 5.16.

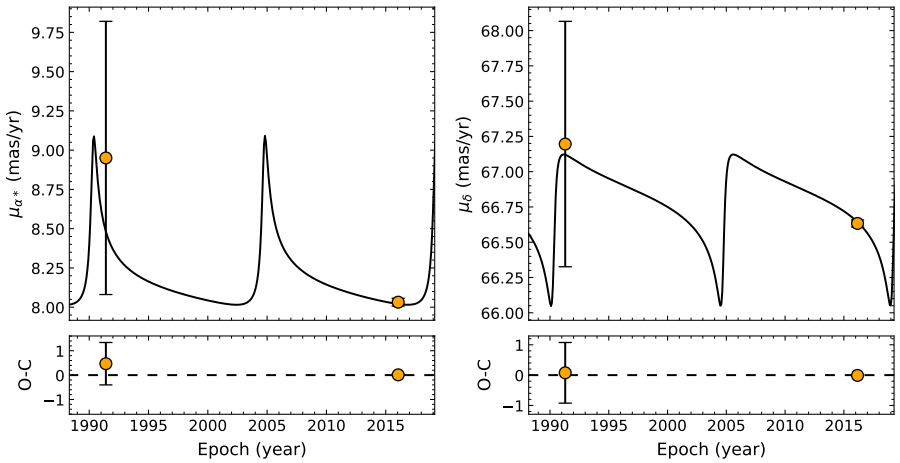

Figure 5.16: Proper motion values in right ascension (*left*) and declination (*right*) for TOI-201. The orange points represent Hipparcos and Gaia EDR3 measurements. The best-fit solution is represented by the solid line, while the lower panels show the residuals.

The radial velocity data employed in this analysis, along with the best-fit solution and residuals, are shown in Figure 5.17. The red points correspond to FEROS measurements, whereas the green points represent the data collected with HARPS.

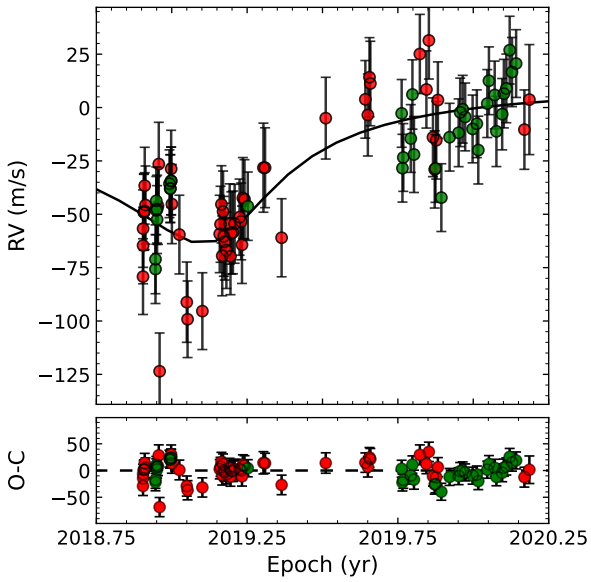

Figure 5.17: Radial velocity data for TOI-201 obtained from HARPS (green) and FEROS (red). The solid line represents the best-fit solution, while the lower panel displays the residuals.

This plot reveals an ascending trend; however, due to the limited temporal coverage of the RV data, which prevents a full determination of the oscillation semi-amplitude, and the absence of relative astrometric measurements, an accurate estimation of the dynamical and orbital parameters of the companion is not feasible. In particular, the determination of the companion's dynamical mass, which strongly depends on the RV semi-amplitude, remains highly uncertain. The uncertainty is more pronounced at higher values, since the data show an upward trend without observing an inversion. Consequently, the dynamical mass estimate is likely to be asymmetric toward larger values. The incomplete coverage of the RV data also introduces uncertainties in the estimation of other orbital parameters, such as eccentricity and period, which cannot be determined with high precision. Table 5.6 reports the best-fit values of the posterior distributions, along with their associated uncertainties, for the stellar mass, the dynamical mass of the companion, and its orbital parameters.

Parameter	Value
Stellar mass ($M_\odot$)	1.316 ± 0.027
Dynamical mass (M_J)	$22.7^{+23}_{-8.4}$
Mass ratio	$0.0165^{+0.017}_{-0.0061}$
a (AU)	$6.8^{+2.0}_{-2.3}$
$\sqrt{e}\sin\omega$	$0.40^{+0.37}_{-0.49}$
$\sqrt{e}\cos\omega$	$0.10^{+0.44}_{-0.49}$
i (°)	93^{+35}_{-39}
P (yrs)	15.4 ± 7.1
e	$0.45^{+0.35}_{-0.31}$
T_0 (JD)	2458034^{+2331}_{-1994}
RV jitter (m/s)	$17.3^{+1.7}_{-1.5}$

Table 5.6: Posterior distributions of the orbital and physical parameters derived from the orvara analysis.

As previously discussed, the limitations of the available data prevent a precise characterization of the companion, resulting in large uncertainties on all derived parameters. The estimated mass is consistent with that of a brown dwarf, located at a distance of approximately 4.5 to 8.8 astronomical units from the host star. A more detailed discussion of these results, and their consistency with the constraints provided by the different techniques, is presented in the following section. Figure 5.18 presents the corner plot of the posterior distributions, illustrating the correlations among the stellar mass, companion mass, semi-major axis, orbital eccentricity, and inclination. The corner plot reveals no evident correlations between the parameters, except for those that are not entirely independent, such as the companion mass and its semi-major axis, although even in these cases the correlations are weak. Due to the large uncertainties affecting the parameter estimates, the distributions are significantly distorted, often appearing as broadened Gaussians or, in cases like the eccentricity, approaching a uniform-like shape. As a result, some apparent relationships in the corner plot are not genuine correlations, but rather artifacts caused by these distortions.

5.3 Final results

As shown in Figure 5.19, the mass and separation values obtained from the orvara analysis are consistent with the previous results. Specifically, the object lies above the radial velocity detection curve, confirming its detection in the RV observations. Additionally, it is consistent with the PMa, as its mass at that separation falls within 1σ of the predicted mass from the PMa model.

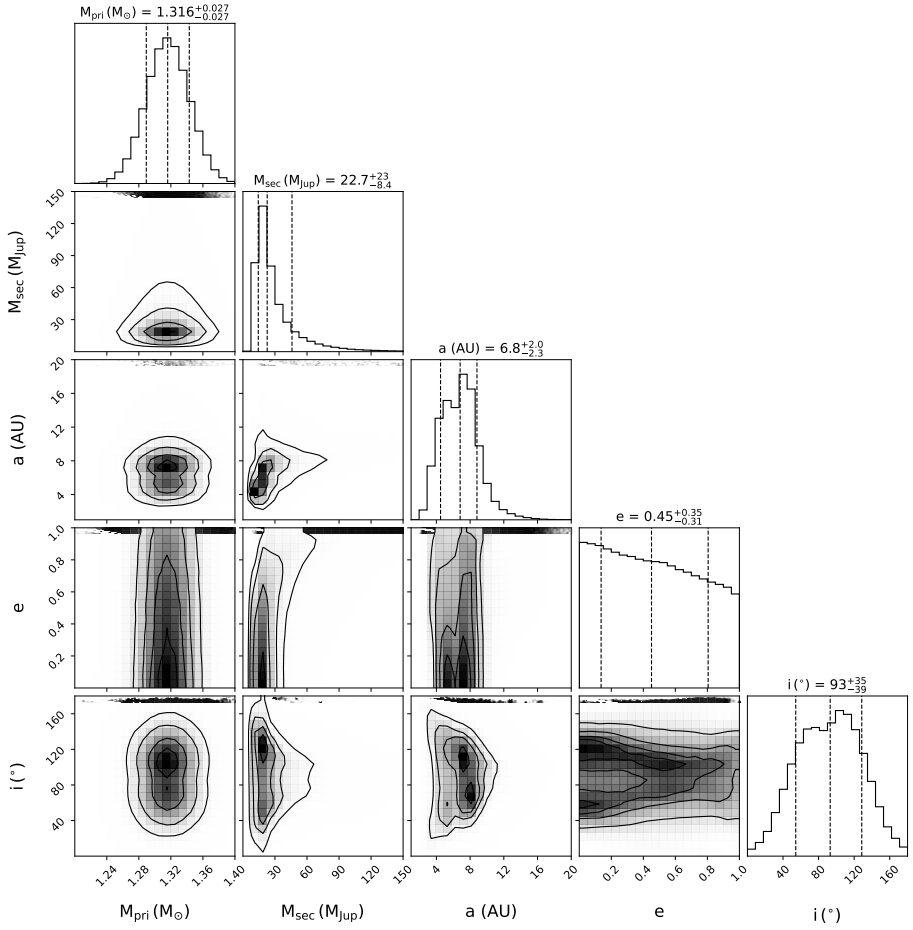

Figure 5.18: Corner plot showing the posterior distributions and correlations among the stellar mass, companion mass, semi-major axis, eccentricity, and inclination.

Furthermore, the object is correctly not detectable by SPHERE observations, as it resides in the inner region that is covered by the coronagraph.
Overall, all the available data support the presence of a low-mass brown dwarf, whose dynamical mass has been estimated at approximately $\sim 22.7\ M_J$. Given that an estimate of the orbital separation from the host star is also available, it is possible to derive the corresponding angular separation. This, in turn, allows for an assessment of the object's detectability with current and future instruments. The angular separation can be estimated from the semi-major axis of the brown dwarf's orbit, reported in Table 5.6 as $6.8^{+2.0}_{-2.3}$ AU, and the distance to TOI-201 from Earth, which is approximately 112.18 pc (as derived from the

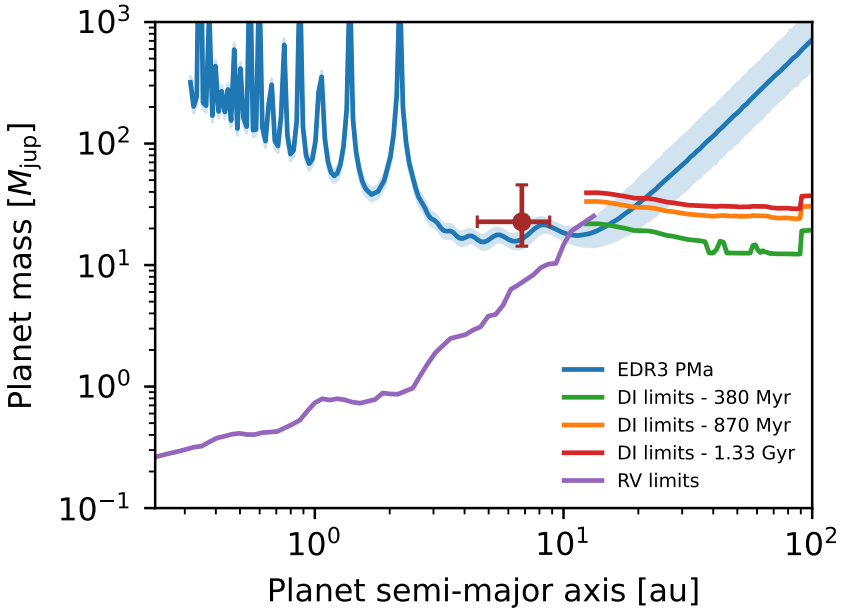

Figure 5.19: Comparison between the mass limits obtained from the SPHERE observations, the RV measurements and the PMa. The brown circle represents the position of the brown dwarf on this diagram.

Gaia EDR3 parallax in Table 5.1). The angular separation θ (in arcseconds) can be calculated using the relation $\theta = \tan \frac{a}{d}$, where a is the semi-major axis in astronomical units and d is the distance in parsecs. The resulting angular separations corresponding to the lower, central, and upper values of the semi-major axis are approximately 40.1, 60.5, and 78.3 mas, respectively.
An estimate of the minimum angular resolution of SPHERE, under the assumption of diffraction-limited performance, can be obtained for the different wavelengths at which the instrument operates. In the case of IRDIS, operating in Dual-Band Imaging (DBI) mode across the spectral range 0.95–2.32 μm, the corresponding angular resolution for an 8-meter telescope ranges from approximately 29.8 to 72.9 mas. For the IFS instrument, a similar approach can be used to estimate the angular resolution in the Y-J (0.95–1.35 μm) and Y-H (0.95–1.65 μm) spectral bands. In the Y-J band, the resolution spans from roughly 29.9 to 42.5 mas, while in the Y-H band it extends from 29.9 to about 51.9 mas. The values we obtained for the brown dwarf's orbit around TOI-201 are larger than the minimum angular resolution achievable with SPHERE for most of the considered wavelengths. However, these values were calculated under the diffraction-limited approximation, which assumes ideal conditions that are often not met in practice due to non-ideal weather and the inherent limi-

tations of the instrument. Furthermore, the coronagraph hides the area within $0.12''$. Without the coronagraph, any object located at such a small separation from the central star, such as this brown dwarf, would be overwhelmed by the stellar light. In conclusion, this object is not detectable with SPHERE under any observational conditions.

The detectability of this object can also be explored in the context of future instruments, such as the MICADO (Multi-AO Imaging Camera for Deep Observations) on the Extremely Large Telescope (ELT), which is expected to achieve first light in 2029 and begin scientific observations in 2030. With a primary mirror diameter of 39 meters and a wavelength coverage between 0.8 and 2.45 μm, its theoretical minimum angular resolution under the diffraction-limited regime can be estimated, ranging from approximately 5.15 to 15.1 mas. While these values are based on ideal conditions, they are significantly lower than the estimated angular separations for the brown dwarf. Therefore, the object could, in theory, be easily detected with MICADO, making TOI-201 a particularly compelling target for future observations. As a result, this region of the planetary system, currently inaccessible to existing instruments, could be explored and characterized with the advanced capabilities of future telescopes.

It is also possible to estimate, using Equation 3.3.1, the astrometric effect induced by the brown dwarf on the apparent semi-major axis of the host star's orbit, yielding a value of approximately 109.6 μas. According to the Gaia official website[1], the expected precision in proper motion measurements, dependent on the G-band magnitude (see Table 5.1 for TOI-201), is about 5.24 μas for Gaia DR4 and 1.84 μas for Gaia DR5. Although these values are only estimates and do not account for all potential sources of uncertainty, they are significantly smaller than the expected astrometric signal, suggesting that future Gaia data releases will enable more precise measurements of TOI-201's proper motion and tighter constraints on the mass of the companion responsible for its PMa.

[1] https://www.cosmos.esa.int/web/gaia/science-performance

Chapter 6

Dynamical analysis

It may happen that small differences in the initial conditions produce very great ones in the final phenomena.
– Henri Poincaré

In Chapter 5, by combining the analysis of SPHERE observations, proper motion anomaly data, and radial velocity measurements, we derived the orbital parameters of the object responsible for the observed PMa, identified as a low-mass brown dwarf (hereafter denoted as TOI-201.03). The orbital parameters of the three components of the TOI-201 planetary system (the confirmed 53-day planet, the candidate 5.8-day planet, and the brown dwarf) are summarized in Table 6.1.

Object	**TOI-201.02**	**TOI-201 b**	**TOI-201.03**
M (M_J)	0.0201	$0.42^{+0.05}_{-0.03}$	$22.7^{+23}_{-8.4}$
a (AU)	0.06963 ± 0.00048	$0.30^{+0.02}_{-0.03}$	$6.8^{+2.0}_{-2.3}$
P	5.84924 ± 0.00003 d	52.97818 ± 0.00004 d	15.4 ± 7.1 yrs
i (°)	/	/	93^{+35}_{-39}
e	/	$0.28^{+0.06}_{-0.09}$	$0.45^{+0.35}_{-0.31}$

Table 6.1: Masses and orbital parameters of the objects comprising the TOI-201 planetary system.

The orbital parameters of TOI-201 b are taken from Hobson et al. [2021], while for TOI-201.02 the orbital period is taken from the NASA Exoplanet Archive[1], and the mass is estimated using the mass-radius relations provided by Otegi et al. [2020]. Due to the close proximity of TOI-201.02 to its host star, it is assumed to have undergone complete tidal circularization; therefore, its orbital

[1] https://exoplanetarchive.ipac.caltech.edu/overview/TOI-201

eccentricity has been fixed to zero. The orbital radius has been derived from the orbital period, assuming a circular orbit. Furthermore, the orbits of the three bodies are assumed to be coplanar. This assumption is supported by the fact that both TOI-201.02 and TOI-201 b are transiting planets, implying orbital inclinations close to 90°. Additionally, as derived in the previous chapter, the nominal inclination of TOI-201.03 is also close to 90°, justifying the approximation of coplanar orbits for all three bodies.
Once the orbital parameters have been derived, a detailed study of the system's dynamical properties can be performed, analyzing its stability and inferring the possible evolutionary pathways that led to the present-day configuration. In order to investigate the system's long-term stability for the nominal orbital parameters of its components, a numerical integration was carried out using the values listed in Table 6.1 as input to derive the time evolution of the orbital elements. The integration was performed with the 15th-order RADAU integrator (RA15; Everhart [1974]; Everhart [1985]), a numerical method similar to implicit Runge-Kutta schemes, specifically suited for orbital calculations. RA15 features rapid convergence and, thanks to its variable time step, is particularly well-adapted to handling close encounters between bodies. The use of a variable time step is also useful when dealing with highly eccentric orbits. In such cases, the gravitational potential varies rapidly, and adopting a variable time step ensures that the orbital elements are computed with sufficient accuracy throughout the integration. The system was integrated over a timespan of 75 Myr and remained stable throughout, as shown in Figure 6.1, which illustrates the time evolution of the semi-major axis and eccentricity of TOI-201.02.

6.1 Stability analysis

In order to explore the parameter space and identify the regions of stability and chaotic behavior, we carried out an analysis based on the computation of the MEGNO (Mean Exponential Growth factor of Nearby Orbits; Cincotta and Simó [2000]) chaos indicator. The MEGNO parameter quantifies how neighboring orbits, initially separated by infinitesimal displacements, diverge over time, serving as an indicator of chaotic behavior, with exponential divergence between nearby trajectories signaling chaos.
In order to introduce and define the MEGNO, let us consider an n-dimensional Hamiltonian $H(\boldsymbol{p}, \boldsymbol{q})$, where $\boldsymbol{p}, \boldsymbol{q} \in \mathbb{R}^n$. We examine two nearby initial conditions in phase space: $(\boldsymbol{p}(0), \boldsymbol{q}(0))$ and $(\boldsymbol{p}'(0), \boldsymbol{q}'(0)) = (\boldsymbol{p}(0) + \delta\boldsymbol{p}, \boldsymbol{q}(0) + \delta\boldsymbol{q})$, separated by an infinitesimal displacement $(\delta\boldsymbol{p}, \delta\boldsymbol{q})$. If the system exhibits exponential sensitivity to initial conditions, the separation vector evolves as $|\delta\boldsymbol{p}(t), \delta\boldsymbol{q}(t)| \approx |\delta\boldsymbol{p}(0), \delta\boldsymbol{q}(0)|e^{\lambda t}$, where λ is the Lyapunov characteristic number (LCN). The time evolution of this separation is governed by the variational equations, which take the form:

$$\delta\dot{q}_i = -\frac{\partial^2 H}{\partial p_j \partial q_i}(\boldsymbol{p}(t), \boldsymbol{q}(t))\delta p_j - \frac{\partial^2 H}{\partial q_j \partial q_i}(\boldsymbol{p}(t), \boldsymbol{q}(t))\delta q_j \ , \tag{6.1.1}$$

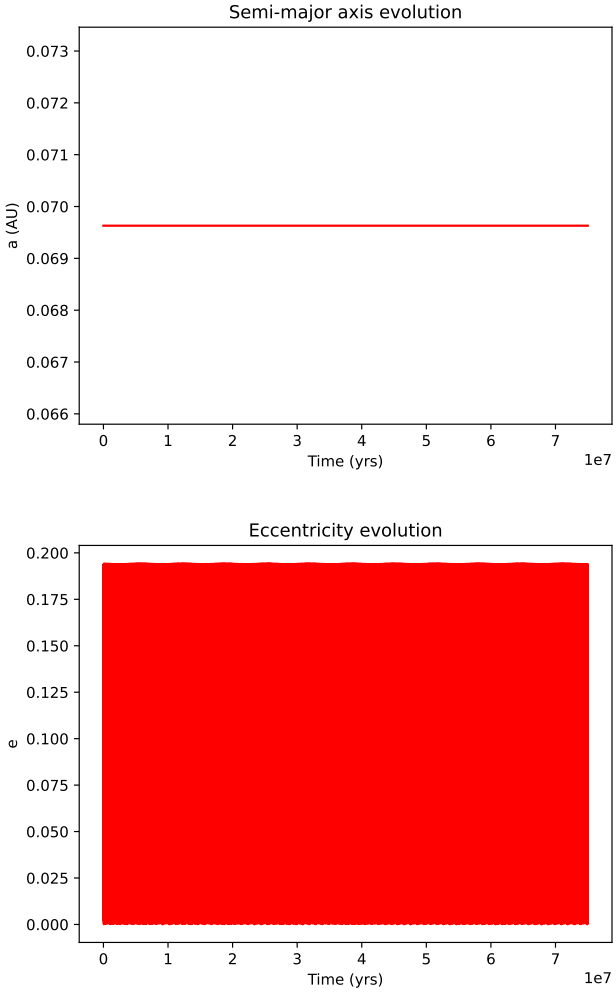

Figure 6.1: Results of the 75 Myr numerical simulation. *Top panel*: time evolution of the semi-major axis of TOI-201.02. *Bottom panel*: time evolution of its eccentricity.

$$\delta\dot{p}_i = -\frac{\partial^2 H}{\partial p_j \partial p_i}(\boldsymbol{p}(t), \boldsymbol{q}(t))\delta p_j - \frac{\partial^2 H}{\partial p_i \partial q_j}(\boldsymbol{p}(t), \boldsymbol{q}(t))\delta q_j \ . \tag{6.1.2}$$

We can now define the vector $\boldsymbol{\delta} = (\delta\boldsymbol{p},\ \delta\boldsymbol{q})$, whose norm is $\delta = ||\boldsymbol{\delta}||$, and the vector $\dot{\boldsymbol{\delta}} = (\delta\dot{\boldsymbol{p}}, \delta\dot{\boldsymbol{q}})$, whose norm is $\dot{\delta} = d\delta/dt = \dot{\boldsymbol{\delta}} \cdot \boldsymbol{\delta}/||\boldsymbol{\delta}||$. At this point, the LCN can be defined as:

$$\lambda = \lim_{t\to\infty} \frac{1}{t} \frac{\delta(t)}{\delta_0} \ , \tag{6.1.3}$$

where δ_0 is the norm of the vector $\boldsymbol{\delta}$ computed at time $t = 0$. The LCN measures the mean exponential rate of divergence of nearby orbits, and if it is larger than zero the orbit is indeed chaotic. As detailed in Benettin et al. [1980a] and Benettin et al. [1980b], a simple iterative procedure can be used to compute the LCN. After fixing a time T, the first step is to compute the growth factor $s_1 = \delta(T)/\delta_0$. Then, a new starting condition is computed at $t = T$, by setting $\delta\boldsymbol{p}(0) = \delta\boldsymbol{p}(T)/s_1$ and $\delta\boldsymbol{q}(0) = \delta\boldsymbol{q}(T)/s_1$, and the variational equations are solved again along T yielding s_2, and so on. After k iterations, the LCN is proven to be:

$$\lambda = \lim_{k\to\infty} \frac{1}{kT} \sum_{j=1}^{k} \ln s_j \ . \tag{6.1.4}$$

Finally, the MEGNO is defined as:

$$Y(t) = \frac{2}{t} \int_0^t \frac{\dot{\delta}(t')}{\delta(t')} t' dt' \ . \tag{6.1.5}$$

A time average of the MEGNO can also be defined, yielding:

$$\bar{Y}(t) = \frac{1}{t} \int_0^t Y(t') dt' \ . \tag{6.1.6}$$

The value of $\bar{Y}$ serves as an indicator of orbital stability. It can be demonstrated that, in the case of a stable periodic orbit, $\bar{Y}$ asymptotically approaches 2 as $t \to \infty$, and thus remains constant. Conversely, for a chaotic orbit, $\bar{Y}$ increases with time and, in the limit $t \to \infty$, follows the relation $\bar{Y} \sim \lambda t/2$. Figure 6.2 illustrates the time evolution of $\bar{Y}$ for both regular and chaotic orbital configurations. The upper panel illustrates the evolution of $\bar{Y}$ for a regular orbit, in both the stable case ("A" line) and the almost unstable periodic case ("B" line). In the stable configuration, the MEGNO rapidly converges to 2 from below, without exhibiting significant oscillations. In contrast, the unstable periodic orbit displays evident oscillations, with several local maxima of decreasing amplitude. In this case, the MEGNO assumes higher values compared to the stable case and ultimately approaches 2 from above. The lower panel shows the evolution of both Y (the noisy curve) and $\bar{Y}$ (the smooth curve). As discussed previously, both indicators, particularly $\bar{Y}$, reach large values and increase approximately linearly with time, consistent with chaotic orbital behavior.

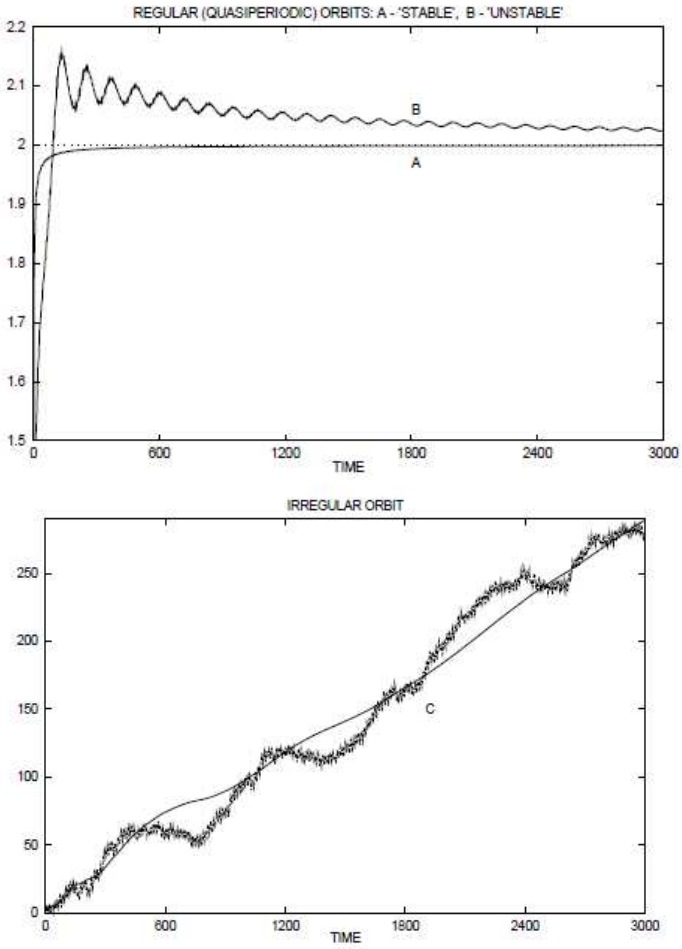

Figure 6.2: *Top panel*: $\bar{Y}$ evolution for a regular orbit, both in the stable ("A" curve) case and almost unstable ("B" curve) case. *Bottom panel*: Y (noisy curve) and $\bar{Y}$ (smooth curve) evolution for an irregular orbit. Image taken from Cincotta and Simó [2000].

To identify the regions of stability and chaotic behavior in the TOI-201 planetary system, a two-dimensional MEGNO map was computed by sampling a grid of approximately $4.8 \cdot 10^4$ orbital configurations and integrating the corresponding variational equations over $5 \cdot 10^4$ years. Specifically, the parameter space defined by the eccentricity of TOI-201.03, varying from 0.14 to 0.8, and its mass, ranging from 19 to 45 Jupiter masses, was explored, while all other orbital parameters were held fixed to their nominal values. The resulting MEGNO distribution is presented in Figure 6.3.

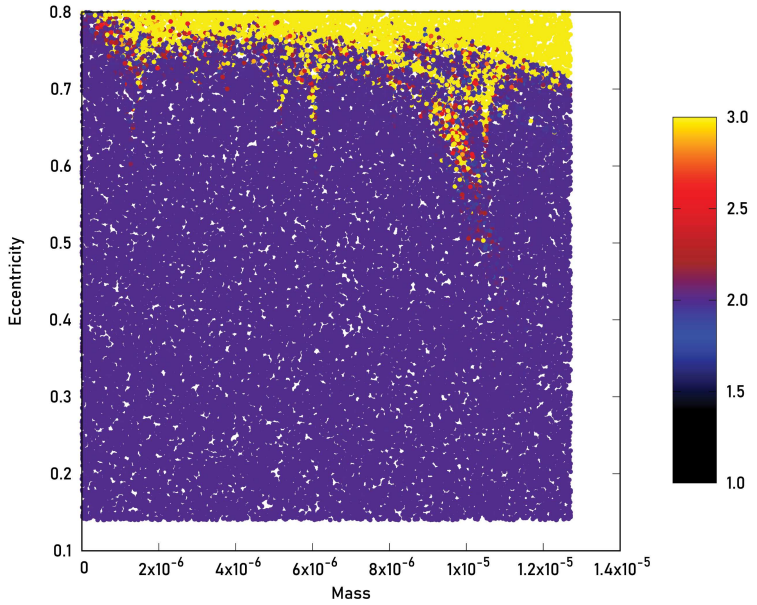

Figure 6.3: Two-dimensional MEGNO map for TOI-201, showing the dynamical behavior of the system as a function of TOI-201.03 eccentricity (vertical axis) and mass (horizontal axis, $M \cdot g$, with M expressed in $M_\odot$ and g in $AU^3 M_\odot^{-1} d^{-2}$). The color scale indicates the MEGNO values.

The blue regions in this map correspond to orbital configurations for which the MEGNO value is approximately 2, indicating regular and stable motion. In contrast, the red and especially yellow regions indicate MEGNO values greater than 2, characteristic of chaotic and thus unstable orbital configurations. As illustrated, stable orbits dominate the sampled parameter space, while instability arises primarily at higher eccentricities. Notably, the extent of the unstable region decreases with decreasing mass: for lower masses, even orbits with relatively high eccentricities, values that would lead to instability at higher masses, remain dynamically stable. Specifically, at higher masses, instability occurs for eccentricities exceeding approximately 0.72, whereas for decreasing mass the threshold shifts upward to around $e \gtrsim 0.75$–0.76. Besides this overall trend, isolated unstable configurations are also present at lower eccentricities, potentially linked to orbital resonances. Since the observed configuration of the system is dynamically stable, the unstable regions identified by the MEGNO analysis can be ruled out, thereby placing constraints on the mass and eccentricity of TOI-201.03. The nominal orbital parameters, $e = 0.45$ and $M = 22.7\ M_J$, fall well within the stable region of the diagram, supporting the hypothesis that the TOI-201 planetary system is indeed long-term stable.
To verify the reliability of the MEGNO-based stability analysis, several numerical simulations, using the code described in the previous section, were carried out using orbital parameters located within the identified instability region, in

order to confirm whether the system indeed exhibits unstable behavior under those conditions. The outcomes of two of these simulations, those considered the most representative, are briefly discussed below. In the first simulation, the mass of TOI-201.03 was set to 45 Jupiter masses and its eccentricity to 0.80, corresponding to the upper boundaries of the explored parameter space. Figure 6.4 shows the time evolution of the semi-major axis and eccentricity of TOI-201.02.

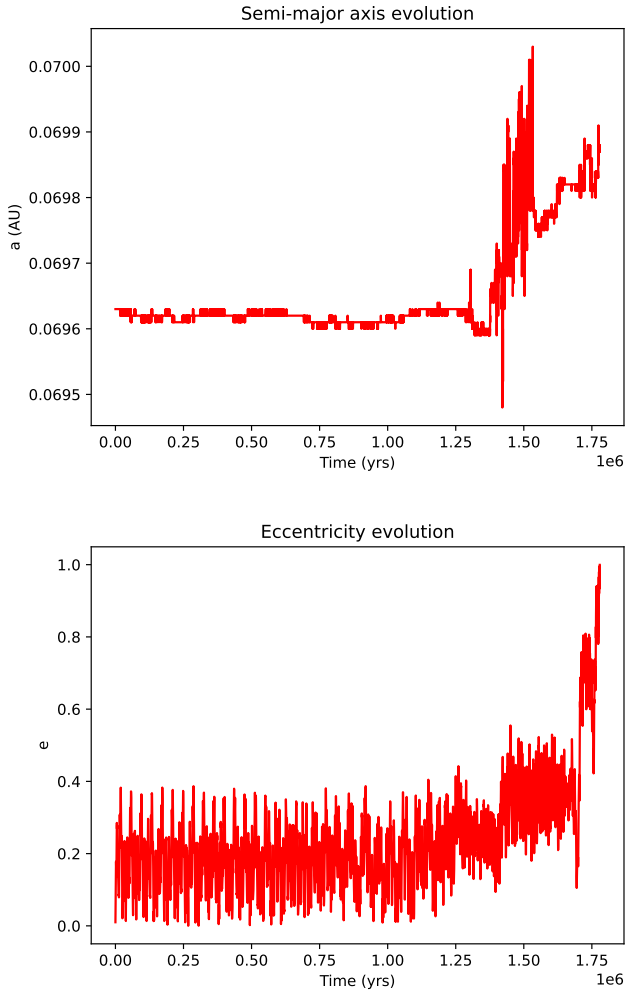

Figure 6.4: Results of the first 50 Myr numerical simulation in the instability regime. *Top panel*: time evolution of the semi-major axis of TOI-201.02. *Bottom panel*: time evolution of its eccentricity.

As expected, the system exhibits clear signs of chaotic behavior. Specifically, after less than 2 Myr, the eccentricity of the innermost planet increases uncontrollably, eventually reaching a value of one. The semi-major axis also displays irregular variations on comparable timescales. Although the numerical simulation was initially planned to run for 50 Myr, the chaotic evolution of the orbital elements, coupled with the premature termination of the integration, indicates that a close encounter between TOI-201.02 and TOI-201 b occurred, ultimately resulting in the ejection of TOI-201.02 from the system. This outcome is consistent with the MEGNO distribution shown in Figure 6.3, as the orbital parameters used in the simulation fall within the region associated with dynamical instability.
A second simulation was conducted using the same orbital parameters as in the previous case, with the only difference being a reduction in the mass of TOI-201.03 to 44 Jupiter masses. The results of this simulation are presented in Figure 6.5. The outcomes are similar to those of the previous simulation, with a close encounter, and the consequent ejection of the inner planet, occurring before 30 Myr. As in the previous case, the result is consistent with the MEGNO distribution, which correctly identifies this orbital configuration as unstable.

6.2 Final results

Overall, all our analyses support the conclusion that the TOI-201 planetary system is dynamically stable. The numerical simulation performed using the nominal orbital parameters listed in Table 6.1 shows no signs of instability. Furthermore, the stability analysis based on the MEGNO chaos indicator confirms that the present-day configuration corresponds to a regular, non-chaotic orbit. Nevertheless, several studies (e.g. Weidenschilling and Marzari [1996]; Chambers et al. [1996]) have shown that planetary systems composed of more than two planets, such as TOI-201, generally cannot achieve absolute long-term stability. However, the timescale over which orbital crossings may occur increases with the mutual separation between the bodies, implying that widely spaced configurations can remain dynamically stable over extended timescales, up to billions of years. If the system is sufficiently spaced to meet these stability criteria, it can be considered effectively stable over the long term. The mutual Hill radius between two bodies, taking into account eccentric orbits, can be defined as:

$$R_H^{(e)} = \left(\frac{m_1 + m_2}{3M_\star}\right)^{1/3} \frac{a_1(1-e_1) + a_2(1-e_2)}{2}\,, \tag{6.2.1}$$

with m_1, a_1 and e_1 representing the mass, semi-major axis and eccentricity of the first body (and analogously for the second body) and $M_\star$ the stellar mass. It is then possible to calculate the mutual separations between neighboring bodies expressed in mutual Hill radii. Using the nominal values for the dynamical and orbital parameters reported in Table 6.1, the resulting separations in mutual Hill radii (hereafter $\Delta_{i,j}$) are $\Delta_{1,2} \approx 34.04$ and $\Delta_{2,3} \approx 18.51$. In Chambers

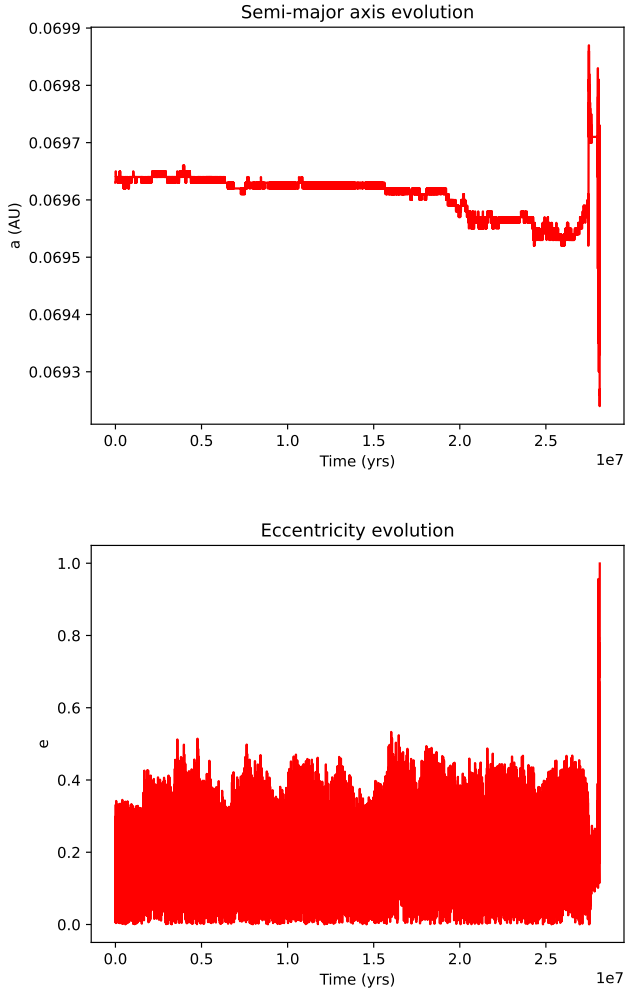

Figure 6.5: Results of the second 50 Myr numerical simulation in the instability regime. *Top panel*: time evolution of the semi-major axis of TOI-201.02. *Bottom panel*: time evolution of its eccentricity.

et al. [1996], a value of $\Delta = 10$ is used as a stability criterion for three-planet systems; thus, according to this study, the TOI-201 system is stable at least up to 10^8 years. However, this study assumes equal mass and equal mutual spacing for all bodies, so while it provides a useful first approximation, a more tailored approach is needed for precise constraints. The work by Marzari [2024] addresses stability in three-planet systems considering the more realistic case of bodies with different masses and separations. The results agree with previous studies, showing that the timescale for the onset of instability increases expo-

nentially with mutual spacing. In particular, for $\Delta \sim 7$, instability is predicted to occur on timescales of order $10^8 - 10^9$ years. Given an almost exponential relationship between Δ and the instability timescale, and the fact that the mutual spacings in the TOI-201 system are much larger than 7, this suggests that the system remains stable over timescales exceeding $\sim 10^{10}$ years. In this work, we performed a numerical simulation of the system over 75 Myr, which showed no signs of instability. Therefore, based solely on our numerical analysis, we conclude that the TOI-201 system appears stable for timescales of at least 75 Myr. Due to practical and computational limitations, longer simulations were not feasible; however, according to the studies mentioned earlier, the system can be considered long-term stable.

The last point to address concerns the evolutionary path that led the TOI-201 planetary system to its present-day configuration. The system exhibits a peculiar architecture, with one planet located very close to the host star, which eccentricity can be considered zero due to tidal circularization, and two outer companions with significantly eccentric orbits. This configuration is consistent with a planet-planet scattering scenario that may have occurred in the early stages of the system's evolution. After the dissipation of the protoplanetary disk, and depending on the initial conditions such as orbital separations, planetary masses, and eccentricities, the system may have entered a phase of dynamical instability. During this phase, close encounters and orbit crossings can lead to increased eccentricities, ultimately resulting in the ejection of one or more planets and the stabilization of the remaining bodies on eccentric orbits. This process may also explain the presence of the innermost planet. One or more planets scattered onto highly eccentric orbits may have reached periastron distances small enough for tidal forces to circularize their orbits, which is potentially the origin of TOI-201.02. In contrast, the surviving outer planets, whose periastron distances remained too large for tidal circularization to be effective, preserved their eccentric orbits. This is the case for TOI-201 b and TOI-201.03, with eccentricities of $0.28^{+0.06}_{-0.09}$ and $0.45^{+0.35}_{-0.31}$, respectively. Additionally, planet-planet scattering often results in slight inward migration of the surviving planets due to conservation of energy, implying that TOI-201 b and TOI-201.03 likely formed at larger distances from the star than where they are observed today. Therefore, if this hypothesis is correct, the TOI-201 system originally hosted more than three planetary bodies. The onset of dynamical instability following disk dissipation, and the consequent ejection of one or more planets, would have shaped the system into its present-day configuration. However, since the orbits of the three bodies are assumed to be coplanar, and given that planetary orbits just after disk dissipation are also expected to be coplanar, the period of dynamical instability and the subsequent planet-planet scattering should not have significantly altered the orbital inclinations, in order to be consistent with the current configuration. Although planet–planet scattering typically results in changes to the orbital inclinations, this is not always the case. For instance, if one planet is rapidly ejected from the system shortly after the onset of instability, the interaction timescale may be too short to induce significant perturbations, allowing the remaining planets to retain orbital configurations close to their ini-

tial conditions.
Another possible explanation for the current system configuration could arise from the effect of secular perturbations. As reported in Table 6.1, the eccentricity of TOI-201.03 spans a wide range of values, from 0.14 to 0.80 within the 1-σ interval. Our numerical simulations indicate that, if the eccentricity of the brown dwarf lies in the upper part of this range, around 0.7, near the boundary of the stability region, it could account for the observed eccentricity of TOI-201 b. In such a scenario, TOI-201 b undergoes secular oscillations in eccentricity, reaching a maximum value of approximately 0.27-0.28, close to its current nominal value. This behavior is illustrated in Figure 6.6, which shows the evolution of the eccentricity of TOI-201 b over a timespan of 10^5 years. The plot highlights the eccentricity oscillations, which occur with a period of approximately 10^4 years.

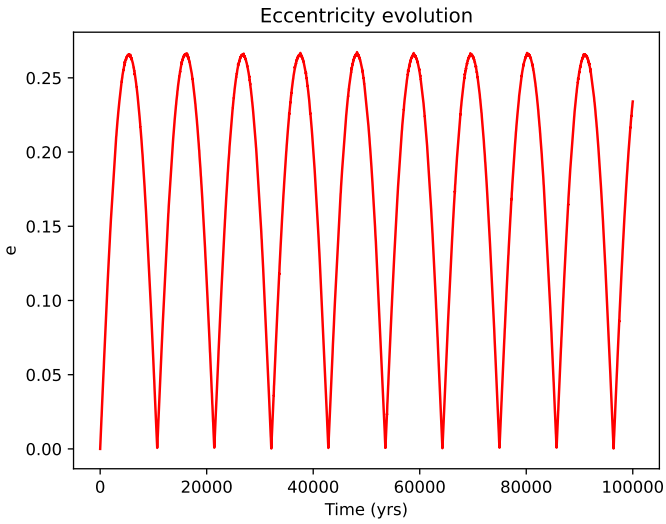

Figure 6.6: Time evolution of the eccentricity of TOI-201 b over 10^5 years, showing periodic oscillations with a maximum value of ~ 0.27. The eccentricity of TOI-201.03 was fixed at 0.75.

Bibliography

B. Addison et al. Minerva-Australis I: Design, Commissioning, & First Photometric Results. *Publications of the Astronomical Society of the Pacific*, 131: 115003, 2019. URL https://doi.org/10.1088/1538-3873/ab03aa.

E. Agol and D. Fabrycky. Transit Timing and Duration Variations for the Discovery and Characterization of Exoplanets. *Handbook of Exoplanets*, 2017. URL https://doi.org/10.48550/arXiv.1706.09849.

E. Agol et al. On detecting terrestrial planets with timing of giant planet transits. *Monthly Notices of the Royal Astronomical Society*, 359:567, 2005. URL https://doi.org/10.1111/j.1365-2966.2005.08922.x.

F. Allard et al. The Limiting Effects of Dust in Brown Dwarf Model Atmospheres. *The Astrophysical Journal*, 556:357, 2001. URL https://doi.org/10.1086/321547.

J. Antichi et al. BIGRE: A Low Cross-Talk Integral Field Unit Tailored for Extrasolar Planets Imaging Spectroscopy. *The Astrophysical Journal*, 695: 1042, 2009. URL https://doi.org/10.1088/0004-637X/695/2/1042.

S. Ataiee et al. How much does turbulence change the pebble isolation mass for planet formation? *Astronomy and Astrophysics*, 615:A110, 2018. URL https://doi.org/10.1051/0004-6361/201732026.

D. Barbato et al. Revised estimates of the frequency of Earth-like planets in the Kepler field. *Proceedings IAU Symposium*, 348, 2018a. URL https://doi.org/10.48550/arXiv.1811.08249.

D. Barbato et al. Exploring the realm of scaled solar system analogues with HARPS. *Astronomy and Astrophysics*, 615:A175, 2018b. URL https://doi.org/10.1051/0004-6361/201832791.

D. Barbato et al. The GAPS Programme with HARPS-N at TNG XVIII. Two new giant planets around the metal-poor stars HD 220197 and HD 233832. *Astronomy and Astrophysics*, 621:A110, 2019. URL https://doi.org/10.1051/0004-6361/201834305.

V. Batista. Finding Planets via Gravitational Microlensing. *Handbook of Exoplanets*, 2018. URL https://doi.org/10.1007/978-3-319-55333-7_120.

J. M. Beckers. Adaptive Optics for Astronomy: Principles, Performance, and Applications. *Annual Review of Astronomy and Astrophysics*, 31:13, 1993. URL https://ui.adsabs.harvard.edu/abs/1993ARA%26A..31...13B/abstract.

G. Benettin et al. Lyapunov Characteristic Exponents for smooth dynamical systems and for hamiltonian systems; a method for computing all of them. Part 1: Theory. *Meccanica*, 15:9, 1980a. URL https://doi.org/10.1007/BF02128236.

G. Benettin et al. Lyapunov Characteristic Exponents for smooth dynamical systems and for hamiltonian systems; A method for computing all of them. Part 2: Numerical application. *Meccanica*, 15:21, 1980b. URL https://doi.org/10.1007/BF02128237.

G. J. Bergsten et al. The Demographics of Kepler's Earths and Super-Earths into the Habitable Zone. *The Astrophysical Journal*, 164:190, 2022. URL https://doi.org/10.3847/1538-3881/ac8fea.

F. W. Bessel. On the variations of the proper motions of Procyon and Sirius. *Monthly Notices of the Royal Astronomical Society*, 6:136, 1844. URL https://ui.adsabs.harvard.edu/abs/1844MonthlyNoticesoftheRoyalAstronomicalSociety...6R.136B/abstract.

J.-L. Beuzit et al. SPHERE: the exoplanet imager for the Very Large Telescope. *Astronomy and Astrophysics*, 631:A155, 2019. URL https://doi.org/10.1051/0004-6361/201935251.

J. Binney and S. Tremaine. *Galactic Dynamics: Second Edition*. Princeton University Press, 2008. URL https://press.princeton.edu/books/paperback/9780691130279/galactic-dynamics.

A. Boccaletti et al. The Four-Quadrant Phase Mask Coronagraph. IV. First Light at the Very Large Telescope. *Publications of the Astronomical Society of the Pacific*, 116:1061, 2004. URL https://doi.org/10.1086/425735.

A. J. Bohn et al. Two Directly Imaged, Wide-orbit Giant Planets around the Young, Solar Analog TYC 8998-760-1. *The Astrophysical Journal Letters*, 898:L16, 2020. URL https://doi.org/10.3847/2041-8213/aba27e.

I. A. Bond et al. Real-time difference imaging analysis of MOA Galactic bulge observations during 2000. *Monthly Notices of the Royal Astronomical Society*, 327:868, 2001. URL https://doi.org/10.1046/j.1365-8711.2001.04776.x.

I. A. Bond et al. OGLE 2003–BLG–235/MOA 2003–BLG–53: A planetary microlensing event. *The Astrophysical Journal*, 606:L155, 2004. URL https://doi.org/10.1086/420928.

W. J. Borucki and A. L. Summers. The photometric method of detecting other planetary systems. *Icarus*, 58:121, 1984. URL https://doi.org/10.1016/0019-1035(84)90102-7.

W. J. Borucki et al. The Kepler Mission: A Mission To Determine The Frequency Of Inner Planets Near The Habitable Zone For A Wide Range Of Stars. *ASP Conference Series*, 119:153, 1997. URL https://articles.adsabs.harvard.edu/pdf/1997ASPC..119..153B.

W. J. Borucki et al. Characteristics of planetary candidates observed by Kepler, II: Analysis of the first four months of data. *The Astrophysical Journal*, 736: 19, 2011. URL https://doi.org/10.1088/0004-637X/736/1/19.

A. P. Boss. Giant planet formation by gravitational instability. *Science*, 276: 1836, 1997. URL https://doi.org/10.1126/science.276.5320.1836.

T. D. Brandt. The Hipparcos-Gaia Catalog of Accelerations. *The Astrophysical Journal Supplement Series*, 239:31, 2018. URL https://doi.org/10.3847/1538-4365/aaec06.

T. D. Brandt. The Hipparcos-Gaia Catalog of Accelerations: Gaia EDR3 Edition. *The Astrophysical Journal Supplement Series*, 254:42, 2021. URL https://doi.org/10.3847/1538-4365/abf93c.

T. D. Brandt et al. orvara: An Efficient Code to Fit Orbits Using Radial Velocity, Absolute, and/or Relative Astrometry. *The Astronomical Journal*, 162:186, 2021. URL https://doi.org/10.3847/1538-3881/ac042e.

R. Burn and C. Mordasini. Planetary population synthesis. *eprint arXiv*, 2024. URL https://doi.org/10.48550/arXiv.2410.00093.

R. Burn et al. A radius valley between migrated steam worlds and evaporated rocky cores. *Nature Astronomy*, 8:463, 2024. URL https://doi.org/10.48550/arXiv.2401.04380.

A. Burrows and J. Liebert. The science of brown dwarfs. *Reviews of Modern Physics*, 65:301, 1993. URL https://doi.org/10.1103/RevModPhys.65.301.

A. Burrows et al. The theory of brown dwarfs and extrasolar giant planets. *Reviews of Modern Physics*, 73:719, 2001. URL https://doi.org/10.1103/RevModPhys.73.719.

J. E. Chambers et al. The Stability of Multi-Planet Systems. *Icarus*, 119:261, 1996. URL https://doi.org/10.1006/icar.1996.0019.

D. Charbonneau et al. Detection of Planetary Transits Across a Sun-like Star. *The Astrophysical Journal*, 529:L45, 2000. URL https://doi.org/10.1086/312457.

G. Chauvin et al. SHINE, The SpHere INfrared survey for Exoplanets. *Proceedings of the Annual meeting of the French Society of Astronomy and Astrophysics*, page 331, 2017a. URL https://sf2a.eu/proceedings/2017/2017sf2a.conf..0331C.pdf.

G. Chauvin et al. Discovery of a warm, dusty giant planet around HIP 65426. *Astronomy and Astrophysics*, 605:L9, 2017b. URL https://doi.org/10.1051/0004-6361/201731152.

A. Cheetham et al. Discovery of a brown dwarf companion to the star HIP 64892. *Astronomy and Astrophysics*, 615:A160, 2018. URL https://doi.org/10.1051/0004-6361/201832650.

D.-C. Chen et al. Constraints on the formation history and composition of Kepler planets from their distribution of orbital period ratios. *Astronomy and Astrophysics*, 687:A25, 2024. URL https://doi.org/10.1051/0004-6361/202449371.

J. Chilcote et al. GPI 2.0: upgrading the Gemini Planet Imager. *SPIE*, 11447: 114471S, 2020. URL https://doi.org/10.1117/12.2562578.

A. Chomez et al. The SPHERE infrared survey for exoplanets (SHINE). V. Complete observations, data reduction and analysis, detection performances, and final results. *arXiv*, 2025. URL https://doi.org/10.48550/arXiv.2501.12002.

P. M. Cincotta and C. Simó. Simple tools to study global dynamics in non-axisymmetric galactic potentials - I. *Astronomy and Astrophysics Supplement Series*, 147:205, 2000. URL https://doi.org/10.1051/aas:2000108.

R. Claudi and D. Mesa. High-Contrast Imaging: Hide and Seek with Exoplanets. *Galaxies*, 13:3, 2025. URL https://doi.org/10.3390/galaxies13010003.

R. U. Claudi et al. SPHERE IFS: the spectro differential imager of the VLT for exoplanets search. *SPIE Conf. Serv.*, 7014:70143E, 2008. URL https://doi.org/10.1117/12.788366.

A. Cumming et al. The Keck Planet Search: Detectability and the Minimum Mass and Orbital Period Distribution of Extrasolar Planets. *Publications of the Astronomical Society of the Pacific*, 120:531, 2008. URL https://doi.org/10.1086/588487.

T. Currie et al. Direct Imaging and Spectroscopy of Extrasolar Planets. *Protostars and Planets VII*, 2023. URL https://doi.org/10.48550/arXiv.2205.05696.

R. Davies et al. The Enhanced Resolution Imager and Spectrograph for the VLT. *Astronomy and Astrophysics*, 674:A207, 2023. URL https://doi.org/10.1051/0004-6361/202346559.

M. Deleuil et al. Planets, candidates, and binaries from the CoRoT/Exoplanet programme: the CoRoT transit catalogue. *Astronomy and Astrophysics*, 619: A97, 2018. URL https://doi.org/10.1051/0004-6361/201731068.

K. Dohlen et al. The infra-red dual imaging and spectrograph for SPHERE: design and performance. *SPIE Conf. Serv.*, 7014:70143L, 2008. URL https://doi.org/10.1117/12.789786.

S. Dong et al. LAMOST telescope reveals that Neptunian cousins of hot Jupiters are mostly single offspring of stars that are rich in heavy elements. *Proceedings of the National Academy of Sciences*, 115:266, 2018. URL https://doi.org/10.1073/pnas.1711406115.

J. Drazkowska et al. Planet Formation Theory in the Era of ALMA and Kepler: from Pebbles to Exoplanets. *Protostars and Planets VII*, 2023. URL https://doi.org/10.48550/arXiv.2203.09759.

A. Emsenhuber, C. Mordasini, and R. Burn. Planetary population synthesis and the emergence of four classes of planetary system architectures. *Eur. Phys. J. Plus*, 138:181, 2023. URL https://doi.org/10.1140/epjp/s13360-023-03784-x.

A. Emsenhuber et al. The New Generation Planetary Population Synthesis (NGPPS) I. Bern global model of planet formation and evolution, model tests, and emerging planetary systems. *Astronomy and Astrophysics*, 656: A69, 2021. URL https://doi.org/10.1051/0004-6361/202038553.

C. Espaillat et al. An Observational Perspective of Transitional Disks. *Protostars and Planets VI*, page 497, 2014. URL https://doi.org/10.48550/arXiv.1402.7103.

E. Everhart. Implicit single-sequence methods for integrating orbits. *Celestial Mechanics*, 10:35, 1974. URL https://doi.org/10.1007/BF01261877.

E. Everhart. An efficient integrator that uses Gauss-Radau spacings. *Dynamics of Comets: Their Origin and Evolution*, 115, 1985. URL https://doi.org/10.1007/978-94-009-5400-7_17.

J. Farinato et al. SHARK-NIR, ready to "swim" in the LBT Northern Hemisphere "ocean". *SPIE*, 12185:1218522, 2022. URL https://doi.org/10.1117/12.2630083.

D. A. Fischer and J. Valenti. The Planet-Metallicity Correlation. *The Astrophysical Journal*, 622:1102, 2005. URL https://doi.org/10.1086/428383.

K. B. Follette. An Introduction to High Contrast Differential Imaging of Exoplanets and Disks. *Publications of the Astronomical Society of the Pacific*, 135:093001, 2023. URL https://doi.org/10.1088/1538-3873/aceb31.

R. Foy and A. Labeyrie. Feasibility of adaptive telescope with laser probe. *Astronomy and Astrophysics*, 152:L29, 1985. URL https://articles.adsabs.harvard.edu/pdf/1985A%26A...152L..29F.

F. Fressin et al. The False Positive Rate of Kepler and the Occurrence of Planets. *The Astrophysical Journal*, 766:81, 2013. URL https://doi.org/10.1088/0004-637X/766/2/81.

B. J. Fulton et al. The California-Kepler Survey. III. A Gap in the Radius Distribution of Small Planets. *The Astronomical Journal*, 154:109, 2017. URL https://doi.org/10.3847/1538-3881/aa80eb.

Gaia Collaboration et al. The Gaia mission. *Astronomy and Astrophysics*, 595: A1, 2016. URL https://doi.org/10.1051/0004-6361/201629272.

Gaia Collaboration et al. Gaia Early Data Release 3. Summary of the contents and survey properties. *Astronomy and Astrophysics*, 650:C3, 2021. URL https://doi.org/10.1051/0004-6361/202039657e.

Gaia Collaboration et al. Gaia Data Release 3. Summary of the content and survey properties. *Astronomy and Astrophysics*, 674:A1, 2023. URL https://doi.org/10.1051/0004-6361/202243940.

E. Gaidos et al. They are small worlds after all: revised properties of Kepler M dwarf stars and their planets. *Monthly Notices of the Royal Astronomical Society*, 457:2877, 2016. URL https://doi.org/10.1093/mnras/stw097.

J. P. Gardner et al. The James Webb Space Telescope. *Space Science Reviews*, 123:485, 2006. URL https://doi.org/10.1007/s11214-006-8315-7.

M. Gillon et al. Temperate Earth-sized planets transiting a nearby ultracool dwarf star. *Nature*, 533:221, 2016. URL https://doi.org/10.1038/nature17448.

S. Y. Haffert et al. Two accreting protoplanets around the young star PDS 70. *Nature Astronomy*, 3:749, 2019. URL https://doi.org/10.1038/s41550-019-0780-5.

L. Hartmann et al. Accretion and the Evolution of T Tauri Disks. *The Astrophysical Journal*, 495:385, 1998. URL https://doi.org/10.1086/305277.

C. Hayashi. Structure of the Solar Nebula, Growth and Decay of Magnetic Fields and Effects of Magnetic and Turbulent Viscosities on the Nebula. *Progress of Theoretical Physics Supplement*, 70:35, 1981. URL https://doi.org/10.1143/PTPS.70.35.

R. Helled et al. Giant Planet Formation, Evolution, and Internal Structure. *Protostars and Planets VI*, 2013. URL https://doi.org/10.48550/arXiv.1311.1142.

M. J. Hobson et al. A Transiting Warm Giant Planet around the Young Active Star TOI-201. *The Astronomical Journal*, 161:235, 2021. URL https://doi.org/10.3847/1538-3881/abeaa1.

V. Hoffmann et al. Stochasticity and predictability in terrestrial planet formation. *Monthly Notices of the Royal Astronomical Society*, 465:2170, 2017. URL https://doi.org/10.1093/mnras/stw2856.

M. J. Holman and N. W. Murray. The Use of Transit Timing to Detect Terrestrial-Mass Extrasolar Planets. *Science*, 307:1288, 2005. URL https://doi.org/10.1126/science.1107822.

A. W. Howard et al. The Occurrence and Mass Distribution of Close-in Super-Earths, Neptunes, and Jupiters. *Science*, 330:653, 2010. URL https://doi.org/10.1126/science.1194854.

A. W. Howard et al. Planet Occurrence within 0.25 AU of Solar-type Stars from Kepler. *The Astrophysical Journal Supplement*, 201:15, 2012. URL https://doi.org/10.1088/0067-0049/201/2/15.

R. Hueso and T. Guillot. Evolution of protoplanetary disks: constraints from DM Tauri and GM Aurigae. *Astronomy and Astrophysics*, 442:703, 2005. URL https://doi.org/10.1051/0004-6361%3A20041905.

A. Izidoro and S. N. Raymond. Formation of Terrestrial Planets. *arXiv:astro-ph*, 2018. URL https://doi.org/10.48550/arXiv.1803.08830.

A. Kaufer et al. Commissioning FEROS, the new high-resolution spectrograph at La-Silla. *The Messenger*, 95:8, 1999. URL https://ui.adsabs.harvard.edu/abs/1999Msngr..95....8K/abstract.

M. A. Kenworthy et al. First On-Sky High-Contrast Imaging with an Apodizing Phase Plate. *The Astrophysical Journal*, 660:762, 2007. URL https://doi.org/10.1086/513596.

M. Keppler et al. Discovery of a planetary-mass companion within the gap of the transition disk around PDS 70. *Astronomy and Astrophysics*, 617:A44, 2018. URL https://doi.org/10.1051/0004-6361/201832957.

P. Kervella et al. Stellar and substellar companions of nearby stars from Gaia DR2. Binarity from proper motion anomaly. *Astronomy and Astrophysics*, 623:A72, 2019. URL https://doi.org/10.1051/0004-6361/201834371.

P. Kervella et al. Stellar and substellar companions from Gaia EDR3. Proper-motion anomaly and resolved common proper-motion pairs. *Astronomy and Astrophysics*, 657:A7, 2022. URL https://doi.org/10.1051/0004-6361/202142146.

S. Kiefer et al. Spectral and angular differential imaging with SPHERE/IFS. Assessing the performance of various PCA-based approaches to PSF subtraction. *Astronomy and Astrophysics*, 652:A33, 2021. URL https://doi.org/10.1051/0004-6361/202140285.

D. Kipping. An Independent Analysis of the Six Recently Claimed Exomoon Candidates. *The Astrophysical Journal Letters*, 900:L44, 2020. URL https://doi.org/10.48550/arXiv.2008.03613.

D. M. Kipping. Parametrizing the exoplanet eccentricity distribution with the Beta distribution. *Monthly Notices of the Royal Astronomical Society*, 434: L51, 2013. URL https://doi.org/10.1093/mnrasl/slt075.

M. Kramer. Pulsar Timing as an Exoplanet Discovery Method. *Handbook of Exoplanets*, 2018. URL https://doi.org/10.1007/978-3-319-55333-7_5.

G. Lacedelli et al. An unusually low density ultra-short period super-Earth and three mini-Neptunes around the old star TOI-561. *Monthly Notices of the Royal Astronomical Society*, 501:4148, 2021. URL https://doi.org/10.1093/mnras/staa3728.

M. Langlois et al. High contrast imaging with IRDIS near infrared polarimeter. *SPIE*, 7735:77352U, 2010. URL https://doi.org/10.1117/12.857221.

L. Lindegren et al. Gaia Early Data Release 3. The astrometric solution. *Astronomy and Astrophysics*, 649:A2, 2021. URL https://doi.org/10.1051/0004-6361/202039709.

M. Lingam, I. Ginsburg, and A. Loeb. Prospects for Life on Temperate Planets around Brown Dwarfs. *The Astrophysical Journal*, 888:102, 2020. URL https://iopscience.iop.org/article/10.3847/1538-4357/ab5b13.

J. J. Lissauer et al. Models of Jupiter's growth incorporating thermal and hydrodynamic constraints. *Icarus*, 199:338, 2009. URL https://doi.org/10.1016/j.icarus.2008.10.004.

Y. Lithwick and Y. Wu. Secular chaos and its application to Mercury, hot Jupiters, and the organization of planetary systems. *Proceedings of the National Academy of Sciences*, 111:12610, 2014. URL https://doi.org/10.1073/pnas.1308261110.

B. Lyot. The study of the solar corona and prominences without eclipses. *Monthly Notices of the Royal Astronomical Society*, 99:580, 1939. URL https://doi.org/10.1093/mnras/99.8.580.

B. Macintosh et al. First light of the Gemini Planet Imager. *Proceedings of the National Academy of Sciences*, 111:12661, 2014. URL https://doi.org/10.1073/pnas.1304215111.

V. V. Makarov, N. Zacharias, and G. S. Hennessy. Common Proper Motion Companions to Nearby Stars: Ages and Evolution. *The Astrophysical Journal*, 687:566, 2008. URL https://doi.org/10.1086/591638.

L. Malavolta et al. The GAPS programme with HARPS-N at TNG. XI. Pr 0211 in M 44: the first multi-planet system in an open cluster. *Astronomy and Astrophysics*, 588:A118, 2016. URL https://doi.org/10.1051/0004-6361/201527933.

L. Malavolta et al. An Ultra-short Period Rocky Super-Earth with a Secondary Eclipse and a Neptune-like Companion around K2-141. *The Astronomical Journal*, 155:107, 2018. URL https://doi.org/10.3847/1538-3881/aaa5b5.

F. Malbet and A. Sozzetti. Astrometry as an Exoplanet Discovery Method. *Handbook of Exoplanets*, 2018. URL https://doi.org/10.1007/978-3-319-55333-7_196.

C. Marois et al. Angular Differential Imaging: A Powerful High-Contrast Imaging Technique. *The Astrophysical Journal*, 641:556, 2006. URL https://doi.org/10.1086/500401.

F. Marzari. *Planetary Astrophysics*. Cambridge Scholars Publishing, 2023.

F. Marzari. Planet–planet scattering in systems of multiple planets of unequal mass. *Monthly Notices of the Royal Astronomical Society*, 536:422, 2024. URL https://doi.org/10.1093/mnras/stae2602.

M. Mattioli et al. SHARK-VIS the LBT high contrast imager at visible wavelengths. *SPIE*, 10702:107024F, 2018. URL https://doi.org/10.1117/12.2312591.

M. Mayor and D. Queloz. A Jupiter-mass companion to a solar-type star. *Nature*, 378:355, 1995. URL https://dx.doi.org/10.1038%2F378355a0.

M. Mayor et al. Setting New Standards with HARPS. *The Messenger*, 114:20, 2003. URL https://ui.adsabs.harvard.edu/abs/2003Msngr.114...20M/abstract.

M. Mayor et al. The HARPS search for southern extra-solar planets XXXIV. Occurrence, mass distribution and orbital properties of super-Earths and Neptune-mass planets. *eprint arXiv*, 2011. URL https://doi.org/10.48550/arXiv.1109.2497.

T. Mazeh, T. Holczer, and S. Faigler. Dearth of short-period Neptunian exoplanets: A desert in period-mass and period-radius planes. *Astronomy and Astrophysics*, 589:A75, 2016. URL https://doi.org/10.1051/0004-6361/201528065.

I. S. McLean. *Electronic Imaging in Astronomy: Detectors and Instrumentation*. Wiley, 1997.

F. Merkle et al. Succesful tests of adaptive optics. *Messenger*, 58: 1, 1989. URL https://www.eso.org/sci/publications/messenger/archive/no.58-dec89/messenger-no58-1-4.pdf.

L. Mishra et al. Framework for the architecture of exoplanetary systems I. Four classes of planetary system architecture. *Astronomy and Astrophysics*, 670: A68, 2023. URL https://doi.org/10.1051/0004-6361/202243751.

C. Mordasini and R. Burn. Planet formation – observational constraints, physical processes, and compositional patterns. *Reviews in Mineralogy and Geochemistry*, 90, 2024. URL https://doi.org/10.48550/arXiv.2404.15555.

C. Mordasini et al. Theory of planet formation. *eprint arXiv*, 2010. URL https://doi.org/10.48550/arXiv.1012.5281.

A. Mortier et al. On the functional form of the metallicity-giant planet correlation. *Astronomy and Astrophysics*, 551:A112, 2013. URL https://doi.org/10.1051/0004-6361/201220707.

P. S. Muirhead et al. Characterizing the Cool KOIs. III. KOI 961: A Small Star with Large Proper Motion and Three Small Planets. *The Astrophysical Journal*, 747:144, 2012. URL https://doi.org/10.1088/0004-637X/747/2/144.

U. Munari et al. APASS Landolt-Sloan BVgri Photometry of RAVE Stars. I. Data, Effective Temperatures, and Reddenings. *The Astronomical Journal*, 148:81, 2014. URL https://doi.org/10.1088/0004-6256/148/5/81.

S. Nayakshin. Dawes Review 7. The tidal downsizing hypothesis of planet formation. *PASA*, 2016. URL https://doi.org/10.1017/pasa.2016.55.

R. P. Nelson. Planetary Migration in Protoplanetary Disks. *Handbook of Exoplanets*, 2018. URL https://doi.org/10.1007/978-3-319-55333-7_139.

M. Neveu-VanMalle et al. Hot Jupiters with relatives: discovery of additional planets in orbit around WASP-41 and WASP-47. *Astronomy and Astrophysics*, 586:A93, 2016. URL https://doi.org/10.1051/0004-6361/201526965.

B. R. Oppenheimer and S. Hinkley. High-Contrast Observations in Optical and Infrared Astronomy. *Annual Review of Astronomy and Astrophysics*, 47:253, 2009. URL https://doi.org/10.1146/annurev-astro-082708-101717.

J. F. Otegi et al. Revisited mass-radius relations for exoplanets below 120 Earth masses. *Astronomy and Astrophysics*, 634:A43, 2020. URL https://doi.org/10.1051/0004-6361/201936482.

J. C. B. Papaloizou and C. Terquem. Planet formation and migration. *Reports on Progress in Physics*, 69:119, 2005. URL https://doi.org/10.1088/0034-4885/69/1/R03.

A. Pavlov et al. Data Reduction and Handling for SPHERE. *Proc. SPIE*, 7019: 701939, 2008. URL https://doi.org/10.1117/12.789110.

D. Pearson et al. NIX, the imager for ERIS: the AO instrument for the VLT. *SPIE*, 9908:99083F, 2016. URL https://doi.org/10.1117/12.2234074.

K. Pearson. On lines and planes of closest fit to systems of points in space. *Philosophical Magazine*, Series 6, vol. 2, no. 11:559, 1901. URL http://www.stats.org.uk/pca/Pearson1901.pdf.

M. J. Pecaut and E. E. Mamajek. Intrinsic Colors, Temperatures, and Bolometric Corrections of Pre-main-sequence Stars. *The Astrophysical Journal Supplement*, 208:9, 2013. URL https://doi.org/10.1088/0067-0049/208/1/9.

M. Perryman. The history of astrometry. *The European Physical Journal H*, 37:745, 2012. URL http://dx.doi.org/10.1140/epjh/e2012-30039-4.

M. Perryman. *The Exoplanet Handbook*. Cambridge University Press, 2018.

M. Perryman et al. The HIPPARCOS Catalogue. *Astronomy and Astrophysics*, 323:L49, 1997. URL https://articles.adsabs.harvard.edu/pdf/1997A%26A...323L..49P.

E. A. Petigura et al. Prevalence of Earth-size planets orbiting Sun-like stars. *Proceedings of the National Academy of Sciences*, 110:48, 2013. URL https://doi.org/10.1073/pnas.1319909110.

A. A. A. Piette and N. Madhusudhan. On the Temperature Profiles and Emission Spectra of Mini-Neptune Atmospheres. *The American Astronomical Society*, 904:154, 2020. URL https://doi.org/10.3847/1538-4357/abbfb1.

E. Pinna et al. Bringing SOUL on sky. *arXiv*, 2021. URL https://doi.org/10.48550/arXiv.2101.07091.

E. Plávalová and A. Rosaev. Classifications for Exoplanet and Exoplanetary Systems - Could it be developed? I. Exoplanet classification. *arXiv:astro-ph*, 2024. URL https://doi.org/10.48550/arXiv.2409.09666.

J. B. Pollack et al. Formation of the Giant Planets by Concurrent Accretion of Solids and Gas. *Icarus*, 124:62, 1996. URL https://doi.org/10.1006/icar.1996.0190.

J. E. Pringle. Accretion disks in astrophysics. *Annual review of Astronomy and Astrophysics*, 19:137, 1981. URL https://articles.adsabs.harvard.edu/pdf/1981ARA%26A..19..137P.

D. Queloz et al. From CORALIE to HARPS. The way towards 1 m s-1 precision Doppler measurements. *The Messenger*, 105:1, 2001. URL https://ui.adsabs.harvard.edu/abs/2001Msngr.105....1Q/abstract.

R. P. Butler and others. Catalog of nearby exoplanets. *The Astrophysical Journal*, 646:505, 2006. URL https://doi.org/10.1086/504701.

R. Racine et al. Speckle Noise and the Detection of Faint Companions. *The Publications of the Astronomical Society of the Pacific*, 111:587, 1999. URL https://doi.org/10.1086/316367.

R. R. Rafikov. Dynamical evolution of planetesimals in protoplanetary disks. *The Astronomical Journal*, 126:2529, 2003. URL https://doi.org/10.1086/378609.

H. Rauer et al. The PLATO Mission. *Experimental Astronomy*, 59:26, 2025. URL https://doi.org/10.48550/arXiv.2406.05447.

S. N. Raymond et al. Building the terrestrial planets: Constrained accretion in the inner Solar System. *Icarus*, 203:644, 2009. URL https://doi.org/10.1016/j.icarus.2009.05.016.

I. N. Reid and S. A. Metchev. *Exoplanets*. Springer Praxis Books, 2008.

G. R. Ricker et al. Transiting Exoplanet Survey Satellite (TESS). *Journal of Astronomical Telescopes, Instruments, and Systems*, 1:014003, 2015. URL https://doi.org/10.1117/1.JATIS.1.1.014003.

A. Riols and H. Latter. Gravitoturbulence in magnetized protostellar discs. *Monthly Notices of the Royal Astronomical Society*, 460:2223, 2016. URL https://doi.org/10.1093/mnras/stw1112.

T. S. Ross. Limitations and applicability of the Maréchal approximation. *Applied Optics*, 48:1812, 2009. URL https://doi.org/10.1364/AO.48.001812.

G. Rousset et al. First diffraction-limited astronomical images with adaptive optics. *Astronomy and Astrophysics*, 230:L29, 1990. URL https://articles.adsabs.harvard.edu/pdf/1990A%26A...230L..29R.

V. S. Safronov. Evolution of the Protoplanetary Cloud and the Formation of the Earth and Planets. *Soviet Astronomy - AJ*, 16:183, 1972. URL https://adsabs.harvard.edu/full/1972SvA....16..183R.

A. Santerne. Populations of Extrasolar Giant Planets from Transit and Radial Velocity Surveys. *Handbook of Exoplanets*, 2018. URL https://doi.org/10.1007/978-3-319-55333-7_154.

A. Santerne et al. SOPHIE velocimetry of Kepler transit candidates. XVII. The physical properties of giant exoplanets within 400 days of period. *Astronomy and Astrophysics*, 587:A64, 2016. URL https://doi.org/10.1051/0004-6361/201527329.

N. C. Santos et al. The HARPS search for southern extrasolar planets. XXV. Results from the metal-poor sample. *Astronomy and Astrophysics*, 526:A112, 2011. URL https://doi.org/10.1051/0004-6361/201015494.

H. M. Schmid et al. SPHERE/ZIMPOL high resolution polarimetric imager. I. System overview, PSF parameters, coronagraphy, and polarimetry. *Astronomy and Astrophysics*, 619:A9, 2018. URL https://doi.org/10.1051/0004-6361/201833620.

G. Schneider et al. NICMOS Coronagraphic Observations of the GM Aurigae Circumstellar Disk. *The American Astronomical Society*, 125:1467, 2003. URL https://doi.org/10.1086/367596.

N. I. Shakura and R. A. Sunyaev. Black holes in binary systems. Observational appearance. *Astronomy and Astrophysics*, 24:337, 1973. URL https://adsabs.harvard.edu/full/1973A%26A....24..337S.

Y. Shvartzvald et al. The frequency of snowline-region planets from four years of OGLE-MOA-Wise second-generation microlensing. *Monthly Notices of the Royal Astronomical Society*, 457:4089, 2016. URL https://doi.org/10.1093/mnras/stw191.

A. Sivaramakrishnan and B. R. Oppenheimer. Astrometry and Photometry with Coronagraphs. *The Astrophysical Journal*, 647:620, 2006. URL https://doi.org/10.1086/505192.

A. Sivaramakrishnan et al. Ground-based Coronagraphy with High-order Adaptive Optics. *The Astrophysical Journal*, 552:397, 2001. URL https://doi.org/10.1086/320444.

M. F. Skrutskie et al. The Two Micron All Sky Survey (2MASS). *The Astronomical Journal*, 131:1163, 2006. URL https://doi.org/10.1086/498708.

M. Smoluchowski. Drei Vorträge über Diffusion, Brownsche Molekularbewegung und Koagulation von Kolloidteilchen. *Physikalische Zeitschrift*, 17:557, 1916. URL https://jbc.bj.uj.edu.pl/dlibra/publication/411756/edition/387534/content.

R. Soummer et al. Detection and characterization of exoplanets and disks using projections on Karhunen–Loève eigenimages. *The Astrophysical Journal Letters*, 755:L28, 2012. URL https://doi.org/10.1088/2041-8205/755/2/L28.

K. G. Stassun et al. The Revised TESS Input Catalog and Candidate Target List. *The Astronomical Journal*, 158:138, 2019. URL https://doi.org/10.3847/1538-3881/ab3467.

J. H. Steffen et al. Transit timing observations from Kepler – VII. Confirmation of 27 planets in 13 multiplanet systems via transit timing variations and orbital stability. *Monthly Notices of the Royal Astronomical Society*, 428:1077, 2013. URL https://doi.org/10.1093/mnras/sts090.

D. J. Stevenson. The Search for Brown Dwarfs. *Annual Review of Astronomy and Astrophysics*, 29:163, 1991. URL https://doi.org/10.1146/annurev.aa.29.090191.001115.

O. Struve. Proposal for a project of high-precision stellar radial velocity work. *The Observatory*, 72:199, 1952. URL https://articles.adsabs.harvard.edu/pdf/1952Obs....72..199S.

H. Tanaka, T. Takeuchi, and W. R. Ward. Three-Dimensional Interaction between a Planet and an Isothermal Gaseous Disk. I. Corotation and Lindblad Torques and Planet Migration. *The Astrophysical Journal*, 565:1257, 2002. URL https://doi.org/10.1086/324713.

A. Toomre. On the gravitational stability of a disk of stars. *Astrophysical Journal*, 139:1217, 1964. URL https://doi.org/10.1086%2F147861.

W. A. Traub and B. R. Oppenheimer. *Direct Imaging of Exoplanets. In: Exoplanets*. S. Seager, 2010.

J. T. Trauger and W. A. Traub. A laboratory demonstration of the capability to image an Earth-like extrasolar planet. *Nature*, 446:771, 2007. URL https://doi.org/10.1038/nature05729.

A. Udalski et al. A Venus-mass Planet Orbiting a Brown Dwarf: A Missing Link between Planets and Moons. *The Astrophysical Journal*, 812:47, 2015. URL https://doi.org/10.1088/0004-637X/812/1/47.

N. Unger et al. Exploring the brown dwarf desert with precision radial velocities and Gaia DR3 astrometric orbits. *Astronomy and Astrophysics*, 680:A16, 2023. URL https://doi.org/10.1051/0004-6361/202347578.

A. Vigan et al. Exoplanet characterization with long slit spectroscopy. *Astronomy and Astrophysics*, 489:1345, 2008. URL https://doi.org/10.1051/0004-6361%3A200810090.

A. Vigan et al. Photometric characterization of exoplanets using angular and spectral differential imaging. *Monthly Notices of the Royal Astronomical Society*, 407:71, 2010. URL https://doi.org/10.1111/j.1365-2966.2010.16916.x.

S. J. Weidenschilling and F. Marzari. Gravitational scattering as a possible origin for giant planets at small stellar distances. *Nature*, 384:619, 1996. URL https://doi.org/10.1038/384619a0.

L. M. Weiss et al. The Mass of KOI-94d and a Relation for Planet Radius, Mass, and Incident Flux. *The Astrophysical Journal*, 768:14, 2013. URL https://doi.org/10.1088/0004-637X/768/1/14.

R. Wielen et al. Indications on the binary nature of individual stars derived from a comparison of their HIPPARCOS proper motions with ground-based data. I. Basic principles. *Astronomy and Astrophysics*, 346:675, 1999. URL https://doi.org/10.48550/arXiv.astro-ph/9901228.

J. N. Winn. Transits and Occultations. *Exoplanets*, 2010. URL https://doi.org/10.48550/arXiv.1001.2010.

A. Wolszczan. Confirmation of Earth-Mass Planets Orbiting the Millisecond Pulsar PSR B1257+12. *Science*, 264:538, 1994. URL https://doi.org/10.1126/science.264.5158.538.

A. Wolszczan and D. A. Frail. A planetary system around the millisecond pulsar PSR1257 + 12. *Nature*, 265:145, 1992. URL https://doi.org/10.1038/355145a0.

J. T. Wright et al. The Frequency of Hot Jupiters Orbiting nearby Solar-type Stars. *The Astrophysical Journey*, 753:160, 2012. URL https://doi.org/10.1088/0004-637X/753/2/160.

J. K. Zink and B. M. S. Hansen. Accounting for multiplicity in calculating eta Earth. *Monthly Notices of the Royal Astronomical Society*, 487:246, 2019. URL https://doi.org/10.1093/mnras/stz1246.